SOLUTE-SOLVENT INTERACTIONS OF TRANSITION METAL CONTAINING COMPLEXES DETERMINED VIA GAS PHASE PHOTODISSOCIATION SPECTROSCOPY

By

DARRIN JOSEPH BELLERT

A DISSERTATION PRESENTED TO THE GRADUATE SCHOOL
OF THE UNIVERSITY OF FLORIDA IN PARTIAL FULFILLMENT
OF THE REQUIREMENTS FOR THE DEGREE
OF DOCTOR OF PHILOSOPHY

UNIVERSITY OF FLORIDA

1998

This dissertation is dedicated to three wonderful little time syncs
who have made the writing of this dissertation most difficult (yet worth it).

Danielle
Allison
and
Sam

ACKNOWLEDGMENTS

Above and beyond anyone else, I thank Phil. He is no longer just a mentor but a friend. He is also the only person I know who can glance at a 4000 cm^{-1} complicated spectrum composed of many vibronic progressions within overlapping electronic transitions and pick out the 10 cm^{-1} "bad splice". When it comes to science, "just ask Phil".

I also thank Dr. Thandi Buthelezi. She is an amazing person and a wonderful friend. This dissertation would not be possible without her. I could not ask for a better team mate than Thandi. Once, she allowed me to measure her response time after she was accidently shot with the pulsed dye laser. From the repetition rate of the laser and distance between laser burns on her skin, we calculated how fast she was moving away from the laser field. I wanted to repeat the experiment to validate the results....but she refused.

I also thank Dr. Tom Hayes. He is a true friend and my girls love him. He also has made this dissertation possible.

I thank my dad "big Al". He gave me a job and taught me how to work. Lessons which I carry with me always.

TABLE OF CONTENTS

ACKNOWLEDGMENTS....iii

ABSTRACT....vi

CHAPTERS

1 INTRODUCTION....1

2 THE EXPERIMENT....3

Main Chamber....3
The Mass Spectrometer....6
Line-Shapes and Broadening Mechanisms....8

3 THE VIBRONIC STRUCTURE OF TWO GROUP 5 METAL XENIDES: VXe^+ AND $NbXe^+$....14

Vibronic Analysis....15
Dissociation Energies....23
Discussion....27

4 THE Co^+-RARE GAS COMPLEXES....31

Electrostatics....32
Electronic Structure of the Cobalt Atomic Ion....36
$CoRG^+$....48
Overview....48
Transitions in the **a-X** system....61
The **A-X** and **C-X** transitions of $CoRG^+$....70
The **b-X** and **D-X** transitions....77
Trends in the $CoRG^+$ complexes....85
$CoRG^+$ summary....87

5 THE STRUCTURE OF Co^+OCO....89

Results....91
Discussion....102

6 THE STRUCTURE OF Co^+N_2 105

Results 107
Discussion 112
CoN_2^+ Conclusions 113

7 THE SOLVATION OF ZrO^+ 114

Results 114
ZrO^+Ar and ZrO^+OCO 116
ZrO^+N_2 125
ZrO^+CO 134
Discussion 139

8 CONCLUDING REMARKS 145

REFERENCES 147

BIOGRAPHICAL SKETCH 152

Abstract of Dissertation Presented to the Graduate School
of the University of Florida in Partial Fulfillment of the
Requirements for the Degree of Doctor of Philosophy

SOLUTE-SOLVENT INTERACTIONS OF TRANSITION METAL CONTAINING COMPLEXES DETERMINED VIA GAS PHASE PHOTODISSOCIATION SPECTROSCOPY

By

Darrin Joseph Bellert

August, 1998

Chairperson: Philip J. Brucat
Major Department: Chemistry

High resolution gas phase studies of solvated mono-positive transition metal atoms and molecules have been accomplished through photodissociation spectroscopy of a mass selected, supersonically cooled ion beam. The solute/solvent interaction has been characterized with spectroscopic detail. The solute in every case is either an open d-shell transition metal cation or the oxide of a transition metal. The closed-shell solvating ligands are typically simple monatomic, diatomic, or triatomic molecules. The characteristics of the bond which forms between the transition metal (solute) and ligand (solvent) are ubiquitous to the long-ranged intermolecular forces dominating in the condensed phase.

The most intrinsic properties determined through the association of the interacting fragments have been spectroscopically measured and these include bond dissociation energies, vibrational frequencies, bond lengths, bond force constants, etc. The evolution of these properties as a function of bonding partner has been qualitatively determined and certain trends established.

CHAPTER 1
INTRODUCTION

Why study the solvation of metal containing cations? Why study solvation? Why do basic research? To answer the above questions is simple, I can and I'm curious.! We should study solvation because (and I paraphrase Star Trek [1]) are we all not simply "ugly bags of water". Think of the researcher interested in determining the properties of a biologically important protein who, instead of performing a potentially difficult experiment, decides to calculate these properties. Due to the aqueous intercellular environment, a gas-phase calculation will clearly provide questionable results concerning the properties of the protein molecule. It is therefore up to the experimentalist to measure the effects of solvation and up to the programmer to incorporate these results into the computer code. Additionally, the control of reactant solvation imposed by water flow through semi-permeable cellular membranes may be used as a governing device to ensure the outcome (product formation) of biologically important intercellular chemical reactions. It can therefore be deemed that knowledge of molecule solvation is of utmost importance.

The spectroscopic study of this weak interaction, which gains chemical importance through ensemble action, has only recently been made possible through application of supersonic beam techniques [2]. The "non-bonded" electrostatic complex, or cluster, typifies the intermolecular properties associated with the condensed phase but is studied in

the gas phase where it is isolated and free to vibrate and rotate. High resolution studies of molecules in the bulk condensed phase are doomed to failure through "nearest neighbor" effects washing out the well defined quantized energy level structure of the isolated complex.

The bulk of this dissertation deals with the measurement and interpretation of the quantized properties of simple charged transition metal-ligand complexes. As we are graduating from the (albeit important) study of solvated atoms, a chapter has been devoted to the study of a solvated charged transition metal containing molecule (*i.e.* the solvation of ZrO^+).

CHAPTER 2
THE EXPERIMENT

The experiment can be broken down into three main parts. The synthesis, cooling and columnation of the molecular clusters occur in the main chamber. Mass separation and parent (or fragment) ion detection occurs in a specialized time of flight mass spectrometer. Photointerrogation of the mass selected parent ions is accomplished via one (or both) of the pulsed tunable dye lasers. Figure 2-1 provides a schematic of the instrument. At the end of this chapter a short discussion of line shapes and broadening mechanisms encountered in the photodissociation action spectra is presented.

Main Chamber

The main chamber is a 500 liter vacuum chamber (backed by one 10 inch and two 6 inch diffusion pumps) which is broken down into two sections. The primary region (operating pressure ~ 10^{-5} torr) is where synthesis and consequent cooling of the cations occur. Roughly in the center of the primary region a capture flange is situated which contains the source block and pulsed valve. A rotating transition metal target rod is located inside the source block (fig. 2-2). The pulsed valve (General Valve) is coupled via 1/4 inch stainless steel tubing to a high pressure gas manifold situated outside the vacuum chamber. The line contains a regulated supply of 20 - 150 psi of the ligand doped carrier gas. The concentration of the ligand is roughly 10 psi diluted to 1000 psi in helium.

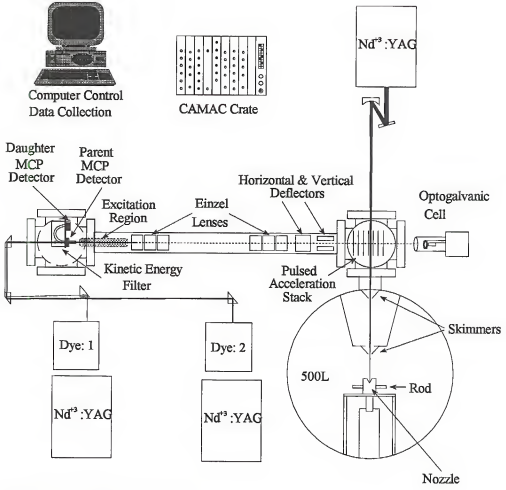

Figure 2-1. The Experiment.

The focused 2nd harmonic of Nd^{+3}:YAG laser oblates a rotating transition metal rod within a 500 L vacuum chamber. Just prior to oblation, a pulse valve is triggered to momentarily open emitting a burst of gas which entrains the thus formed clusters. The laser driven plasma supersonically expands and transgress two conical skimmers before entering into the acceleration region of a time of flight mass spectrometer. The pulsed stack accelerates the ions at 90° relative to the molecular beam down a 2.5 meter flight tube into a kinetic energy analyzer. Just prior to entrance, one of two pulsed dye lasers is triggered to fire and intercepts the ion beam in the excitation region. The kinetic energy analyzer is tuned to transmit fragment ions resulting from photon absorption. Signal is observed when heavy particles strike a dual microchannel plate electron multiplier located at the exit slit of the kinetic energy filter.

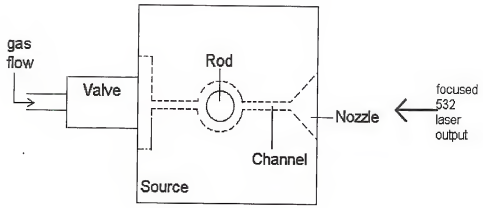

Figure 2-2. The Source Block.

A stainless steel metal block which supports the rotating rod, pulse valve, and expansion nozzle.

A current pulse to the valve solenoid pulls a poppett away from the sealing faceplate thus allowing a burst of gas to be released. The ligand doped helium gas is directed through the source block and engulfs the rotating transition metal rod. As the metal is bathed in the gas, the focused 2nd harmonic of a pulsed Nd^{+3}:YAG laser (7 ns, ~15 mJ/pulse) oblates the metal's surface causing the formation of a cascade of neutral and

charged transition metal atoms and clusters. The hot plasma transgresses a 1.5 cm channel and upon exiting suffer a supersonic, adiabatic expansion which essentially quenches the internal energy of the beam. As the density and temperature drop during the rapid expansion, cationic collisions with the polarizable ligand (and carrier gas) result in bond formation. It should be noted that this method of a pulsed laser driven, high pressure plasma followed by supersonic expansion is in fact a gentle method of molecular cation formation and the only way to routinely synthesize weakly bound (< 0.5 eV) inductive complexes.

The thus formed molecular beam drifts (velocity = the speed of sound through helium) through a conical skimmer and into the secondary region of the main chamber. The operating pressure here is ~10^{-6} torr and this region serves to further columnate the molecular beam as it drifts through a second conical skimmer and into the acceleration region of a time of flight mass spectrometer.

The Mass Spectrometer

Roughly 600 μs. after formation, the ion beam enters a liquid nitrogen trapped, differentially pumped, oil free vacuum chamber (operating pressure ~ 10^{-7} torr) which serves as the acceleration region of a time of flight mass spectrometer. The positive ions are accelerated to 1.45 keV at a right angle to the neutral beam axis and shot down a 2.5 meter stainless steel flight tube. The acceleration is accomplished in two stages (in accord with Wiley and McLaren [3]) as a series of parallel capacitor plates is pulsed from the

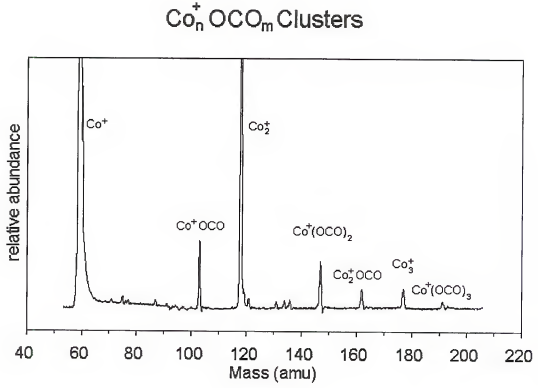

Figure 2-3. A typical mass spectrum.

ground to high voltage. Electrostatic optics guide the ion beam down the flight tube and into a 180° electrostatic sector situated inside the final differentially pumped, liquid nitrogen trapped vacuum chamber (operating pressure ~ 10^{-8} torr).

The sector serves as a kinetic energy filter and signal is observed when heavy particles strike a dual microchannel plate electron multiplier at the exit slit of the sector. Parent time of flight mass spectra are observed when the electrostatic sector is set to transmit ions of the full kinetic energy 1.45 keV. Figure 2-3 shows a typical time of flight mass spectrum observed in our lab. Daughter mass spectra are observed at the time of

arrival associated with the parent but at a kinetic energy equal to the ratio of the daughter to parent mass multiplied by the kinetic energy of the parent. Photodissociation spectra of mass selected parent ions are obtained with the sector tuned to transmit daughter ion products resulting from a dissociation event. The energy resolution of the kinetic energy filter is 1 part in 10 and the mass resolution of the time of flight is 1 part in 250.

Photodissociation action spectra are obtained from continuous scans of a tunable Nd^{+3}:YAG pumped dye Laser (Lumonics HD500 or Quantel) timed to intersect the parent ion of interest just prior to the entrance of the electrostatic sector which is tuned to transmit the daughter ion. The optical resolution of the experiment is limited by the laser linewidth and is a little better than 0.1 cm^{-1}. The photodissociation yield (photofragment abundance) is monitored as a function of dye-laser frequency. Neon optogalvanic transitions are recorded simultaneously with unknown photodissociation spectra to provide absolute frequency calibration of the spectrum. As the laser beam counterpropagates along the ion beam axis, a Doppler shift is necessary to bring the calibrated spectra into the laboratory frame. Critical timing parameters and voltages are controlled by a CAMAC crate/personal computer combination operating with real time software.

Line-Shapes and Broadening Mechanisms

As previously mentioned the laser linewidth ultimately limits the optical resolution of the spectra. Transitions which are limited by the laser linewidth have Lorentzian line-

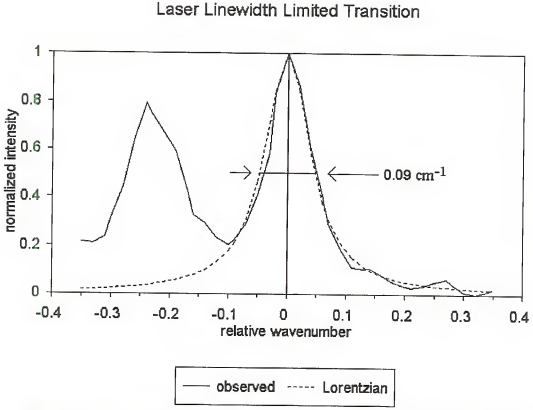

Figure 2-4. The R(J'= 5 ½) ← R(J"= 4 ½) transition in the [09.86] 9/2 ← X 9/2 (21,0) band of $^{58}Ni_2^+$.

This transition was only limited by the laser linewidth and fit to a Lorentzion line shape. The full width at half max is 0.09 cm^{-1}.

shapes with a FWHM ≤ .1 cm^{-1} (the linewdith of the dye laser). A normalized Lorentzian line-shape function is given in eqn. 2-1.

$$g(\nu-\nu_R) = \frac{\gamma}{(\frac{\gamma}{2})^2 + (2\pi)^2 (\nu-\nu_R)^2} \qquad (2\text{-}1)$$

where ν_R is the resonant frequency and γ is a constant which is related to the FWHM ($\Delta\nu_{1/2}$).

$$\Delta\nu_{1/2} = \frac{\gamma}{2\pi} \tag{2-2}$$

Several molecular systems have been studied which were limited by the laser linewidth. In particular the rotational structure of the $v' = 21 \leftarrow v'' = 0$ band of the [09.86] 9/2 ← X 9/2 system of Ni_2^+ [4]. The bluest transition in this band is the R(J'= 5 ½) ← R(J''= 4 ½) and is reproduced in figure 2-4. The peak was fit to the Lorentzian line-shape function of eqn. 2-1 and is provided as the dotted curve in fig. 2-4. The full width at half max of this peak is 0.09 cm^{-1} as indicated in the figure.

Another broadening mechanism which involves the Lorentzian line-shape is lifetime broadening and is due to the uncertainty principle.

$$\Delta E \Delta t \geq \hbar \tag{2-3}$$

Rearranging eqn. 2-3 gives

$$\frac{\Delta E}{h} = \Delta\nu = \frac{1}{2\pi\tau} \tag{2-4}$$

where the excited state lifetime (τ) places a limit on the linewidth arising from a transition between two states. The FWHM of these transitions provide estimates of the excited state lifetime via eqn. 2-2. Fig. 2-5 shows the origin of a band system observed in $ZrON_2^+$ [5]. The peak is fit both to a Lorentzian and to a Doppler line-shape (Gaussain) function. As

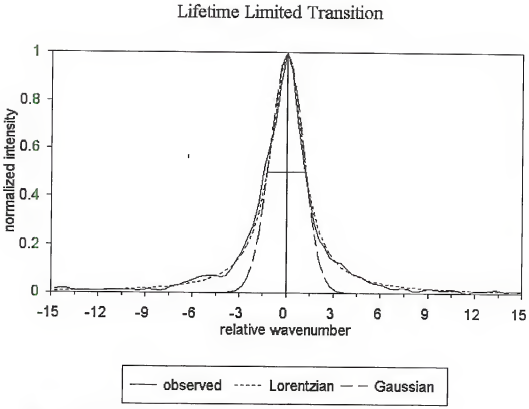

Figure 2-5. The origin of a band system observed in $ZrON_2^+$.

This band contour was fit to both Lorentzian and Doppler line shape functions. The agreement with the Lorentzian is obvious.

the experiment is sub-Doppler, the Lorentzian is expected to (and does) accurately portray the observed peak shape. The FWHM of this transition is 2.5 cm^{-1} and thus provides an estimate of the excited state lifetime at 2.15 ps.

The previously discussed line broadening mechanisms are hard limits: one is determined by the instrument and one is set by the molecule. The final broadening mechanism to be addressed is power broadening and this is limited only by technique. The

actual power broadened line-shape is complicated and only estimations of the linewidth will be presented. In intense laser fields the molecule undergoes oscillations at the Rabi frequency

$$\nu_{Rabi} = \frac{\mu E}{h} \approx \Delta t^{-1} \tag{2-5}$$

where μ is the transition dipole moment and E is the electric field. The inverse of eq. 2-5 can be used as a rough estimate of the excited state lifetime and substituted into the uncertainty principle (eq. 2-3).

$$\Delta\nu = \frac{\mu E}{2\pi h} \tag{2-6}$$

The electric field E can be determined from the power of the laser beam (fluence = 10 mJ / 7 ns) and the transition dipole moment, μ, can be estimated from a guess of the oscillator strength (f) associated with the transition

$$f = \frac{8\pi^2 m_e \nu}{3he^2}\mu^2 \tag{2-7}$$

where f = 1 for a fully allowed transition. Consider the origin of the $^1\Delta_2$ system of $CoOCO^+$ [6] occurring around 12 300 cm^{-1}. This is basically a spin, parity forbidden transition centered on the Co^+ and expected to be of very weak oscillator strength (say f = 0.0005). This makes the transition dipole moment 0.3 D and $\Delta\nu \approx 0.3$ cm^{-1} which is

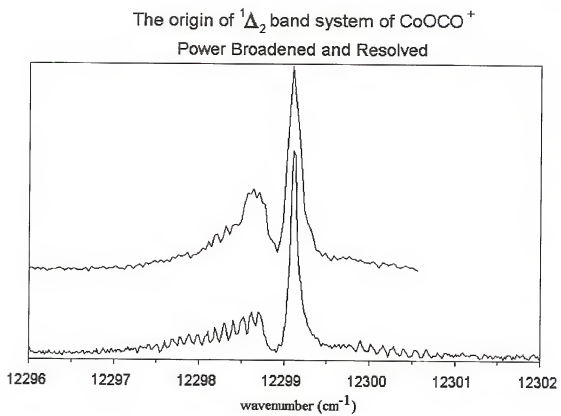

Figure 2-6. Two renditions of the origin of the $^1\Delta_2$ band system in $CoOCO^+$.

The spectrum of the upper trace was recorded under experimental conditions where the resolution was limited by the power of the pulsed laser. The lower trace was recorded under modified conditions which allowed the resolution to be limited only by the laser linewidth.

three times greater than the laser linewidth. To increase the resolution of the experiment a 10x dispersive element was set in the optical path of the laser beam roughly 30 cm in front of the laser/ion interaction region. This had the effect of decreasing the field intensity by a factor of 10^2 and decreased the power broadened linewidth by 10. Figure 2-6 shows two renditions of the origin of the $^1\Delta_2$ [6] system in $CoOCO^+$. The lower trace shows the resolved (laser linewidth limited) spectrum whereas the upper trace shows the power broadened spectrum.

CHAPTER 3
THE VIBRONIC STRUCTURE OF TWO GROUP 5 METAL XENIDES: VXe^+ AND $NbXe^+$

Spectroscopic studies of (metal ion)-(rare gas) electrostatic complexes can be found in the recent literature. $MgAr^+$ [7], $CaAr^+$ [8], $BaAr^+$ [9], and $SrAr^+$ [10] have been probed by elegant optical studies to elucidate the association of the argon atom to an atomic ion with s and p orbital occupation. In fact, the spectra of these molecules all share an intense Alkali-like "D line", coupling a weakly bound ground state to a more strongly bound excited state. Ion complexes with open d-shell metal centers are significantly more complicated and perhaps for this reason, more interesting. Our contribution to this science has been the optical spectroscopy of the transition metal ion-ligand complexes via resonant photodissociation [11-13]. Our early efforts concentrated on the lighter first row (transition metal)-(rare gas) ionic complexes and, in spite of weak s←d and spin-forbidden transitions, optical assignments have been made of several such species. Our recent work has addressed the heavier (and thus more relativistic) metal ions [14]. These studies of the group 5 metal xenides fall into context with similar studies of V^+ and Nb^+ (rare gas) ions [15-19], and most recently $TaAr^+$ [unpublished results].

The electronic transition probed in this study is derived from a parity forbidden, spin allowed transition centered on the group 5 metal cation: $3d^34s\ ^5P \leftarrow 3d^4\ ^5D$ and has

been dubbed the **B-X** electronic system of these molecules. Recent rotationally-resolved photodissociation spectra of the **B-X** transition in VAr^+ from our laboratory [19] shows the ground state of the ion to be $^5\Sigma^+$ ($\Omega'' = 0$) with a zero-point bond length of 2.64 Å. This ground state bond length is predicted accurately (within 1%) by high-level theory [20] for this ion. The excited **B** state of VAr^+, and presumably all the analogous Nb^+·RG and V^+·RG ions, is $\Omega'=1$ ($^5\Pi_1$). In VAr^+, the bond length of the **B** $^5\Pi_1$ state ($v'=0$) is 2.91Å, an increase of 0.27Å over the ground state. As the excited state electronic configuration has a larger repulsive interaction with the RG than does the ground state, this leads to the long progression in the upper state vibrational quantum number evident in the **B-X** electronic transition in all V^+/Nb^+ - ligand systems.

Vibronic Analysis

Figure 3-1 shows the $^{51}V^{129}Xe^+$ photodissociation spectrum in the region from 15 500 to 18 000 cm^{-1}. The horizontal axis is the dissociation laser frequency in wavenumbers and the vertical axis displays relative photofragmentation into $V^+ + Xe$, which is related to the absolute absorption of the ion. A single progression containing 27 different upper vibronic levels has been identified and labeled by the upper state vibrational quantum number in this figure. The spectrum also contains transitions to electronic states different than that of the most prominent progression, and these bands have not yet suffered analysis. The presence of these 'extra' states is related to numerous perturbations and intensity anomalies in the most prominent band system. Notably, vibronic transitions

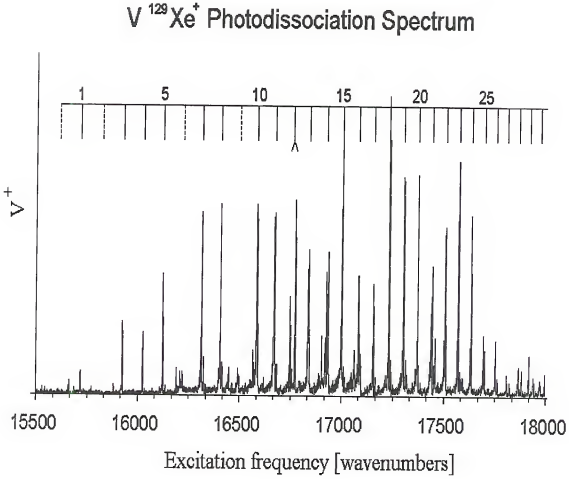

Figure 3-1. The resonant photodissociation of $V^{129}Xe^{+}$.

The horizontal axis is dye laser frequency and the vertical axis is relative V^{+} photocurrent resulting from the photodissociation of mass selected $V^{129}Xe^{+}$. A single vibrational progression has been labeled by upper state quantum number. The dotted ticks label the expected position of missing bands. All transitions originate from the vibrationless level of the ground state, i.e. are 'cold bands'.

connecting the ground state to the **B** state with v′ = 0, 2, 6, and 9 (dashed tick marks, fig.3-1) are either missing or grossly perturbed. The energy of two other transitions (v′ = 12 and 25) were determined by weighted average of a split or 'doubled' transition.

Table 3-1. Cold band positions in the VXe^+ $B\,^5\Pi_1 \leftarrow X\,^5\Sigma^+$ System

v'	Observed	Fit to Eq. 1	Residual
0		15612.575	
1	15718.9	15718.581	0.3
2		15822.695	
3	15925.3	15924.917	0.4
4	16025.6	16025.246	0.4
5	16123.9	16123.683	0.2
6		16220.229	
7	16314.8	16314.881	-0.1
8	16407.4	16407.642	-0.3
9		16498.511	
10	16586.0	16587.487	-1.5
11	16671.9	16674.571	-2.7
12	[16761.4][a]	16759.763	1.6
13	16841.8	16843.063	-1.3
14	16925.5	16924.47	1.1
15	17002.7	17003.985	-1.3
16	17083.0	17081.608	1.4
17	17157.3	17157.339	-0.1
18	17233.1	17231.178	2.0
19	17304.5	17303.124	1.4
20	17373.9	17373.179	0.8
21	17441.6	17441.341	0.3
22	17506.8	17507.61	-0.8
23	17571.1	17571.988	-0.8
24	17634.2	17634.473	-0.3
25	[17695.9][b]	17695.067	0.8
26	17753.8	17753.768	0.1
27	17808.3	17810.576	-2.2
28	17865.7	17865.493	0.2
29	17917.4	17918.517	-1.2
30	17971.3	17969.649	1.7

[a]weighted average of two bands at 16748.7 and 16774.0 cm^{-1}
[b]weighted average of two bands at 17692.5 and 17699.2 cm^{-1}

Table 3-1 lists the line positions and residuals to a least squares fit of the vibronic transitions to the standard formula:

$$\vartheta\,(v',0) = T_{00} - (\omega_e'/2 - \omega_e x_e'/4) + \omega_e'\,(v' + \tfrac{1}{2}) - \omega_e x_e'\,(v' + \tfrac{1}{2})^2 \qquad (3\text{-}1)$$

Perturbed transitions were not included in the fit. The constants derived from this formula are presented in Table 3-2 along with those determined for the other V^+/Nb^+-(rare-gas) complexes. Figure 3-2 is a plot of transition frequency -vs- upper state vibrational quantum number, $(v' + \tfrac{1}{2})$, for all the observed 'cold band' transitions in the $\mathbf{B}\,^5\Pi_1 \leftarrow \mathbf{X}\,^5\Sigma^+$ system. The symbols represent observed data and the solid curve calculated based on the formula above and the constants of Table 3-2. If the local perturbations are ignored, the observed vibrational structure of VXe^+ is well described by eqn. (3-1).

Table 3-2. Properties of Nb^+-Rg and V^+-Rg Molecules [cm^{-1}, except where noted]

		$NbAr^+$	$NbKr^+$	**$NbXe^+$**	VAr^+	VKr^+	**VXe^+**
B state ($^5\Pi_1$)	T_{00}	12 740 [b]	13 377 [a]	**13 601**	15 216 [b]	15 368	**15 613**
	ω_e'	82.3 [b]	90.1 [a]	**85.2**	90.4 [b]	94.0	**107.9**
	$\omega_e x_e'$	1.46	1.12 [a]	**0.63**	1.56	1.13	**0.95**
	k'(N/m)	11.2 [b]	21.1 [a]	**23.1**	10.8 [b]	16.5	**25.1**
	D_0'	1202 [b]	2066 [a]	**3051**	1353 [b]	2051	**3222**
X state ($^5\Sigma^+$)	D_0''	3106	4607 [a]	**5815**	2975	3824	**5240**

[a] Preliminary results.

[b] Results [17,15] dependent on a vibrational numbering that cannot be confirmed by isotope shifts at the present time.

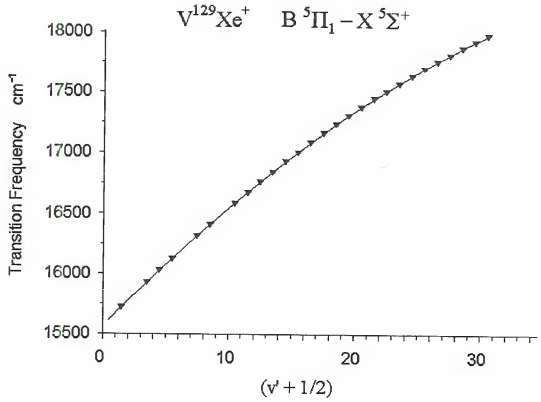

Figure 3-2. The vibrational structure of the $\mathbf{B}^5\Pi_1$-$\mathbf{X}^5\Sigma^+$ system in $V^{129}Xe^+$.

The solid curve has been calculated based on eqn. 3-1 and the constants of table 3-2. The symbols are observed cold band transition frequencies.

Portions of the photodissociation action spectrum for both $Nb^{129}Xe^+$ (lower trace) and a minor naturally occurring isotopic variant $Nb^{136}Xe^+$ (top trace) is shown in figure 3-3. Labeled by their upper state vibrational quantum numbering, the transitions seen in fig. 3-3 are representative of the 49 observed vibronic bands in the $\mathbf{B}\,^5\Pi_1 \leftarrow \mathbf{X}\,^5\Sigma^+$ system of this ion, and spans from 13 800 to 16 300 cm^{-1} and covers nearly 80% of the vibrational

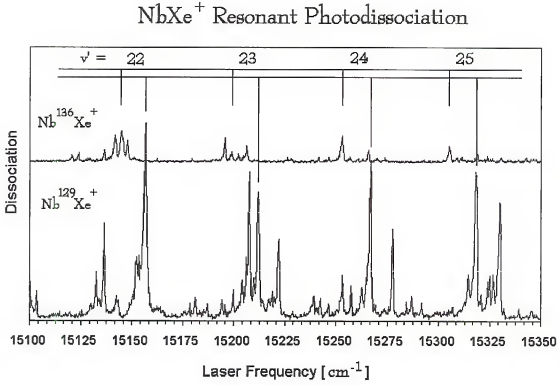

Figure 3-3. A portion of the resonant photodissociation spectrum of $NbXe^+$.

The transitions in the $Nb^{136}Xe^+$ molecule are shown in the top panel and those in the most abundant isotope, $Nb^{129}Xe^+$, are shown in the bottom panel. These spectra are obtained simultaneously to improve the accuracy with which the isotope shift is recorded. A portion of the vibrational progression has been labeled by upper state vibrational quantum number. All transitions originate from the vibrationless level of the ground state.

levels of the upper state. Also evident in fig. 3-3 are vibronic bands involving other upper states which are not under discussion here. The obvious red-shift of the heavier isotopomer with respect to the major species is purely an effect of the known mass change and provides unambiguous absolute vibrational quantum numbering of the transitions. The ability to select and monitor the photodissociation of the different $NbXe^+$ isotopes has

made the analysis of this and other congested spectra possible.

Table 3-3. Assigned Transitions in the $B\,^5\Pi_1 - X\,^5\Sigma^+$ system of $Nb^{129}Xe^+$

v'	Observed	Fit to Eq.1	Residual	v'	Observed	Fit to Eq.1	Residual
0		13600.59		27	15420.24	15422.52	-2.28
1		13684.58		28	15471.41	15472.22	-0.80
2		13767.30		29	15517.90	15520.65	-2.75
3	13842.46	13848.75	-6.29	30	15567.92	15567.80	0.12
4	13933.12	13928.93	4.19	31	15610.75	15613.69	-2.94
5	14004.65	14007.84	-3.19	32	15658.11	15658.31	-0.20
6	14088.23	14085.47	2.75	33	15700.82	15701.66	-0.84
7	14164.32	14161.84	2.47	34	15743.59	15743.74	-0.14
8	14236.35	14236.94	-0.60	35	15783.89	15784.55	-0.66
9	14310.53	14310.77	-0.25	36	15823.73	15824.09	-0.35
10	14379.61	14383.33	-3.72	37	15861.18	15862.35	-1.18
11	14452.04	14454.62	-2.58	38	15899.97	15899.35	0.62
12	14524.75	14524.64	0.11	39	15935.98	15935.08	0.90
13	14595.52	14593.39	2.13	40	15968.39	15969.54	-1.15
14	14657.55	14660.86	-3.32	41	16002.01	16002.73	-0.72
15	14728.08	14727.07	1.01	42	16035.33	16034.65	0.68
16	14792.09	14792.01	0.08	43	16065.49	16065.30	0.20
17	14856.88	14855.68	1.20	44	16096.00	16094.68	1.32
18	14920.25	14918.08	2.17	45	16123.65	16122.78	0.87
19	14982.39	14979.21	3.19	46	16150.17	16149.62	0.55
20	15040.39	15039.07	1.32	47	16178.71	16175.19	3.52
21	15099.03	15097.66	1.37	48	16204.24	16199.49	4.75
22	15156.80	15154.97	1.82	49	16228.30	16222.52	5.78
23	15212.07	15211.02	1.05	50	16252.25	16244.28	7.97
24	15266.99	15265.80	1.19	51	16274.61	16264.77	9.84
25	15318.40	15319.31	-0.91	52	16295.30	16283.98	11.32
26	15372.99	15371.55	1.44				

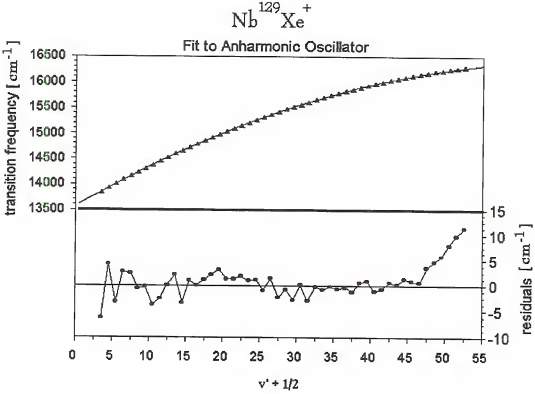

Figure 3-4. The vibrational structure of the **B-X** system in $Nb^{129}Xe^{+}$.

The top panel shows the the transition frequencies calculated based on eqn. (3-1) and the constants of Table 3-2 (solid curve). The experimental values (symbols) on the vertical axis are plotted versus upper state vibrational quantum number. The bottom panel and right vertical axis show the residuals to the fit (observed minus calculated) of band origins to eqn. 3-1.

The vibronic structure of $NbXe^{+}$ has been analyzed in identical fashion to VXe^{+}. The observed transitions (Table 3-3) have been fit to eqn. 3-1 and the vibrational constants extracted (Table 3-2). The top trace of figure 3-4 is a plot of transition frequency -vs- upper state vibrational quantum number, $(v' + \frac{1}{2})$, for all the observed transitions in the $\mathbf{B}\ ^5\Pi_1 \leftarrow \mathbf{X}\ ^5\Sigma^+$ system of $Nb^{129}Xe^{+}$. The deviation of the observed

vibrational structure of $NbXe^+$ from that predicted by eqn. 3-1 is shown in the lower panel of figure 3-4. Here the residuals are the observed minus the calculated band positions plotted versus upper vibrational quantum number. The anharmonic oscillator fails to describe the vibrational structure of the upper state near the diabatic dissociation limit.

Dissociation Energies

From the lower panel of fig. 3-4 it is clear that the Morse form of the potential energy (eqn. 3-1) provides an accurate description for only low lying vibrational levels of the molecule and fails for levels near dissociation. A more accurate dissociation limit may be obtained if the long-range forces are explicitly taken into account in the description of the vibrational structure at high quantum number. LeRoy and Bernstein (LB) [21] have provided such a treatment. Following LB, the vibrational energy level structure of the highest bound vibrational states have the property

$$\Delta G(v) = \tfrac{1}{2}\,[E(v+1) - E(v-1)] = -K\,[E(v) - D]^{(n+2)/2n} \qquad (3\text{-}2)$$

where $E(v)$ is the energy of the vibrational level in a given electronic state and D is the dissociation energy of that electronic state, K is a combination of fundamental constants and n is the order of 1/r in the long-range attractive part of the diatomic potential. For metal ions bound to the xenon atom, n=4 corresponds to the charge -(induced dipole) force at dissociation. Both $E(v)$ and D are taken with respect to the zero point level of the

ground state. The constant K has been shown to be [21]

$$K=\frac{hC_n^{-1/n}n\ \Gamma((n+1)/n)}{(2\pi\mu)^{1/2}\ \Gamma((n+2)/2n)} \qquad 3\text{-}3$$

where μ is the reduced mass of the diatomic, C_n is the coefficient of the $1/r^n$ term in the

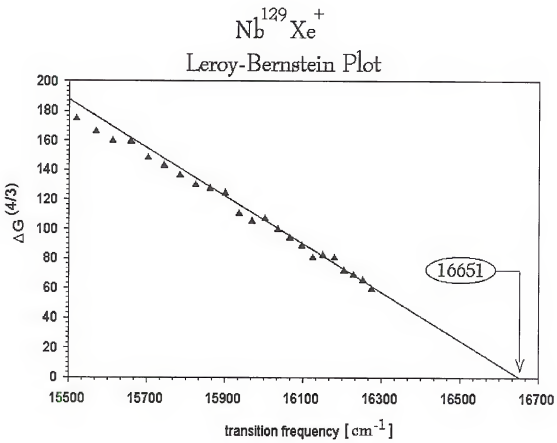

Figure 3-5. The Leroy-Bernstein extrapolation of the **B** state vibrational energy differences to the diabatic dissociation limit for $NbXe^+$.

The symbols represent observed values and the solid line is calculated from eqn. 3-2. This LB analysis places the diabatic dissociation limit at 16 651 cm^{-1}.

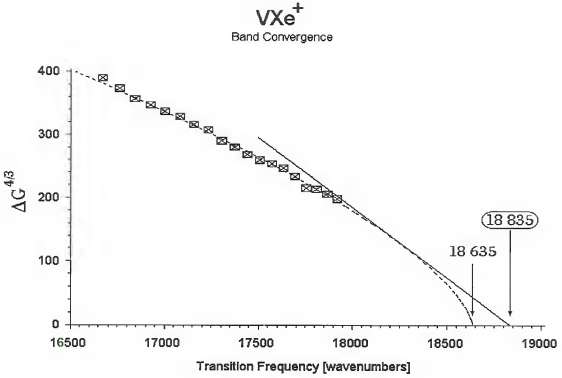

Figure 3-6. The extrapolation of the vibrational energy differences to the diabatic dissociation limit of the **B** state of VXe^+.

The symbols represent experimental data, the dotted curve represents the results of a hypothetical Morse potential function with the constants of Table 3-2, and the solid line represents the LB predicted line from eqn. 3-2 The accepted band convergence limit is not that of the Morse potential, but from the LB extrapolation, giving 18835 cm^{-1}.

potential function of the molecule and Γ is the standard Gamma function [22]. In our case, n = 4 and $C_4 = ½ (q^2\alpha)$ which may be evaluated by taking a full electron charge on the metal for q and the dipole polarizability, α, of Xenon at its bulk value, 4.11 $Å^3$ [23]. Application of eqn. 3-2 to metal-rare gas ions suggests a plot of $\Delta G^{4/3}$ -vs- $[E(v) - D]$ should be linear with a slope of $K^{4/3}$ for transitions approaching a band convergence.

Moreover, the theoretical slope of this line, obtained by inserting the relevant constants in eqn. 3-3 is $K^{4/3} = 0.2211\ (cm^{-1})^{1/3}$. This treatment has been successfully applied to both $VAr(Kr)^+$ [15] and $NbAr^+$ [17] to accurately extrapolate vibrational energy levels to the dissociation limit and fig. 3-5 shows this treatment applied to the **B** state limit of $NbXe^+$.

Unfortunately, application of the Leroy-Bernstein treatment to VXe^+ is impossible due to unfavorable Franck-Condon overlap with the highest bound vibrational levels in the $\mathbf{B}\ ^5\Pi_1$ state. The dissociation energy could rather be determined via the Birge-Sponer [24] treatment but it has already been seen that the Morse oscillator does not provide an accurate description of the molecule's vibrational structure nearing a dissociation limit and it has been observed that the Birge-Sponer prediction underestimates the true dissociation energy by roughly 7% [16]. The Leroy-Bernstein protocol is therefore applied to extrapolated (calculated) vibrational levels of VXe^+. Figure 3-6 shows a LeRoy-Bernstein plot for the highest observed transitions in the VXe^+ $\mathbf{B}\ ^5\Pi_1 \leftarrow \mathbf{X}\ ^5\Sigma^+$ system, which are shown with symbols. The dotted line in this figure shows the behavior of a hypothetical Morse type potential function with the vibrational constants derived for the VXe^+ $\mathbf{B}\ ^5\Pi_1$ state (Table 3-2). The Morse function deviates from the expected limiting behavior of this molecule and predicts a band convergence at 18 635 cm^{-1}. The correct LB limiting behavior is shown by the solid line in figure 3-6, which is drawn with the theoretical slope at a tangent to the Morse extrapolated dotted curve. We expect that this line accurately predicts the band convergence of the **B** state of this molecule at 18 835 ± 50 cm^{-1}.

The band convergence of both **B-X** systems have determined through LB analysis. The identification of the atomic states of the fragments that correspond to this limit must

be made from analogy with isovalent molecules. Two different band convergences have been identified in $NbAr^+$ [17] which allows the identification of those limits from the comparison of the difference in energy of those limits with the known electronic states of the Nb^+ ion [25]. The **B** state in $NbAr^+$ diabatically dissociates into $a\ ^5P_2\ Nb^+ + Ar\ (^1S_0)$ fragments and the **A** state into $a\ ^3G_5\ Nb^+ + Ar\ (^1S_0)$ fragments. VAr^+ too has two identifiable electronic systems [15] and a photodissociation spectrum similar in appearance to $NbAr^+$, with completely analogous dissociation limits. Based on the comparison with its sister molecules $NbAr^+$ and VAr^+, the electronic system discussed here is labeled the $\mathbf{B}\ ^5\Pi_1 \leftarrow \mathbf{X}\ ^5\Sigma^+$ and assigned a diabatic dissociation limit of $Xe\ ^1S_0 + a\ ^5P_2\ Nb^+\ (V^+)$ atoms. $NbXe^+$ dissociates into these fragments at 16 651 cm^{-1} above its zero point level and this limit is 10 835.85 cm^{-1} [25] above the ground state atoms, which leads to the determination of the binding energy, D_0, of the ground state of the ion of 5815 ± 10 cm^{-1}. VXe^+ dissociates into these fragments at 18 835 cm^{-1} above its zero point level and this limit is 13 594.73 cm^{-1} [25] above the ground state atoms, which leads to the binding energy, D_0, of the ground state of the ion at 5240 ± 50 cm^{-1}. The diabatic dissociation limit of the **B** state is simply the difference between D and T_{00}.

Discussion

The adiabatic dissociation energies, D_0", of V^+· Ar, V^+· Kr, V^+· Xe, as determined by photodissociation in this laboratory, are shown in Table 3-4. The values compare favorably with existing experimental and theoretical values. Aristov and Armentrout [26]

have determined the bond dissociation energy of these species through collisional dissociation (CID), and qualitative agreement exists in the ordering of the binding energies determined. Photodissociation, in this case, has proved to provide an overall accuracy superior to that of collisional work. High level *ab initio* theory has not yet been applied to VXe^+, but Bauschlicher [20] has predicted some of the properties of the low lying states of VHe^+, VNe^+ and VAr^+. The calculated dissociation energy (D_e") for VAr^+ is roughly 15% lower than what is observed experimentally (D_o"). This is consistent with a systematic discrepancy already observed between calculated and experimental bond

Table 3-4. The Ground State Binding Energies, D_0, of $V^+ \cdot Rg$ molecules (cm^{-1})

	VAr^+	VKr^+	VXe^+
D_0" (this work, Ref [15])	2975±15	3824±15	5240±50
Aristov and Armentrout (Ref [26]) [Experiment]	1600±1600 (0.2±0.2 eV)	3200±1600 (0.4±0.2eV)	6800±1400 (0.84±0.17eV)
Partridge and Bauschlicher (Ref [20]) [Theory]	2600 (0.322 eV)		

The authors original units are quoted in parenthesis

energies in $CrAr^+$, $CoAr^+$, and $NiAr^+$. In all cases, the calculated binding in these $M \cdot Ar^+$ molecules [20,27] is approximately 15% lower than the experimental values [11-13].

The 'bonding' in transition metal - rare gas ($M^+ \cdot Rg$) ions is largely electrostatic, with the electronic configuration of the metal ion playing an important role in the

determination of molecular properties. In the (group 5 metal)-Xe^+ and its analogs, the low-lying electronic states of the ion arise from two different electronic configurations of the metal ion, d^4 for the ground state and d^3s for several excited states, including the well studied $\mathbf{B}\ ^5\Pi_1$ state. The d^3s configuration of the metal has a larger repulsive radius than the d^4 configuration, which leads to a greater bond length and weaker binding energy of molecular states arising from this metal configuration, and long vibrational progressions in electronic transitions connecting these two configurations are observed. Comparison of the $\mathbf{B}\ ^5\Pi_1 \leftarrow \mathbf{X}\ ^5\Sigma^+$ band origin for complexes of successively heavier rare gases (i.e. $NbAr^+$, $NbKr^+$, $NbXe^+$ or VAr^+, VKr^+, VXe^+) shows a progressive blue shift, also indicative of a greater binding energy in the d^4 ground state than the d^3s excited state.

Figure 3-7 shows the trends in binding energies of the various transition-metal-ion rare-gas complexes, M^+·RG, for M=Co^+ or V^+/Nb^+ and RG= Ar, Kr, and Xe. Plotted in Fig. 3-7 are the binding energies (D_0) of various states of the M^+·RG complexes versus the rare-gas electric-dipole polarizability, α. The dotted lines and open squares indicate a nearly linear dependence of D_0 on α for 5 electronic states of 3 Co^+·RG ions. The data presented here, shown in solid lines and filled squares, shows that this relationship holds for the the ground and excited state observed in (group 5 $metal^+$)·RG ions as well. What is striking is that the polarizability dependence of the vanadium and niobium ion complexes' binding energies are nearly identical but more 'mild' than that of the cobalt ions. For the same metal ion fig. 3-7 shows the binding energies of different ion states fall on parallel lines, implying the same slope but different intercepts. The slope of the lines for V^+/Nb^+ ions is significantly smaller than that for Co^+ ions, however .

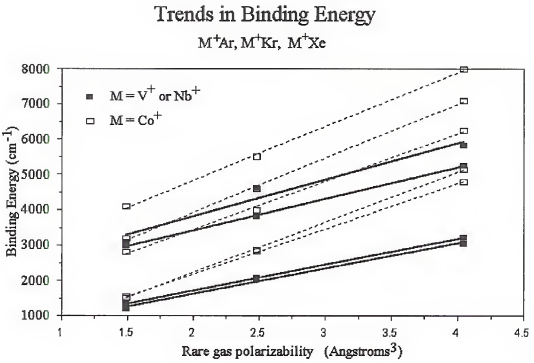

Figure 3-7. Trends in the binding of metal ion-rare gas complexes.

The dotted line and open squares show the binding energies (D_0) of various $CoRg^+$ ion states versus rare-gas electric-dipole polarizabilty. The solid line and filled squares show the same data for V/Nb Rg^+ ions. Note the nearly linear dependence of the binding energy on polarizability, but with different slopes for different groups of metal ions.

CHAPTER 4
THE Co^+-RARE GAS COMPLEXES

High-resolution spectroscopy has characterized the chemical interactions between covalently bonded atoms since the beginning of this century. The study of electronic, rotational, and vibrational transitions in simple isolated molecules has provided quantum mechanical detail of the structure of the chemical bond. But covalent bonds aren't the only interactions at work during a chemical reaction because, by necessity, the reactants are not isolated. The forces between non-bonded species are significant in all phases and become dominant in the condensed phase. Yet, high-resolution spectroscopy works best in the gas phase where the species of interest are isolated and its energy levels are well defined. This is the motivation for making model compounds that exhibit the non-bonded interactions ubiquitous in condensed phases and are yet tractable enough to be studied experimentally and theoretically to a worthy precision: 'clusters'. The spectra of weakly-bound van der Waals complexes or clusters, which exhibit the dispersion forces found in all liquids, has been made possible by the application of supersonic beam techniques and allows these species to be studied in just the same way that stable, chemically-bound species have suffered analysis.

When the non-bonded fragments of the liquid or cluster possess a net charge, the magnitude of the interaction is greatly increased relative to neutrals due to strong, long-

range electrostatic and inductive forces that are a consequence of the non-vanishing electric monopole moment(s) and this behavior is of great significance to the behavior of every electrolytic solution.

A wealth of information has been acquired for the Co^+-rare gas [11,28,29] complexes and is presented here. At least five excited states have been identified and characterized in each of the ionic molecules. The bonding characteristics in each molecule are state specific and differences have been attributed to such subtle interactions as d-orbital occupation and spatial orientation. The evolution of these bonding properties as a function of bonding partner is determined and various qualitative trends established.

The first section of this chapter provides a discussion of the electrostatic (and inductive) forces so common in the ionic clusters described in this dissertation. The second section gives a discussion of the electronic structure of the cobalt atomic ion, as all optical transitions described here originate from the Co^+ chromophore. The final section provides the spectra and analysis of the Co^+(rare gas) complexes.

Electrostatics

The focus of much of this discussion revolves around the concept of a formal charge separation between the parts of our ionic cluster and the subsequent electrostatic interaction between these parts. The forces are well known between simple static multipoles (electrostatics). The forces between permanent multipoles and induced multipoles (inductive forces) are slightly more difficult to calculate, but the dipole

polarizability of many atoms and molecules is known [23,30,31] (table 4-1). In fact, the dipole polarizability of Ar in the field of a single positive charge has been determined as 1.48 $Å^3$ by our group [32].

Table 4-1. IP's, multipole moments, and dipole polarizabilities

Species	IP[a] [eV]	quadrupole moment (Q) [$x10^{-40}$ Cm^2]	dipole moment (μ)[b] [$x10^{-30}$ Cm]	dipole polarizability (α)[b] [$Å^3$]
Co	7.86			
Co^+	17.06			
Ar	15.759			(1.48[c]) 1.641
Kr	13.999			2.484
Xe	12.130			4.044
CO_2	13.769	-14.3[b]		$4.31_{\parallel}$ $2.21_{\perp}$
N_2	15.576	-4.7[b]		$2.21_{\parallel}$ $1.51_{\perp}$
H_2O	12.6	-3.7[d]	6.284 (1.884 D)	
NH_3	10.2	-3.3[d]	4.920 (1.475 D)	$2.45_{\parallel}$ $2.16_{\perp}$

a. [33]
b. [30]
c. [32]
d [34]

Ideal values have been provided below which characterize the important electrostatic and inductive energies observed in our ionic cluster molecules. It is important to realize that some of the formula presented below are approximations based on Coulomb's law and that these approximate formula strongly deviate at short interaction

distances (say 1Å). The provided numeric examples below therefore employ interaction distances (3Å) which minimize deviations and are actually more applicable to the bond lengths observed in inductively bound cluster molecules.

Charge-Dipole

$$U(r) = -\frac{q\mu}{r^2} \tag{4-1}$$

Two electron charges with opposing signs separated by 1Å provides a dipole moment of 4.8 D and the energy of a single electron charge 3Å away from this dipole of 4.8 D is -12 896.25 cm^{-1}. The negative sign assumes the interaction is attractive and is dependent upon the orientation of the dipole. The magnitude of a repulsive interaction is the same as above but with the opposite sign.

Charge-Induced Dipole

$$U(r) = -\frac{q^2\alpha}{2r^4} \tag{4-2}$$

The energy of a single electron charge 3 Å away from a molecule with a polarizability of 1 $Å^3$ is -716.937 cm^{-1}. The negative sign indicates the interaction is attractive.

Charge-Quadrupole

$$U(r) = \frac{qQ}{2r^3}(3\cos^2\theta - 1) \qquad (4\text{-}3)$$

The unit of quadrupole moment is defined by an array of 4 point charges (2 positive and 2 negative) located on the vertices of a square with side length = 1Å. Common charged vertices are connected through the diagonal of the square and the quadrupole moment associated with this arrangement is -2.40326×10^{-39} Cm^2 [30] and is directional along the line connecting the negative charges. The same magitude but different sign of the quadrupole moment occurs along the line connecting the positive charges. The energy of a single positive electron charge located 3Å away from this quadrupole moment and lying along the line connecting the negative charged vertices is -6452.41 cm^{-1}.

The above formalisms are applicable to the ion cluster complexes presented in this dissertation. From table 4-1 the disparity in IP between the metal and ligand assures that the metal acts as a formal monopole of +e charge. The main contributor to the observed binding energies in these complexes are due to the electrostatic and inductive forces and a sampling of these contributions is presented in Table 4-2.

Negative entries of Table 4-2 indicate the association is attractive while the positive entry indicates a repulsive interaction. Experimentally observed bond lengths have been used in Table 4-2 when possible. The bond lengths for CoN_2^+ (T and linear) are the average of the best various theoretical calculations performed. The calculations typically provide only the Co^+-(nearest atom) bond lengths for the polyatomic complexes.

The bond lengths of Table 4-2 provide the Co^+-(center of mass) distance of the various ligands and were determined from the unperturbed, gas phase geometries of the bonding partner [35] and calculated Co^+-(nearest atom) bond lengths.

Table 4-2. The electrostatic forces present in Co^+ complexes

Complex	Center-Center Distance [Å]	Charge-Dipole [cm^{-1}]	Charge-Quadrupole [cm^{-1}]	Charge-Induced Dipole [cm^{-1}]
$CoAr^+$	2.385[a]			-2674
$CoKr^+$	2.447[a]			-4023
$CoXe^+$	2.9[a]			-3320
$CoOCO^+$	3.174[a]		-3242	-2466
CoN_2^+ (lin)	2.52[b]		-2129	-3182
CoN_2^+ (T)	2.17[b]		1667	-3955
$CoOH_2^+$	2.10[c]	-10285		
$CoNH_3^+$	2.23[c]	-7199		-5797

a. This study
b. [36-38]
c. [39-40]

Electronic Structure of the Cobalt Atomic Ion

The similarity in the spectrum of the Co^+ complexes in this study results from the fact that the atomic ion itself is the chromophore for all the observed optical transitions. Since the complexes discussed in this chapter are largely electrostatically bound, the transition probabilities and the ordering of the molecular electronic states in energy can be obtained via a molecular orbital picture of the Co^+ open valence shell without regard to

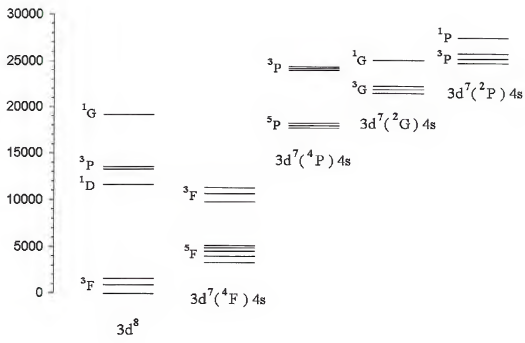

Figure 4-1.Low lying electronic states of free Co^+

the nature of the ligand. The properties of the molecular electronic states and transitions between them thus relate directly to the atomic ion state from which it was built. This description of the electronic structure of the complex ion as that of the perturbed atom is valid for all members of our homologous series.

The many-electron atomic states can be labeled by the Russell-Saunders term symbol that indicates the resultant orbital and spin angular momentum of the entire atom as $^{2S+1}\mathbf{L}$. If the spin-orbit interaction is zero, the energies of the (2S+1)(2L+1) total angular momentum states arising from a given term would all be degenerate. The low lying atomic terms of two electronic configurations the Co^+ ion are shown in figure 4-1.

The splitting of the J=L+S states from a given term is apparent even on the scale of figure 4-1, but in general is still less than the separation of the terms themselves, so the state description in terms of the total spin and orbital quantum numbers L and S is somewhat valid. Thus, initially we ignore the presence of even first-order spin-orbit interaction in our discussion of the electronic structure of our ion complexes.

The atomic wavefunction can be approximated as a product of one-electron wavefunctions, or at least a finite linear combination of them. In this case the spin and orbital angular momentum (as well as principle quantum number) of each electron is taken into account individually. Thus the atomic wavefunction looks like:

$$|\Psi(L,S,J,M_L,M_s,M_J)> = \sum_{\gamma} C_\gamma [|\psi(l_1,s_1,m_{l1},m_{s1})>|\psi(l_2,s_2,m_{l2},m_{s2})>|\psi(l_3,s_3,m_{l3},m_{s3})>...] \quad (4\text{-}4)$$

The wavefunction on the left represents the L·S coupled basis which is exactly valid for the atomic ion in the limit of zero spin-orbit interaction. The following will use the notation

$$|\Psi(L,S,J,M_L,M_s,M_J)> = |\ ^{2S+1}L_J,\ M_L,\ M_S> \qquad ; \qquad M_J = M_L + M_S \quad (4\text{-}5)$$

as a description of the coupled basis wavefunctions.

The wavefunctions in the linear combination on the right of eqn. 4-4 are the properly assymetrized uncoupled basis functions, which are the stationary states of the atom in the limit of large spin-orbit interaction, or, in a strongly cylindrically-symmetric external perturbation and no correlation. The product on the right runs over all the electrons in the atomic ion and each of the spins of electrons is of course $s_i = 1/2$.

If we ignore closed shells, the electronic configuration of the ground state of the Co^+ ion is $3d^8$ and we can describe the uncoupled basis functions for this configuration by the quantum numbers of their d-holes. It is clear that the states resulting from two d-electrons and two d-holes are the same. As an example of a d^8 configuration, consider both the d holes aligned along the z axis ($m_l = 0$), then the uncoupled basis representation of that state is:

$$[\,|\,2,\ 1/2,\ 0,\ 1/2\rangle|2,\ 1/2,\ 0,-1/2\rangle\,] \quad = |0^+,\ 0^-\rangle \quad = \quad |\underline{\uparrow\downarrow}\ \underline{\uparrow\downarrow}\ \underline{\ \ }\ \underline{\uparrow\downarrow}\ \underline{\uparrow\downarrow}\,\rangle$$

$$\delta\ \ \pi\ \ \sigma\ \ \pi\ \ \delta$$

$$m_l = \quad 2\ \ 1\ \ 0\ \ -1\ \ -2$$

This particular uncoupled representation of the atom ends up in more than one of the atomic terms, hence the sum in eqn. 4-4. A term which can be described by a single uncoupled representation in a given configuration is that of a 'stretched state', where the projections of M_L and M_S have their maximum value. The stretched singlet state of this configuration is $|2^+,\ 2\rangle = |\,^1G\ M_L = 4,\ M_S = 0\rangle$, and the stretched triplet state is $|2^+,\ 1^+\rangle = |\,^3F\ M_L = 3,\ M_S = 1\rangle$. The coefficients of the sum in the relationship between the coupled and uncoupled representation of the atomic wavefunctions can be obtatined by the operation of the angular momentum ladder operators [41-42]. The eigenfunctions of the coupled terms of the atom are related to the uncoupled basis by the expansion coefficients $C\gamma$ which can be determined from the values in Table 4-3 for the d^8/d^2 valence configuration. For convenience, the overall phase of the atomic wavefunctions has been chosen so as to make all the coefficients $C\gamma$ real numbers. The entries in Table 4-3 are in fact the square of the coefficients $C\gamma$ times the sign of the original coefficient, or

$C\gamma\text{^}3/|C\gamma|$. This makes printing all the square roots unnecessary. It also makes the sum of the magnitudes of the entries in Table 4-3 for any row or column equal to unity by the orthonormality of the wavefunctions in both the coupled and uncoupled basis.

The values in Table 4-3 are significant because the way in which they relate the wavefunction of the unperturbed (free) d^8 Co^+ atom to the wavefunction of the electrostatic complex. In the free ion and with no spin-orbit interaction, the energy of the system is determined from the values of the total orbital angular momentum L and the total spin angular momentum S. The orientation of the atomic wavefunction in space is determined by M_L and M_S. The total angular momentum J and its orientation in space M_J are also good quantum numbers in this case and this wavefunction is represented by rows in Table 4-3. When the atomic ion is distorted into $C_{\infty v}$ symmetry from spherical symmetry, i.e. distorted from free ion to the ion in a linear complex, the resultant angular momentum vectors L, S, and J are no longer constants of the motion, and are no longer represented by 'good' quantum numbers. In cylindrical symmetry only the projections of the resultant angular momentum vectors of the free atom remain good quantum numbers. In molecular nomenclature, the projection M_L becomes Λ, the projection M_S becomes Σ, and the projection M_J becomes Ω. Thus, if no covalent interaction exist in the complex, the free atomic energy levels split upon linear complexation in a way that is analogous to the splitting of the states in a homogeneously applied electric field.

In the linear complex, the electrons in d orbitals of the metal are oriented in three different directions with respect to the ligand direction, and thus will have different energies depending on this orientation; this is the basis for ligand field theory in inorganic

Table 4-3. The expansion coefficients C_γ^3 / $|C_\gamma|$ relating the coupled and uncoupled basis for a d^8 atom, see equation 4-4

d^2/d^8	2^+1^+	2^+0^+	1^+0^+	2^+-1^+	1^+-1^+	2^+-2^+	2^+2^-	2^+1^-	2^-2^+	2^+0^-	2^-0^+	1^+1^-
^{3}F 3 1	1											
^{3}F 2 1		1										
^{3}F 1 1			2/5	3/5								
^{3}P 1 1			3/5	-2/5								
^{3}F 0 1					4/5	1/5						
^{3}P 0 1					1/5	-4/5						
^{1}G 4 0							1					
^{1}G 3 0								1/2	-1/2			
^{3}F 3 0								1/2	1/2			
^{1}G 2 0										3/14	-3/14	8/14
^{3}F 2 0										1/2	1/2	0
^{1}D 2 0										-2/7	2/7	3/7

d^2/d^8	1^+0^-	1^-0^+	2^+1^-	2^--1^+	0^+0^-	1^+-1^-	1^--1^+	2^+2^-	2^-2^+
^{1}G 1 0	6/14	-6/14	1/14	-1/14					
^{3}F 1 0	2/10	2/10	3/10	3/10					
^{1}D 1 0	1/14	-1/14	-6/14	6/14					
^{3}P 1 0	3/10	3/10	-2/10	-2/10					
^{1}G 0 0					36/70	16/70	-16/70	1/70	-1/70
^{3}F 0 0					0	4/10	4/10	1/10	1/10
^{1}D 0 0					4/14	-1/14	1/14	-4/14	4/14
^{3}P 0 0					0	1/10	1/10	-4/10	-4/10
^{1}S 0 0					1/5	-1/5	1/5	1/5	-1/5

chemistry [43]. The importance of these anisotropic interactions of the orbitals with a ligand has been used to analyze the spectra of transition metal containing diatomic molecules before [44, 45]. The description of the wavefunction of the electrons on the metal center is best described by the rows of Table 4-3, as it is the orientation of the individual electrons orbit with respect to the ligand that determine the repulsive or attractive behavior of the interaction.

Table 4-3 relates the wavefunction of the free ion to a description of the ion distorted in the field of an electrostatic ligand, and thus allows the determination of the perturbation of the atomic ion energy levels upon complexation. With the z axis taken as the quantization and symmetry axis of the molecule, the d_{z^2} orbital ($d\sigma, m_l=0$) will have the most metal-ligand overlap and thus interaction upon molecular bonding. The d_{xz} and d_{yz} orbitals ($d\pi$, $|m_l|=1$) have somewhat reduced overlap, but should remain degenerate with each other in cylindrical symmetry. The same can be said of the $d_{x^2-y^2}$ and d_{xy} orbitals ($d\delta$, $|m_l|=2$). Thus the energy of the complex will depend on the occupation numbers of the $d\sigma$, $d\pi$, and $d\delta$ orbitals, $n_{d\sigma}$, $n_{d\pi}$, and $n_{d\delta}$. We will use the convention that $n_{d\sigma}$, $n_{d\pi}$, and $n_{d\delta}$ represent the **d-hole populations** in our discussion of Co^+. In other words, the total electronic energy of the cobalt ion complex is approximately:

$$E_{complex} = T(\,^{2S+1}L\,;\,Co^{+}) + T(\text{ligand}) + E_{electrostatic}(r) + E_{XF}(n_{d\sigma}, n_{d\pi}, n_{d\delta}) \quad (4\text{-}6)$$

The term E_{XF}, the crystal field energy, is of great importance in a variety of inorganic coordination compounds, and may be determined from our experimental studies for these simple complexes for the first time. The simplest functional form of the crystal field energy is linear in hole populations

$$E_{XF}(n_{d\sigma}, n_{d\pi}, n_{d\delta}) = E_{\sigma}n_{d\sigma} + E_{\pi}n_{d\pi} + E_{\delta}n_{d\delta} \quad (4\text{-}7)$$

which is a two parameter linear function of the populations since

$$E_\sigma + 2E_\pi + 2E_\delta = 0 \quad ; \quad E_\pi = -\frac{E_\sigma + 2E_\delta}{2} \tag{4-8}$$

so that the interaction of a closed shell is included in the electrostatic term only.

Ballhausen and Jorgensen suggest that the crystal field splitting parameters (at most 5, one for each d orbital) may be further reduced by symmetry to just one parameter, Dq. They suggest for a linear molecule of coordination number one:

$$E_{XF}(n_{d\sigma}, n_{d\pi}, n_{d\delta}) = (-5.14Dq)\, n_{d\sigma} + (-0.57Dq)\, n_{d\pi} + (3.14Dq)\, n_{d\delta} \tag{4-9}$$

Usually in inorganic coordination complexes the crystal field is in nature repulsive and the value Dq is taken as positive and this convention has been preserved in eqn. 4-9. Sometimes, when the interaction between the metal d electrons and the ligand is favorable (covalent), the energy ordering of the states is reversed and Dq is negative. The latter can be seen in the case of CoH [47] and CoF [48], where the ground states of those molecules arising from the Co^+ ^3F d^8 is $^3\Phi$ and not $^3\Delta$ since in these covalent compounds $E_\sigma > E_\delta$ and the occupation of a **σ hole** is unfavorable. For the Co^+-ligand complexes in this study, the d-overlap with the ligand electrons is repulsive and $E_\sigma < E_\delta$, and therefore σ holes are favored energetically over all others.

Table 4-4 shows the d-hole population of an atom in a d^8 electronic configuration distorted into $C_{\infty v}$ symmetry. These are simply calculated from the coefficients found in Table 4-3. The last column is the calculated relative crystal field energy of a given

Table 4-4. d-hole populations for the d^8 terms of linear complexes of Co^+.

d^8	Molecular State (linear)	d-hole population			Relative Xtal Field Energy (Dq)
		σ	π	δ	
^1S	$^1\Sigma$	2/5	4/5	4/5	0.00
^1G	$^1\Gamma$	0	0	2	6.28
	$^1\Phi$	0	1	1	2.57
	$^1\Delta$	3/7	8/7	3/7	-1.51
	$^1\Pi$	6/7	1	1/7	-4.53
	$^1\Sigma$	36/35	32/35	2/35	-5.63
^3P	$^3\Sigma$	0	2/5	8/5	4.80
	$^3\Pi$	3/5	1	2/5	-2.40
^1D	$^1\Pi$	1/7	1	6/7	1.39
	$^1\Sigma$	4/7	2/7	8/7	0.49
	$^1\Delta$	4/7	6/7	4/7	-1.63
^3F	$^3\Phi$	0	1	1	2.57
	$^3\Sigma$	0	8/5	2/5	0.34
	$^3\Pi$	2/5	1	3/5	-0.74
	$^3\Delta$	1	0	1	-2.00

molecular state from the d-hole population and eqn. 4-9. As the actual energy differences between the terms is much larger that the crystal field energy the states are ordered by term energy and then crystal field energy. The ground state of free Co^+ is $^3F\ 3d^8$ therefore, the ground state of any linear electrostatic complex of Co^+ is predicted to be $^3\Delta$, as observed. This state is simple in that it consists of a single basis function in both the coupled and uncoupled basis,

$$|^3F,\ 2,\ 1\rangle = |2^+,\ 0^+\rangle = |\ \underline{\downarrow}\ \ \uparrow\downarrow\ \ \underline{\ \ }\ \ \underline{\downarrow}\ \ \uparrow\downarrow\ \ \uparrow\downarrow\ \rangle$$

and thus contains a full hole in both the dσ and dδ-orbitals.

The actual (experimental) binding energies of serveral electronic states of d^8 electrostatic complexes have been determined accurately for the first time in this study. Table 4-5 lists these binding energies and an analysis of the contribution from the

Table 4-5. Ligand field parameters as derived only from the experimental diabatic binding energies of the d^8 states of the $CoRg^+$ complexes [cm^{-1}] through the direct application of eqns 4-6 through 4-9.

		Ar	Kr	Xe
Experimental Diabatic Binding Energies	$D_0(^3\Delta)$	-4111	-5500	-8000
	$D_0(^1\Delta)$	-3210	-4598	-7100
	$D_0(^3\Pi)$	-2816	-4000	-6250
Crystal Field (2 Parameter) {eqn 4-9}	E_{elect}	-4485	-6347	-9433
	Dq	-550	-820	-1153
Ligand Field (4 Parameter) {eqn 4-6}	E_{elect}	-3758	-5553	-8560
	Eσ	1043	2265	3780
	Eπ	875	1079	1330
	Eδ	-1396	-2212	-3758

application of eqns. 4-6 through 4-9. Perusal of the entries of table 4-5 lays tribute to an unfortunate limitation of eqn. 4-6. This brute force method inaccurately predicts that hole population in the dσ-orbital destabilizes the crystal field energy whereas hole population in the dδ-orbital is the biggest contributor to the crystal field stabilization energy. Additional failures include the obvious overestimation of the electrostatic term (greater than the bond

energy) and in the crystal field treatments and the sign of Dq is wrong for inductively bound complexes.

An obvious error associated with the above analysis is the assumption of a constant electrostatic interaction which was determined for each molecule through parameterization. Equation 4-6 hints of the radial dependence of this term which is inversely proportional to the fourth power of interatomic separation and clearly changes from state to state. Analytically solving the electrostatic energy (eqn. 4-2) and representing this as a state selective constant in eqn. 4-6 allows the reparameterization of the crystal fields (Table 4-6). Unfortunately, only two states ($^1\Delta$ and $^3\Delta$) in two of the three molecules ($CoAr^+$ and $CoKr^+$) have the measured bond lengths and bond strengths required to provide this new parameterization for the $CoRG^+$ states derived from d^8 Co^+ atomic configurations.

From the entries of Table 4-6 the successes of this modified model is obvious. The signs of both the ligand field and crystal field parameters are qualitatively correct with the greatest ligand field stabilization observed in the Eσ term (greatest hole population in the dσ-orbital). Additionally the sign of Dq is positive as is expected for inductively bound complexes. The incorporation of the observed bond lengths and thus the measured electrostatic interaction into the above model is clearly warranted as the electrostatic contribution to the binding energy is state selective.

The entries in the final rows of Table 4-6 represent the energy differences associated with the spatial orientation of the d-orbitals. It is interesting that when going from Ar to Kr, the effects of the different orientations and occupations appear to "soften".

The absolute value of the ligand field energies tend to decrease as well as Dq. This is probably due to the increased polarizability of krypton. As the size of the bonding partner increases, the ability of the electronic cloud to deform increases and begins to wash out the "lumpy" open-shelled nature of the transition metal atomic ion.

Table 4-6. Ligand field parameters for two states of $Co^+Ar(Kr)$ as derived from eqns. 4-6 through 4-9. The electrostatic contribution to the binding is explicitly determined from the bond lengths and eqn. 4-2 and used as a state selective constant as opposed to an averaged molecular constant determined through parameterization.

		Co^+·Ar	Co^+·Kr
$^3\Delta$	Bond Energy (cm^{-1})	-4111	-5500
	Bond Length (Å)	2.385	2.447
	$E_{electrostatic}$ (cm^{-1})	-2674	-4082
$^1\Delta$	Bond Energy (cm^{-1})	-3210	-4598
	Bond Length (Å)	2.458	2.452
	$E_{electrostatic}$ (cm^{-1})	-2370	-4048
Crystal Field (cm^{-1}) (1 parameter) {eqn 4-9}			
	Dq	617	523
Ligand Field (cm^{-1}) (3 parameter) {eqn 4-6}	Eσ	-2917	-2228
	Eπ	-22	304
	Eδ	1480	810

$CoRG^+$

Overview

The resonant photodissociation spectrum of $CoAr^+$ in the region of 12 400 cm^{-1} to 17 400 cm^{-1} can be seen in fig. 4-2. The $CoAr^+$ spectrum has been split into two traces in order to maintain the resolution of the figure and to provide the entire observed spectrum. The bands in each electronic transition are labeled by their upper state vibrational quantum number. Due to the supersonic expansion the ions suffer prior to photo-interrogation, all transitions originate from the $v'' = 0$ level of the ground electronic state. Long vibronic progressions which lead to dissociation in four of the five electronic states is evident from fig. 4-2. This is indicative of a large geometry change which occurs upon photon absorption in these four electronic transitions. The **a**-X transition, which contains a progression of only two bands, implies an upper state of similar geometry to the ground state.

Completely analogous to the $CoAr^+$ spectrum of fig. 4-2 are the spectra of $CoKr^+$ and $CoXe^+$. Figure 4-3 provides a portion of the $Co^{84}Kr^+$ spectrum and fig. 4-4 displays the resonant visible spectrum of $Co^{129}Xe^+$. Progressions in both spectra have been labeled by upper state vibrational quantum number, however, the identity of the vibrational quantum numbers in the latter two are unambiguous as both krypton and xenon possess naturally occurring isotopes of sufficient abundance to be observed in photodissociation. The action of these naturally occurring isotopic variants are simultaneously monitored and the isotopic shifts utilized to acquire the absolute vibrational quantum numbering.

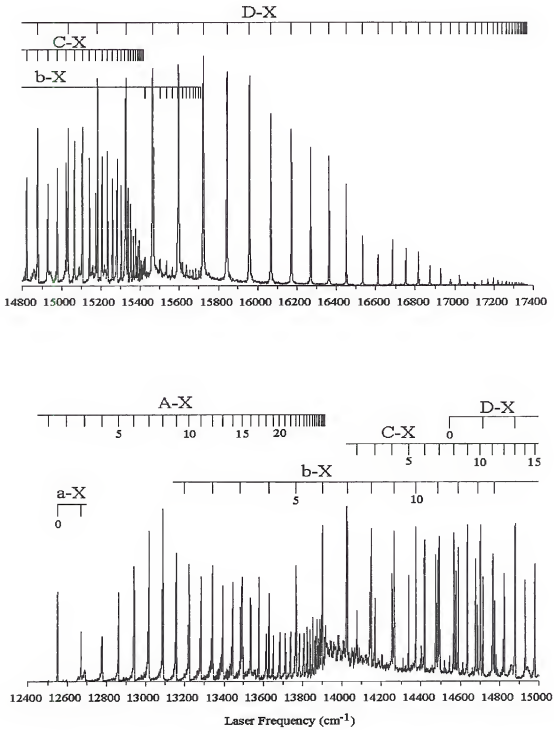

Figure 4-2. The full visible spectrum of $CoAr^+$.

Tick marks above the spectrum label the upper state vibrational quantum number of the transition. Notice a portion in each trace is repeated for continuity.

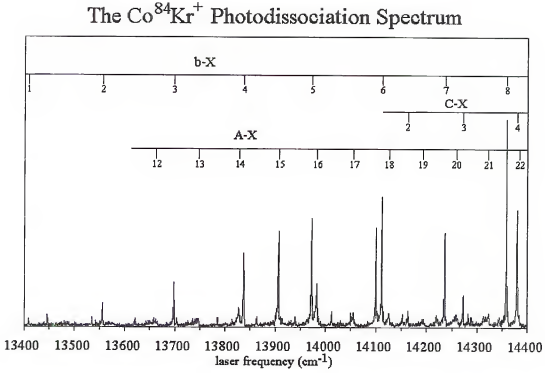

Figure 4-3. A portion of the $Co^{84}Kr^+$ photodissociation spectrum.

Tables 4-7 through 4-9 list the line positions of resonant transitions observed in each of the ionic complexes and were fit to the anharmonic oscillator of eqn. 3-1. Transitions approaching a dissociation limit were not included in the fit and the vibrational constants extracted from this formula have been presented in Table 4-10 along with those obtained for similar Co^+·ligand complexes. The vibrational analysis of resonant transitions in the $CoRG^+$ complexes were done in similar fashion to that presented for the group 5-metal-xenon ionic complexes of chapter 3. Figure 4-5 displays the transition frequencies of 'cold band' transitions in $CoAr^+$ plotted against upper state vibrational quantum

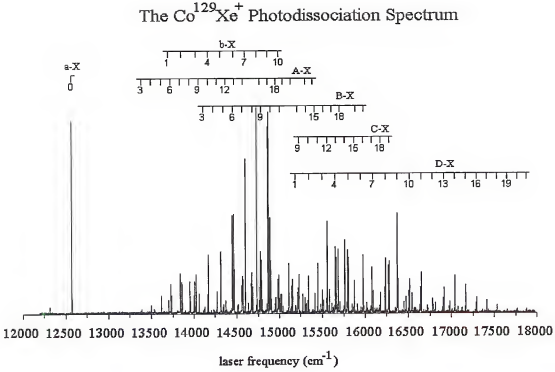

Figure 4-4. The photodissociation spectrum of $Co^{129}Xe^{+}$.

number, $(v' + ½)$. The symbols represent observed data (Table 4-7) and the solid curve calculated based on formula 3-1 and the constants of table 4-10. The solid lines at the right of the figure label the atomic state of the Co^{+} fragment at dissociation. The energies of these atomic states have been offset by the $CoAr^{+}$ ground state binding energy (4111 cm^{-1}). It is evident from fig. 4-5 that the atomic state assignments of the dissociated fragments is clearly correct and that the two term anharmonic oscillator (eqn. 3-1) consistently underestimates the true binding energy of this class of weakly bound molecules. The term value plots for the resonant 'cold band' transitions of $CoKr^{+}$ and $CoXe^{+}$ are presented in figs. 4-6 and 4-7. Unfortunately, as the binding energies of these

Table 4-7. Observed cold band positions (cm^{-1}) in $CoAr^+$.

v'+1/2	a-X	b-X	A-X	C-X	D-X
0.5	12552.02				14545.79
1.5	12672.35	13198.42	12505.01		14715.71
2.5		13344.89	12600.25	14077.51	14880.21
3.5		13485.80	12691.17	14168.66	15034.85
4.5		13629.76	12778.37	14255.72	15184.95
5.5		13768.13	12862.91	14339.40	15328.66
6.5		13902.28	12942.52	14419.23	15465.93
7.5		14027.89	13018.24	14495.65	15598.07
8.5		14150.39	13089.99	14568.41	15724.28
9.5		14266.67	13158.26	14637.70	15844.73
10.5		14376.47	13223.29	14703.32	15959.72
11.5		14489.35	13284.46	14765.22	16068.97
12.5		14591.06	13342.16	14824.00	16172.52
13.5		14688.85	13396.12	14880.21	16270.95
14.5		14775.27	13446.87	14931.28	16364.40
15.5			13494.45	14979.98	16452.29
16.5			13538.75	15025.62	16534.97
17.5			13579.72	15067.74	16612.81
18.5			13616.42	15107.42	16685.61
19.5			13652.83	15143.35	16753.63
20.5			13685.02	15177.03	16816.86
21.5			13713.87	15207.94	16875.30
22.5			13740.70	15236.06	16929.40
23.5			13768.13	15261.50	16978.66
24.5		15425.07	13787.40	15284.95	17024.56
25.5			13806.91	15305.30	17065.66
26.5		15502.47	13824.34	15323.19	17103.82
27.5		15535.89	13839.64	15340.47	17138.00
28.5		15565.50	13853.10	15354.81	17168.71
29.5		15592.29	13864.83	15367.69	17196.23
30.5		15616.21	13875.00	15378.74	17220.67
31.5		15637.30	13883.73	15388.19	17242.32
32.5		15655.93	13891.25	15396.29	17261.63
33.5		15672.24	13897.44	15403.16	17278.42

Table 4-7. Observed cold band positions (cm^{-1}) in $CoAr^+$ (continued)

v'+1/2	a-X	b-X	A-X	C-X	D-X
34.5		15686.71	13903.43	15409.03	17293.27
35.5		15699.09	13907.92	15413.90	17306.31
36.5		15709.94	13911.42	15417.75	17317.43
37.5			13914.35	15421.03	17327.13
38.5					17335.31
39.5					17342.21
40.5					17347.97
41.5					17351.93
42.5					17356.88
43.5					17359.15
44.5					17362.63
45.5					17363.62
46.5					17366.22

Table 4-8. Observed cold band positions (cm^{-1}) in $Co^{84}Kr^{+}$.

v'+1/2	a-X	b-X	A-X	C-X	D-X
0.5	12553.52				
1.5		13409.17			
2.5		13556.45		14163.28	
3.5		13698.09		14272.78	
4.5		13837.45		14379.67	15355.97
5.5		13972.91		14483.46	15497.43
6.5		14111.83		14585.59	15635.43
7.5		14236.14		14684.72	15769.80
8.5		14359.10		14781.03	15900.93
9.5		14491.03		14875.01	16027.53
10.5		14607.24		14967.12	16152.15
11.5		14730.46		15053.29	16273.91
12.5		14841.90	13662.52	15140.77	16390.78
13.5			13747.69	15225.02	16504.80
14.5		15065.62	13828.34	15306.93	16616.41
15.5		15168.82	13907.25	15386.24	16723.13
16.5		15270.36	13982.89	15464.28	16827.65
17.5		15370.07	14055.58	15534.19	16929.16
18.5			14126.35	15606.38	17026.88
19.5			14193.53	15675.82	17122.19
20.5			14259.36	15744.82	17213.90
21.5			14322.84	15805.42	17301.72
22.5			14384.17	15866.50	17387.03
23.5			14443.02	15927.15	17468.84
24.5			14499.07	15982.56	17547.75
25.5			14551.71	16034.37	17624.06
26.5			14604.16	16085.57	17696.67
27.5			14656.87	16136.38	17766.68
28.5				16184.69	17833.29
29.5			14744.52	16228.10	17897.10
30.5				16271.25	17957.51
31.5			14826.01	16312.31	
32.5			14865.70	16351.31	
33.5			14901.84	16388.12	
34.5			14935.70	16422.22	
35.5			14968.21	16455.13	
36.5			14998.02		
37.5			15030.30		

Table 4-9. Observed cold band positions (cm^{-1}) in $Co^{129}Xe^{+}$.

v'+1/2	a-X	b-X	A-X	B-X	C-X	D-X
0.5	12574.74					
1.5		13705.53				15190.55
2.5		13863.25				15347.18
3.5		14025.37	13389.50			15500.74
4.5		14172.57	13504.12	14110.71		15652.18
5.5		14318.44	13621.47	14228.72		15802.08
6.5		14468.49	13733.92	14344.98		15948.33
7.5		14605.42	13844.98	14459.64		16093.11
8.5		14741.26	13954.58	14572.66		16236.16
9.5		14869.54	14062.70	14684.21	15225.98	16376.54
10.5		14997.27	14168.99	14794.11	15339.67	16513.76
11.5			14273.24	14902.30	15450.56	16649.35
12.5			14376.13		15559.21	16782.86
13.5			14476.95	15008.53	15662.65	16913.45
14.5			14576.38	15216.91	15765.45	17042.10
15.5				15318.44	15871.11	17168.49
16.5			14769.79	15417.33	15974.88	17292.89
17.5			14863.94	15516.40	16076.74	17414.57
18.5			14956.33	15612.99	16176.74	17534.16
19.5			15046.08		16276.17	17651.52
20.5			15134.65	15707.62		17766.57
21.5				15891.85		17878.19
22.5			15306.32	15981.43		
23.5			15389.30			

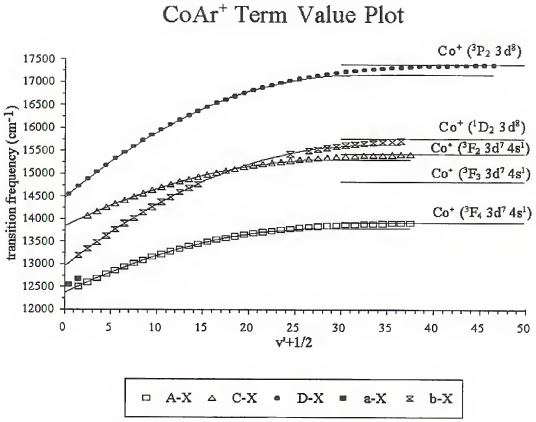

Figure 4-5. The $CoAr^+$ term value plot.

The symbols represent the observed data while the solid curves provide the best fit of the data to the anharmonic oscillator. The horizontal lines at the immediate right of the figure provide the terms of the dissociated fragment Co^+ which are at energies offset by the ground state binding energy.

complexes increase there is an apparent decrease in Franck-Condon overlap with the higher vibrational levels of the various electronic transitions. For $CoXe^+$, this overlap is so poor that no direct observation of a band convergence was possible. Therefore, the dissociation limits of the excited states were determined through long extrapolations of the anharmonic oscillator (eqn. 3-1). The lower block of fig. 4-7 shows the long extrapolation to dissociation in $CoXe^+$. The ground state binding energy (8000 ± 200 cm^{-1}) was chosen

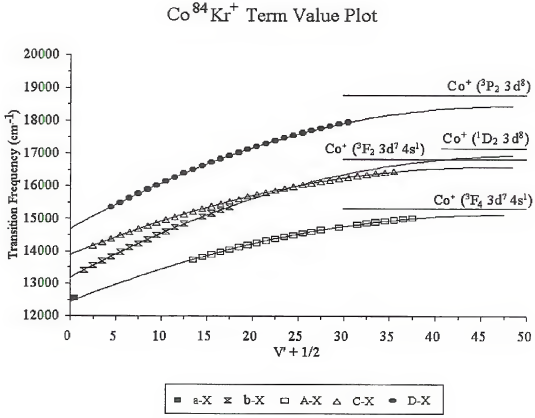

Figure 4-6. The $Co^{84}Kr^+$ term value plot.

The symbols represent observed resonant transitions and the solid lines calculated from eqn. 3-1 and the constants of table 4-10. The actual diabatic dissociation energies are at frequencies given by the horizontal lines on the right and these label the excited state Co^+ term at dissociation.

to be consistent with the systematic underestimation (~8 %) [16] of eqn. 3-1 to the true dissociation energies.

A more precise method for obtaining dissociation energies has been presented by Leroy and Bernstein [21]. In this treatment, the long-ranged forces present at dissociation are explicitly considered in the description of the vibrational structure approaching a limit.

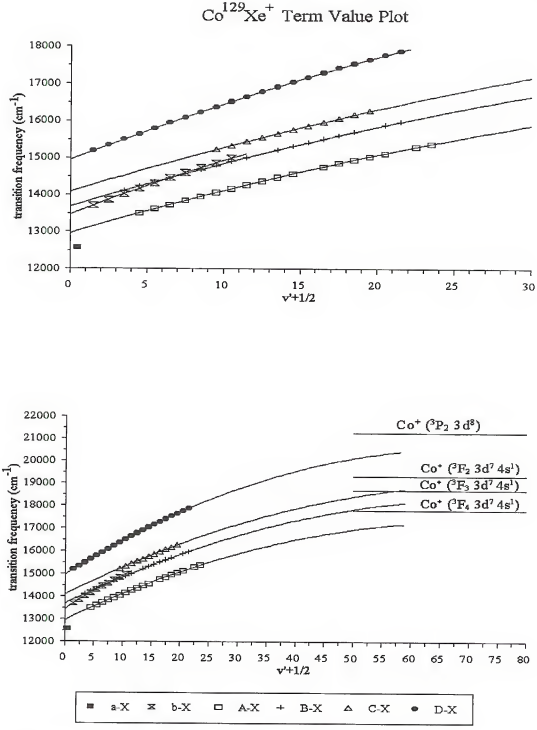

Figure 4-7. Term value plots for $Co^{129}Xe^{+}$.

The top trace shows a highlight of the lower. The lower block shows the long extrapolation to dissociation. The systematic underestimation of the two parameter anharmonic oscillator to the true dissociation energies was used to provide a better estimate to the ground state binding energy which in turn provides estimates to the diabatic binding energies of these excited states.

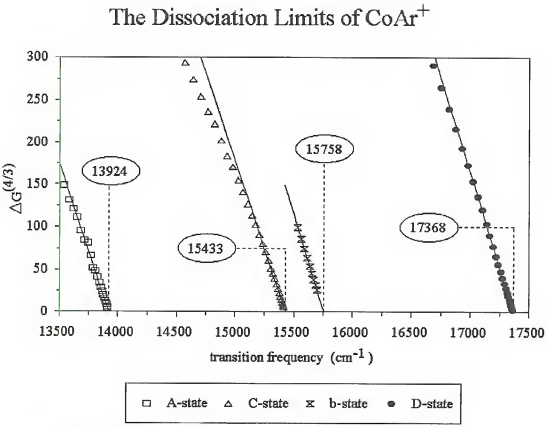

Figure 4-8. The Leroy-Bernstein analysis of $CoAr^+$.

For $CoRG^+$, this force is charge-induced dipole and is dependent on the polarizability of the rare gas (Table 4-1). This protocol has successfully been applied to the group 5 metal-xenides of chapter 3 and application of eqns. 3-2 and 3-3 to transitions approaching a band convergence result in a linear relationship which may be extrapolated to obtain the diabatic dissociation energies of the excited states. Figures 4-8 and 4-9 show the LB treatment applied to various excited states of $CoAr^+$ and $CoKr^+$. The ground state binding energy is obtained from these extrapolated values and the known energies of the atomic transitions of Co^+ (fig. 4-1) and for $CoAr^+$, this is 4111 cm^{-1}. The extrapolations of fig. 4-9 are

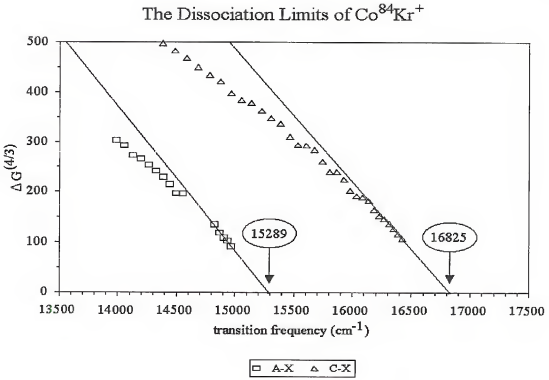

Figure 4-9. The Leroy-Bernstein analysis applied to $Co^{84}Kr^+$.

The symbols represent observed transitions and the solid lines calculated from eqn 3-2. Since a long extrapolation to the horizontal axis was required, the slope of the linear extrapolation was set to the theoretical limiting slope (eqn 3-3). The x-axis intersection provides a measure of the diabatic binding energy of each state.

substantially longer than those for $CoAr^+$ and are due to poor Franck-Condon overlap with the higher bound vibrational levels of $CoKr^+$. The slope of the extrapolations of fig 4-9 was predetermined through eqn 3-3 and the intercepts provide a ground state bond dissociation energy for $Co^{84}Kr^+$ of 5500 cm^{-1}. Once the ground state binding energy has been established, the dissociation energy of each state can subsequently be determined through:

$$D_0'_{(complex)} = D_0''_{(complex)} + \Delta E_{atomic} - T_{00}'_{(complex)} \qquad (4\text{-}10)$$

where ΔE_{atomic} is the energy of the atomic state known to derive the complex. The excited

state dissociation energies are simply the difference between the diabatic limit and the state's electronic origin (T_{00}). These results are provided in Table 4-10.

Transitions in the a-X system

Figure 4-10 shows both members of the vibrational progression observed in the a-X system of $CoAr^+$. Both members have been rotationally resolved and fig. 4-10 shows

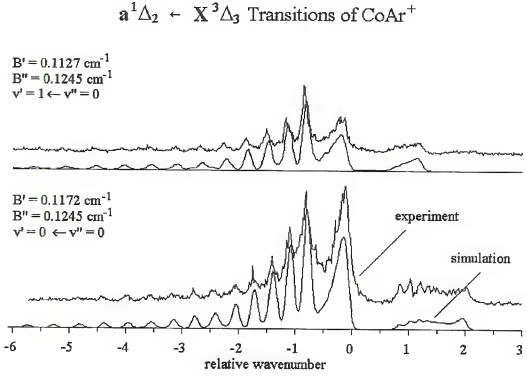

Figure 4-10. The rotationally resolved members of the a-X system.

Only the origin (lower trace) and first vibronic band (upper trace) of the a-X system were of sufficient intensity to suffer rotational analysis. Both traces have been offset by their band origins which align with 0 relative wavenumbers.

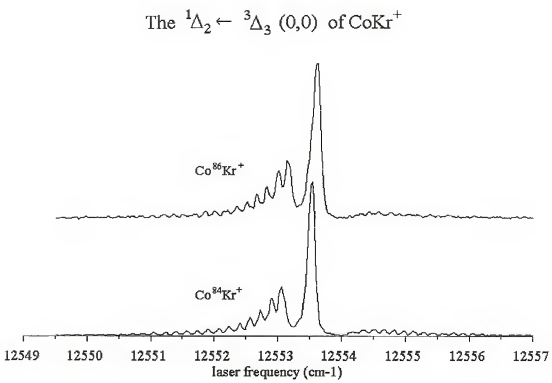

Figure 4-11. The a $^1\Delta_2$ - X $^3\Delta_3$ (0,0) origin band contour.

The band contour of the most abundant naturally occurring isotopes of $CoKr^+$. The slight blue shift of the heavier isotopomer verifies the origin assignment. The top trace was scaled by the ratio of the natural isotopic abundances of krypton.

experiment and simulated contours of the rotational structure of each of these bands. The rotational simulations of fig. 4-10 assumes $CoAr^+$ acts as a symmetric top, rigid rotor undergoing a perpendicular transition with the total angular momentum decreasing upon photon absorption ($\Delta\Omega = -1$). Furthermore, the simulations of fig. 4-10 are calculated based on a lower state assignment of $\Omega'' = 3$ and rotational constant $B'' = 0.1245$ cm^{-1}. The upper state rotational constants are provided in the figure and from these the

vibrationally averaged bond lengths of the origins of both the ground ($^3\Delta_3$) and excited a-state ($^1\Delta_2$) are calculated as 2.385 ± 0.005 Å and 2.458 ± 0.005 Å (table 4-10). Figure 4-11 provides the analogous **a-X** band system in the two most abundant naturally occurring isotopes of $CoKr^+$. The origin is the only member of this vibronic progression and the only band in $CoKr^+$ to suffer rotational analysis. Figure 4-11 shows the rotational structure of the **a** $^1\Delta_2 \leftarrow$ **X** $^3\Delta_3$ (0,0) transition. The intensity of the top trace of figure 4-11 ($Co^{86}Kr^+$) has been scaled by the ratio of the naturally occurring krypton isotopes and is the reason for the apparent diminished signal to noise relative to the (unscaled) lower trace ($Co^{84}Kr^+$). The slight blue shift of the heavier isotopomer verifies the vibrational (origin) assignment and suggests a greater vibrational frequency for the ground state relative to this state. The rotational structure of this band is composed of three branches with approximately equally spaced lines in the P and R branches and a sharp unresolved Q branch. This and the apparent Franck-Condon overlap, which peaks at the origin, is consistent the slight geometry change observed upon photo-excitation for this and all **a-X** $CoRG^+$ transitions.

The rotational contour of fig. 4-11 was simulated assuming $CoKr^+$ act as a rigid symmetric rotor undergoing a perpendicular transition ($\Omega' = 2 \leftarrow \Omega'' = 3$) and this simulation is reproduced in fig. 4-12 along with the $Co^{84}Kr^+$ band contour. The simulation reproduces the observed contour so well that the two traces appear superimposed. The rotational constants used to produce the calculated contour were $B_0'' = 0.0813$ cm^{-1} and $B_0' = 0.0810$ cm^{-1}, thus providing ground and excited state bond lengths of $r_0'' = 2.447$ Å

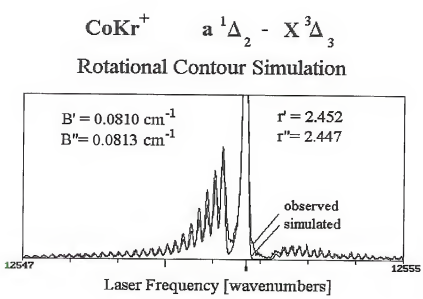

Figure 4-12. The experimental and simulated **a-X** origin.

The upper trace is the experimental spectrum and the lower trace is calculated using the above rotational constants and assuming $CoKr^+$ acts as a rigid symmetric rotor. The simulation reproduces the observed spectra and appears superimposed upon experiment.

and $r_0' = 2.452$ Å. The difference in bond lengths of these two states is only 0.2%. The $Co^{86}Kr^+$ contour was also simulated and used rotational constants $B_0'' = 0.0805$ cm^{-1} and $B_0' = 0.0802$ cm^{-1} which essentially scale from those of the lighter isotopomer by the ratio of the reduced masses.

The $\mathbf{a}\ ^1\Delta_2 \leftarrow X\ ^3\Delta_3$ (0,0) transition in $Co^{129}Xe^+$ is presented as the top trace in fig. 4-13. This band is obviously not as resolved as it was in $CoKr^+$ or $CoAr^+$ and is resolution

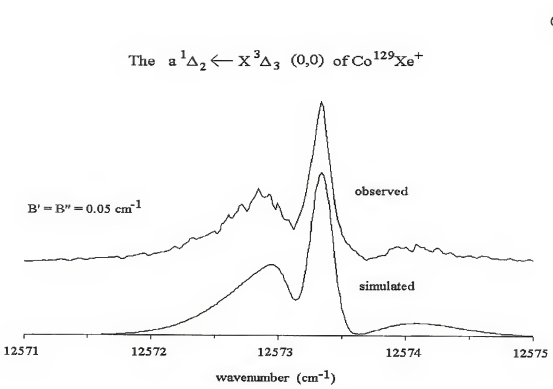

Figure 4-13. Observed and simulated rotational contour of the origin transition (0,0) of the $a^1\Delta_2 \leftarrow X\,^3\Delta_3$ band system of $Co^{129}Xe^+$.

Despite the limited resolution of this band when compared to those observed in the similar molecules $CoAr^+$ and $CoKr^+$, the simulation assures the accurate assignment of Ω and verifies that this transition is the $a^1\Delta_2 \leftarrow X\,^3\Delta_3$ common to all $CoRG^+$ complexes.

limited by the laser linewidth and pulsed laser power broadening. Nonetheless, the gaps between the unresolved branches are clearly evident and indicate the large unquenched angular momentum ($\Omega'' = 3$) of the ground state. The relative intensities of the P and R branches assign the decrease in angular momentum ($\Delta\Omega = -1$) upon photon absorption. Simulation of the unresolved contour (lower trace of fig. 4-13) provides rotational constants $B'' = B' = 0.05$ cm^{-1} which provide a measure of the bond lengths of the two states connected by this transition (2.9Å).

From the one electron eigenfunctions of Table 4-3 a prediction of the symmetry of the ground state was made which can now be verified. It was speculated that an ordering of the d^8 electronic states was possible, based on the degree of σ-orbital occupation. The Co^+ ground atomic state is a $3d^8\ ^3F$ which can support (among others) a $^3\Delta$ and $^3\Pi$ molecular state. The Δ state has a full σ-hole whereas the Π state has 2/5 of a σ-hole and therefore is expected to be less bound. The rotational simulations assures a lower state Ω value of 3 and this eliminates the possibility of a ground state with $^3\Pi$ symmetry. This simple analysis is fully supported by Bauschlicher's *ab initio* calculations [20].

The **a**-state has been assigned as a $^1\Delta_2$ deriving from the $3d^8$ ($^1D_2$). It is clear from the rotational structure that the assignment of d^8 is correct owing to the similar bond lengths of the states and the observed Franck-Condon overlap which peaks at the origin of the **a**-**X** systems. The simulations provide an upper state Ω assignment of $\Omega' = 2$. There are only two low-lying atomic d^8 configurations which can support molecular terms with $\Omega = 2$, these are the ^1D and ^3P which give rise to the $^1\Delta$ and $^3\Pi$. From fig. 4-1, these atomic states are separated by ~1600 cm^{-1} with the ^3P being higher. If the lineage of the a-state was the ^3P then the binding energy of this state would be greater than the ground and this is not supported by the eigenfunctions of table 4-3 or the bond lengths determined form the rotational simulation of figs. 4-11 through 4-13. In fact the only state which may be bound by more than the ground state is the $^1\Sigma$ deriving from the ^1G with a σ-hole occupation which is slightly greater than 1 (Table 4-4). In lieu of this, the **a**-state has been assigned the $^1\Delta_2$ deriving from the $^1D_2$ of Co^+.

Table 4-10. Results of the Co^+-ligand spectral analysis (cm^{-1} unless otherwise noted).

	$CoAr^+$	$CoKr^+$	$CoXe^+$	$CoOCO^+$	$CoNN^+$
State	**X** $^3\Delta_3$				
Atom	$^3F\ 3d^8$				
D_0	4111	5500	8000	7100	10 000
r_0 (Å)	2.385	2.447		3.174	
State	**a** ($^1\Delta_2$)				
Atom	$^1D_2\ 3d^8$ (11651.48)				
T_{00}	12552	12553	12575	12301	13299
ω_e	~120				
D_0	3210	4598	7100	6450	8000
r_0 (Å)	2.458	2.452		3.152	
α_e	0.0045				
k (N/m)	20.3				

State	**A** ($^3\Phi_4$)				
Atom	$^3F_4\ 3d^7 4s$ (9812.7)				
T_{00}	12410	12482	13027	12377	15500
ω_e	101	114	124	190	140
$\omega_e x_e$	1.77	1.22	0.88	2.22	1.24
D_0	1513	2831	4800	4500	4000
LB limit	13 924	15 289			
r_0 (Å)	2.817			3.340	
α_e	0.00213			0.00047	
k (N/m)	14.2	26.7	36.6	53.6	

Table 4-10. (Continued)

	$CoAr^+$	$CoKr^+$	$CoXe^+$	$CoOCO^+$	$CoNN^+$
State	**b** $^1\Pi_1$ (tentative)				
Atom	$^1D_2$ $3d^8$ (11651.48)				
T_{00}	13038	13261	13540		
ω_e	161	152	169		
$\omega_e x_e$	2.42	1.54	2.14		
D_0	2724	3890	6100		
LB limit	15 758				
r_0 (Å)	2.634				
α_e	0.00202				
k (N/m)	36.2	47.0	68.3		

State	**C** $^3\Pi_2$				
Atom	$^3F_2$ $3d^74s$ (11321.5)				
T_{00}	13889	13938	14148	13733	
ω_e	100	117	128	201	
$\omega_e x_e$	1.71	1.26	0.84	2.63	
D_0	1543	2883	5150	4700	
LB limit	15 433	16 825			
r_0 (Å)	2.806				
α_e	0.00205				
k (N/m)	14.1	27.8	39.2	60.0	

Table 4-10. (Continued)

	$CoAr^+$	$CoKr^+$	$CoXe^+$	$CoOCO^+$	$CoNN^+$
State	**D $^3\Pi_2$**				
Atom	$^3P_2$ $3d^8$ (13261.1)				
T_∞	14556	14761	15032	14975	
ω_e	170	157	161	205	
$\omega_e x_e$	2.69	1.65	1.15	1.64	
D_0	2816	4000	6250	5400	
LB limit	17 368				
r_0 (Å)					
k (N/m)	40.4	50.4	61.6	62.1	
State	**B**				
Atom	$^3F_3$ $3d^74s$ (11708.1)				
T_∞			13746		
ω_e			125		
$\omega_e x_e$			0.83		
D_0			4950		
r_0 (Å)					
k (N/m)			37.1		

The A-X and C-X transitions of $CoRG^+$

Long excited state progressions are evident in both the **A** and **C**-states in all three molecules. For $CoAr(Kr)^+$, transitions in both states terminate in band continuums as shown in figs. 4-2 and 4-5,6. The Leroy-Bernstein analysis of $CoAr^+$ assures that these states derive from atomic manifolds separated by 1508 cm^{-1} which is similar to the spin orbit splitting (1509 cm^{-1}) between the J = 2 and 4 levels of the ^3F atomic term. Therefore the **A** and **C**-states derive from the spin orbit split states $^3F_4$ and $^3F_2$ of the $[3d^7\ (^4F)\ 4s]\ ^3F$ Co^+ term as shown in figs. 4-5 through 4-7. The occupied 4s orbital which is present in the Co^+ chromophore in these states of all three ionic complexes becomes the defining characteristic of the bond and the shielding which it imposes on the 3d orbitals washes out the differences which would be attributable to the different spatial orientation of the occupied d-orbitals. The properties of these states are strikingly similar as can be seen in Table 4-10. Moreover, in fig. 4-14, $CoAr^+$ **A-X** transitions are plotted in the same manner as in the term value plot of fig. 4-5, but the frequency of transitions in the **C**-state have been shifted by the spin orbit splitting between the $^3F_4$ and $^3F_2$ (-1508.8 cm^{-1}) and replotted. It is clear from fig. 4-14 that the vibrational structure of these states is nearly identical and a consistent relative vibrational quantum numbering was chosen for transitions within these two states of $CoAr^+$.

Numerous bands within the **A** and **C**-states of $CoAr^+$ have been rotationally analyzed and figs. 4-15 and 4-16 display a small sampling of those. The upper and lower traces of fig. 4-15 show both the observed and simulated rotational structure of the

$A\ ^3\Phi_4 \leftarrow X\ ^3\Delta_3$ (14,0) and (13,0) bands. The rotational structure was simulated using the same lower state rotational constant ($B'' = 0.1245\ cm^{-1}$) as was used in the simulations of the $a\ ^1\Delta_2 \leftarrow X\ ^3\Delta_3$ (1,0) and (0,0) bands of $CoAr^+$ (fig. 4-10). The three traces of fig. 4-16 show the observed and simulated rotational contour of three bands observed in the $C\ ^3\Pi_2 \leftarrow X\ ^3\Delta_3$ system, namely the (15,0), (12,0), and the (5,0). The simulations of fig. 4-16

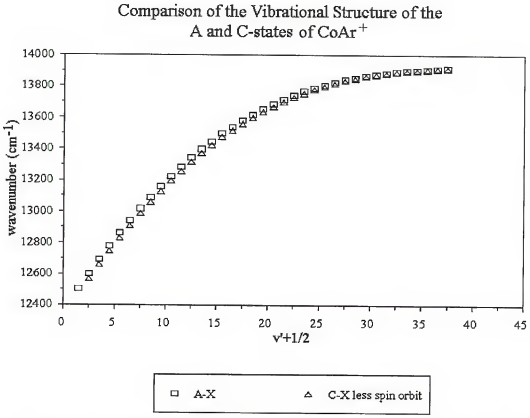

Figure 4-14. Comparison of the vibrational structure from states derived from the ^3F term of Co^+.

Transitions in the A-state are as how they appear in fig. 4-5. The spin orbit splitting has been subtracted from the frequency of resonant transitions within the C-state and this has the effect of overlaying the vibrational structure of each state.

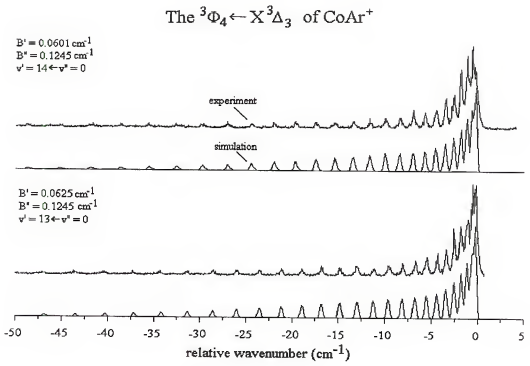
The $^3\Phi_4 \leftarrow X\,^3\Delta_3$ of $CoAr^+$
B' = 0.0601 cm-1
B" = 0.1245 cm-1
v' = 14 ← v" = 0
experiment
simulation
B' = 0.0625 cm-1
B" = 0.1245 cm-1
v' = 13 ← v" = 0
-50 -45 -40 -35 -30 -25 -20 -15 -10 -5 0 5
relative wavenumber (cm-1)

Figure 4-15. The observed and simulated rotational structure of the (14,0) and (13,0) bands of the A-state.

The simulation assumes that $CoAr^+$ acts as a symmetric top, rigid rotor undergoing a perpendicular transition ($\Omega' = 4 \leftarrow \Omega'' = 3$). The bands have been offset by the rotationless band origins which occur at 0 relative wavenumbers.

once again used the same lower state rotational constant as all simulations have. Upper state rotational constants have been extracted from the simulations and fit to the simple expression:

$$B_{v'} = B_e - \alpha_e (v'+1/2) \qquad (4\text{-}11)$$

The constants B_0 (r_0) and α_e were determined from eqn. 4-11 and are provided in Table 4-10. A significant change between upper and lower state bond lengths (r_0 of table 4-10) is

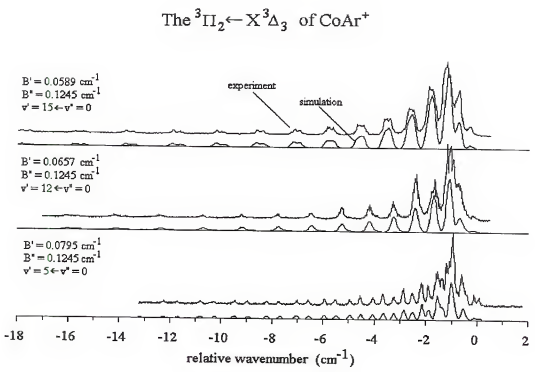

Figure 4-16. The observed and simulated rotational contour of three bands in the C-X system of $CoAr^+$.

The three traces correspond to three different bands with the rotationless band origins occurring at 0 relative wavenumbers.

observed and consistent with the presence of the occupied 4s orbital and the long vibronic progressions evident in both states of each ionic complex. The contour simulations additionally provide assignments of the total electronic angular momentum (Ω) of the states involved in the transitions. All simulations use a common Ω'' ($\Omega'' = 3$) while the excited states have both shown to be perpendicular transitions with the electronic angular momentum having increased in the A-state ($\Omega' = 4$) and decreased in the C-state ($\Omega' = 2$).

As a matter of convenience, the electronic symmetries of the A and C-states have already been introduced but not yet formally discussed. These determinations are based on the Ω assignments afforded by the rotational contour simulations and predictions from the d^7 electronic eigenfunctions. From Table 4-11 it is clear that only one molecular

Table 4-11. Properties of molecular states derived from certain d^7s^1 atomic terms.

d^7 s^1 Atomic State	Molecular State	d-hole population			Relative Xtal Field Energy (Dq)
		σ	π	δ	
d^7 (^{4}P) s	$^3\Pi$	2/5	1	8/5	-2.40
	$^3\Sigma$	1	8/5	2/5	4.80
d^7 (^{4}F) s	$^3\Delta$	0	2	1	-2.00
	$^3\Pi$	3/5	1	7/5	-0.75
	$^3\Sigma$	1	2/5	8/5	0.34
	$^3\Phi$	1	1	1	2.57

state can be derived from the d^7 (^{4}F) s^1 atomic term which is capable of supporting a symmetry with Ω = 4, namely the $^3\Phi_4$. This makes the symmetry assignment of the A-state unambiguous. The C-state symmetry assignment is less obvious as there are two molecular states ($^3\Delta_2$ and $^3\Pi_2$.) derived from the d^7 (^{4}F) s^1 which can support a symmetry with Ω = 2. These two possible assignments have been differentiated based on transition probabilities determined from the electronic d^7 wavefunctions. In the center of figure 4-17

the electronic wavefunction for the ground state of $CoAr^+$ is shown. Along the periphery of the figure the d-hole eigenfunctions of the d^7 (^{4}F) s^1 is shown along with the symmetry of the corresponding molecular states. Solid lines connecting the ground state with the various molecular states derived from the d^7 (^{4}F) s^1 indicate transitions to those states and

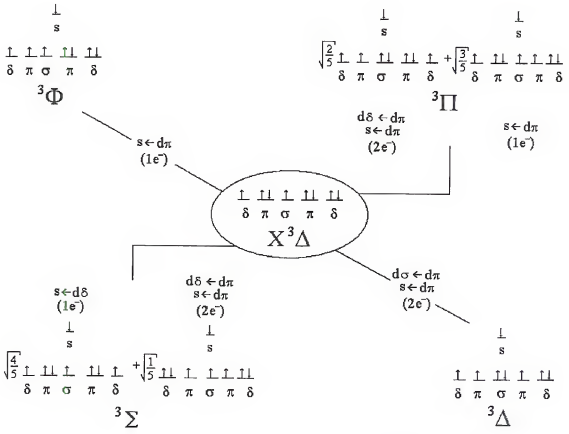

Figure 4-17. Qualitative transition probabilities between states connecting the ground with those derived from the d^7 (^{4}F) s^1 atomic term.

The ground state wavefunction (center) connects with the various molecular terms derived from the d^7 (^{4}F)s^1 atomic term. The transition probabilities can be inferred from the number of electrons that must be moved in order to arrive at the eigenfunction describing the molecular terms at the periphery.

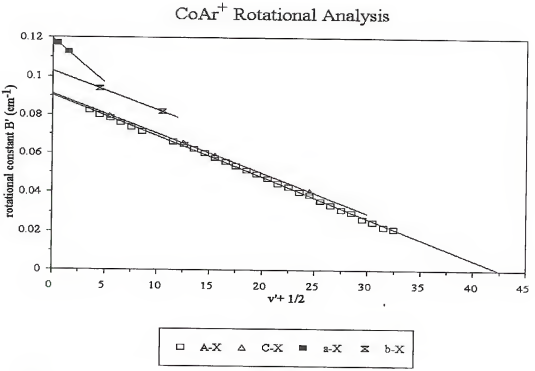

Figure 4-18. The upper state rotational constants of $CoAr^+$ plotted in accord with eqn. 4-11.

The lines are calculated from the fits of the observed data to eqn. 4-11 and the symbols represent the observed rotational constants. Note the striking similarities seen between transitions occurring in the A and C-states.

the annotation along the path describes the type of transition which occurs. For example, consider the $^3\Phi \leftarrow {}^3\Delta$ transition (center of fig. 4-17 to upper left corner). A single configuration describes the $^3\Phi$ electronic wavefunction and the transition which connects this state to the $^3\Delta$ involves the promotion of a single electron from the $d\pi$ orbital of the $^3\Delta$ to the 4s orbital of the $^3\Phi$. As this is a one electron transition, it is expected (and observed) to be intense. In fact, from fig. 4-17, it is predicted that only two electronic transitions with appreciable intensity are possible for the states derived from the d^7 (^{4}F) s^1

atomic term. These are the $^3\Phi$ which has a configuration described entirely by a $s \leftarrow d\pi$ promotion and the $^3\Pi$ which has 60 % of an electronic configuration described by a one electron $s \leftarrow d\pi$ transition from the ground state and thus assigns the C-state as the $^3\Pi_2$. The transition to the $^3\Delta$ requires the promotion of two electrons and is therefore expected to be of weak relative intensity and the promotion to the $^3\Sigma$ violates other selection rules.

The results of the $CoAr^+$ rotational analysis can be viewed in fig. 4-18 as the observed rotational constants have been plotted in accord with eqn. 4-11.

The b-X and D-X transitons

An intense, continuous progression of transitions is observed in the **D**-state of each molecule and approach diabatic dissociation in $CoAr^+$. The Leroy-Bernstein analysis (fig. 4-8) places the diabatic dissociation limit at 17 368 cm^{-1}. The difference between this limit and those of the $^3\Phi_4$ and $^3\Pi_2$ must be the same as the difference between the promotion energies between the atomic state which derives the **D**-state and those of the $^3F_4$ and $^3F_2$. These differences assign the **D**-state as derived from the $d^8\ ^3P_2$ term of Co^+. The binding energy of this state in each complex is consistently greater than the $^3\Phi_4$ and $^3\Pi_2$ states (Table 4-10). The effects of an occupied 4s orbital in the configuration of the atomic term deriving the molecular state are clearly reflected in the relative binding energies of these states. Moreover, the vibrational frequency (force constant) is greatest in the **D**-state and the normal correlation observed between bond force constant and bond energy is maintained.

Transitions in the **D**-state do not show the sharp, well-resolved rotational fine structure ubiquitous to the bands in the redder states but display rather poorly resolved rotational contours. This is presumably due to a shorter upper state unimolecular dissociation lifetime thus resulting in homogeneously broadened transitions. However broadened, application of the previously determined lower state constants ($B'' = 0.1245$ cm^{-1} and $\Omega'' = 3$) to the band contours of a number of transitions in the **D**-state of $CoAr^+$ has provided a consistent measure of the states total orbital angular momentum as $\Omega' = 2$. This assignment is entirely consistent with the wavefunctions of Table 4-3 and the expected properties of derived molecular states (Table 4-4). There is only one molecular state derived from the ^3P atomic term which is capable of supporting such an omega assignment. This is the $^3\Pi$ and thus the **D**-state is termed the $b\ ^3\Pi_2$.

The **b**-state demands special attention as it's interpretation is most subject to speculation. Intense, resonant **b-X** transitions occur in each of the $CoRG^+$, however, due to favorable Franck-Condon overlap, the data for $CoAr^+$ is most complete and the following discussion is reserved for $CoAr^+$. Originally [28] the **b**-state was considered two separate states. From the term value plot of fig. 4-5, it seems that the **b-X** transitions vanish at some point and then resume at higher frequency. The fragment at higher frequency clearly approaches the $^1D_2$ limit of Co^+ as is shown in fig. 4-5 and confirmed through the Leroy-Bernstein treatment (fig. 4-8). It should be noted that only the lower frequency transitions in the b-state (the 14 band origins to the red of the gap) were fit to the Morse equation (eqn. 3-1) and the solid line (which was calculated based on the constants extracted from this fit) extrapolates through the high frequency fragment and

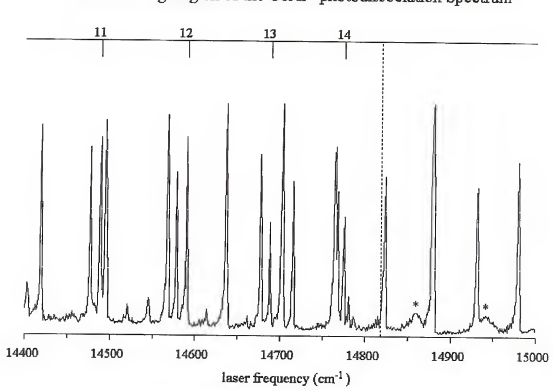

Figure 4-19. The region of the $CoAr^+$ photodissociation spectrum where b-X transitions apparently vanish.

Assigned transitions in the b-X system are labeled by upper state vibrational quantum number. The vertical dotted line labels the $^3F_3$ atomic limit at an energy offset by the ground binding energy (4111 cm^{-1}). Broad features occur above this limit and are labeled with asterisks.

approaches the $^1D_2$ limit in a fashion analogous to the systematic underestimation associated with the application of eqn. 3-1. It has been observed that the fragmentation of the **b**-state correlates with the presence of the $^3F_2$ and $^3F_4$ limits of Co^+ as seen in fig. 4-5.

Figure 4-19 shows the resonant photodissociation action spectrum for $CoAr^+$ in the region where transitions in the **b**-state apparently disappear. Labeled above the

spectrum are the upper state vibrational quantum numbers of the **b-X** transitions. The dotted vertical line shows the presence of the $^3F_3$ limit at an energy offset by the ground state binding energy. The intensity of transitions in the **b-X** progression does not follow the expected "Franck-Condon envelope" but apparently ends abruptly at $v' = 14$ just lower in energy to the $^3F_3$ limit. To higher energy of this limit and labeled by asterisks (fig. 4-19), a new broad feature appears at a frequency consistent with **b-X** transitions. This

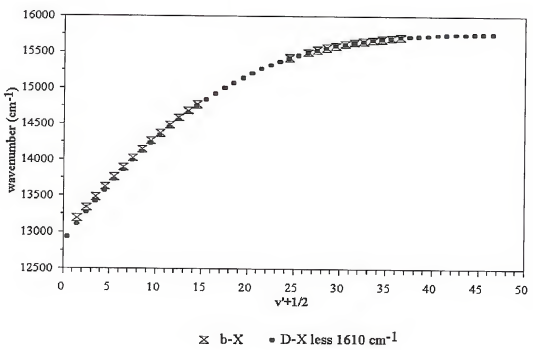

Figure 4-20. A comparison of the vibrational structure of the **b** and **D**-states.

The **b-X** transitions are plotted as they appear in fig. 4-5. The difference between the $^3P_2$ and $^1D_2$ Co^+ atomic term energies has been subtracted from the frequency of resonant transitions in the **D**-state and plotted as a function of vibrational quantum number.

new feature occurs only at frequencies between the ground state offset $^3F_2$ and $^3F_3$ limits of Co^+ (in the region where sharp **b-X** resonances have disappeared). The integrated intensities of these broad features and those of the sharp resonances are similar and it can be concluded that the resonant absorption profile of **b-X** transitions do not end at $v' = 14$, but rather the photodissociation dynamics change abruptly at $v' = 14$ and this change is presumably due to a very efficient coupling into the $^3F_3$ dissociation limit thereby considerably shortening the excited state lifetime and thus homogeneously broadening the resonant transitions. This dissociation pathway "turns off" above the $^3F_2$ limit and "normal" sharp resonances occur again as the **b-X** transitions approach the $3d^8\ ^1D_2$ Co^+ atomic limit.

From table 4-10, the vibrational structure of the **b**-state is consistent with the d^8 description of the Co^+ core. The vibrational frequency and binding energy is greater than that of the $^3\Phi_4$ and $^3\Pi_2$ (the d^7s states) and correspondingly similar to the **D**-state ($b\ ^3\Pi_2$). Moreover, a figure analogous to fig. 4-14 can be constructed for transitions in the **b** and **D**-states of $CoAr^+$. Fig. 4-20 shows the term value plot for **b-X** transitions and for **D-X** transitions whose frequencies have been lessened by the difference in promotion energies of the atomic states from which the molecular states were derived, i.e. $E(v')\ (cm^{-1})$ - 13261.1 cm^{-1} ($^3P_2$) + 11651.5 cm^{-1} ($^1D_2$). It is clear from fig. 4-20 and Table 4-10 that these two states which are derived from different atomic terms but the same d^8 Co^+ core share a very similar vibrational structure and other associated properties.

Two bands in the **b-X** system [the (10, 0) and (4,0)] exhibit sharp rotational structure and have been analyzed. Figure 4-21 shows the observed and simulated contour

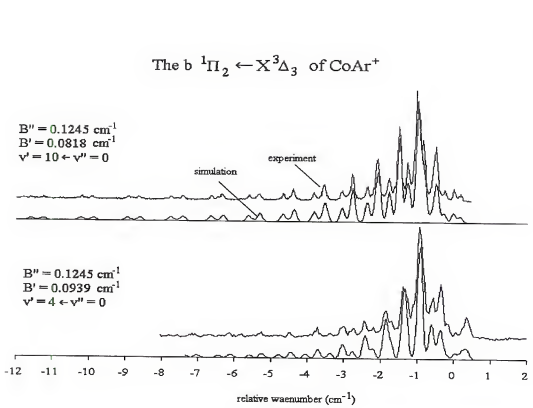
The b $^1\Pi_2 \leftarrow X^3\Delta_3$ of $CoAr^+$
B″ = 0.1245 cm^{-1}
B′ = 0.0818 cm^{-1}
v′ = 10 ← v″ = 0
simulation
experiment
B″ = 0.1245 cm^{-1}
B′ = 0.0939 cm^{-1}
v′ = 4 ← v″ = 0
-12 -11 -10 -9 -8 -7 -6 -5 -4 -3 -2 -1 0 1 2
relative waenumber (cm^{-1})

Figure 4-21. The simulated and observed rotational contour of two bands in the **b-X** system.

of both bands in analogous fashion to figs. 4-10, 4-12 and 4-15,16. The same lower state rotational constant (B″ = 0.1245 cm-1) and total orbital angular momentum (Ω″ = 3) was used in these fits as was used in the previous simulations. The upper state is consistent with a decrease in orbital angular momentum upon photon absorption and the contour was simulated using (ΔΩ = -1). The astute reader may, by now, have realized the development of an apparent inconsistency between the properties of the **a-X** and **b-X** systems. The rotational structure of bands in both systems are consistent with an Ω′ = 2 assignment and both states have been shown to derive from the same ^{1}D atomic term. From table 4-4 only one molecular state ($^1\Delta_2$) derived from the ^{1}D is capable of supporting an Ω = 2 assignment and this symmetry has been commissioned to the **a-X** system. To alleviate this

discrepancy, it is assumed that the **b-X** electronic transition undergoes a double change in total orbital angular momentum ($\Delta\Omega = -2$) and thus (tentatively) assigns the symmetry of the **b**-state as $^1\Pi_1$. The wavenumber transition frequencies associated with a ($\Delta\Omega = -1$) transition should be the same as a ($\Delta\Omega = -2$) transition, however with a different intensity distribution.

The triumph of the above model is the merging of the two fragment progressions in $CoAr^+$ into the **b**-state is now allowable. Without this merging, the fragment progression at the higher energy side of $^3F_2$ atomic limit (fig. 4-3) must be an extension of the two membered **a-X** progression and this is doubtful. Furthermore, the fragment progression (to the red of the $^3F_3$) must then be derived from a d^7s atomic configuration which is inconsistent with observed vibrational structure. Alternatively, this fragment could originate from a hot electronic band which connects with transitions in the **D**-state. The difference in energy between the fragment and the **D**-state would then be attributable to the spin-orbit splitting between the hot electronic state and the ground state. This alternative explanation is doubtful, the **b** and **D**-states are vibrationally very similar, but are rotationally rather different. Additionally, there will be extra transitions in the branch structure near the rotationless origin which are clearly not there (fig. 4-21).

In further support of the $^1\Pi_1$ **b**-state symmetry assignment, from the eigenfunctions of table 4-3, the majority of the configuration which describes the $^1\Pi$ would evolve from a 1 electron transition from the ground $^3\Delta$ state. Additionally, comparing the $^1\Pi_1$ and the $^1\Delta_2$, both derived from the ^1D term, it is expected that the $^1\Pi$ be less bound than the $^1\Delta$

owing to the greater dσ-orbital population as is observed. The greatest inconsistency of this model is the intensity of **b-X** transitions. Due to the rather forbidden nature of a $^1\Pi_1 \leftarrow {}^3\Delta_3$ transition (both spin and Ω forbidden) it is expected that the intensity of these transitions be much less than what is observed.

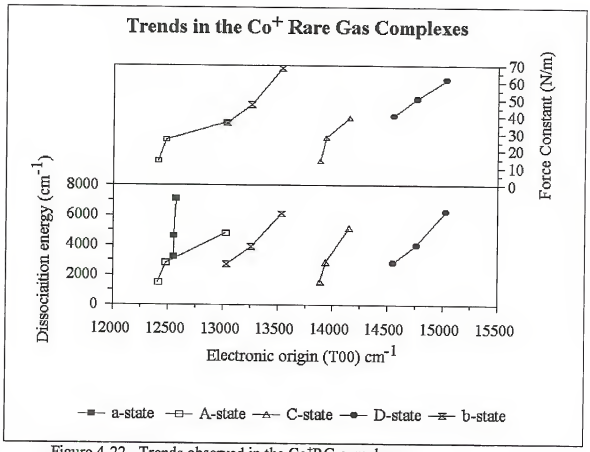

Figure 4-22. Trends observed in the Co^+RG complexes.

The top trace and right axis displays the correlation observed between the bond force constant and electronic origin. The lower trace and left axis shows the same correlation between dissociation energy and electronic origin. Solid lines connect the common state properties observed in each ionic complex.

Trends in the $CoRG^+$ complexes

Various physical properties have been accurately determined and the evolution of the various state properties as a function of bonding partner can be determined. This analysis can provide a means for the interpretation of molecular spectra where the data sets are less complete. In the photodissociation spectra of most molecules, the vibrational structure has been analyzed and the physical constants determined. These properties typically include the bond strength (dissociation energy), electronic origin, vibrational frequency (bond force constant), and anharmonicity. Figure 4-22 shows the correlation observed between three of the afore mentioned properties. The top trace and right axis of fig. 4-22 shows how the bond force constant of each $CoRG^+$ complex changes with electronic origin. The lower trace and left axis shows the same correlation observed with dissociation energy. In each case solid lines connect common states in each molecular ion. The exited state dissociation energy increases with increasing electronic origin [T(atomic resonance) {not shown} < T_0(Ar) < T_0(Kr) < T_0(Xe)] and indicates a ground state which is more strongly bound than the excited state, a prediction born out by measurement. The two traces of fig. 4-22 "track" and therefore a strong correlation exists between bond dissociation energy and force constant (fig. 4-23). This analysis suggests that force constants may be used in place of the measured dissociation energy to predict the relative binding energies of the upper and lower states.

Figure 4-23 shows the usual correlation between [48] bond force constant and dissociation energy. Interestingly, there seems to be a dependence on the presence of an

occupied s-orbital in the Co^+ chromophore deriving the molecular state. Both the **A** and **C**-states are derived from the d^7s^1 atomic configuration of Co^+ and the dependence between force constant and dissociation energy is noticeably different than that of the **b** and **D**-states which are built from the d^8 configuration of Co^+.

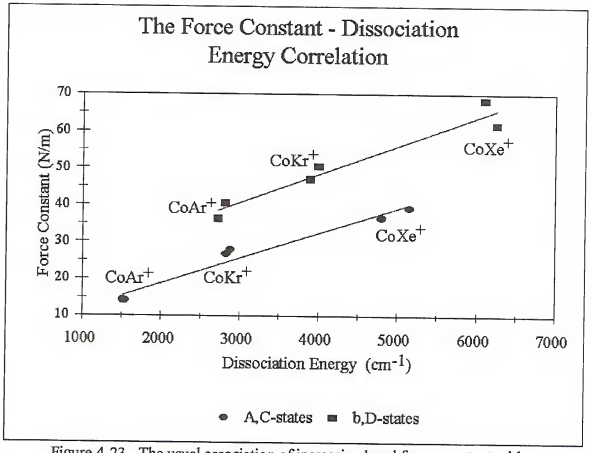

Figure 4-23. The usual association of increasing bond force constant with dissociation energy.

Two different correlations is evident as the association of force constant with dissociation energy seems dependent on the Co^+ atomic configuration which comprises the molecular state.

CoRG$^+$ summary

The $CoAr^+$ ground state binding energy has been accurately measured as 4111 cm^{-1} from the presence of four excited state dissociation limits observed in the resonant photodissociation spectrum of $CoAr^+$. High level ab intio theory [20] predicts the adiabatic binding energy at $D_0 = 0.406$ eV (3270 cm^{-1}) when corrected for the zero point level. Bauschlicher's calculations systematically underestimate the spectroscopic determined binding energies of this and other weakly bound (transition metal)$^+$ argides. Unfortunately, to date, the only state of any of the CoRG$^+$ ionic complexes to be tackled by calculation has been the ground state of $CoAr^+$. Bauschlicher's calculated ground state geometries and symmetries show much less deviation from experiment. The calculated ground state bond length of $CoAr^+$ is $r_0 = 2.45$ Å when approximately corrected for the zero point level and compares favorably (less then 3% error) with the measured value of $r_0 = 2.385$ Å. The calculated symmetry of the lowest lying state is $^3\Delta$ in complete agreement with the rotational analysis and the predictions based on the electronic eigenfunctions of the d-holes in a d^8 configuration (Tables 4-3 and 4-4).

The electronic eigenfunctions and properties derived from them have been most useful in the assignment of electronic transitions of $CoAr^+$. From comparisons of $CoAr^+$ with the isovalent CoF [47], these electronic eigenfunctions seem to provide some insight into the general notion of covalency. The bonding partners in both molecules are similar with a "lumpy" open d-shell Co^+ and a closed shell ligand (Ar or F^-). The transitions observed in both molecules (and therefore the electronic structure) are entirely similar as

both are derived from the same Co^+ chromophore. The difference between $CoAr^+$ and CoF is the bonding mechanism (electrostatic compared to covalent) and this difference manifests itself (among other ways) in the ordering of the molecular terms (Table 4-4) as derived from the same electronic eigenfunctions (Table 4-3). The ground state symmetry of CoF is $^3\Phi$ [47] which has a fully occupied $d\sigma$-orbital whereas the ground state of $CoAr^+$ has the minimal $d\sigma$-orbital occupation. During bond formation, the minimized structure of CoF is the one where the Co^+ offers the most electron density to the covalent (electron sharing) bond whereas in $CoAr^+$, the lowest energy structure is the one which minimizes electron density along the bond axes thereby deshielding the positive core of the Co^+ to allow maximal polarization of the electronic cloud of Ar.

CHAPTER 5
THE STRUCTURE OF Co^+OCO

We are interested in the association of transition-metal ions to various closed-shell, neutral ligands. The long-ranged ion induced-dipole forces present in charged complexes are significant when compared to covalent bond strengths, and thus represent a significant and crucial part of the modeling of condensed phase phenomena involving charged species. A binary ion complex, isolated in the gas-phase and at extremely low temperature, provides an elegant system for which to study the fundamental properties of intrinsically intermolecular forces. Free, isolated and cold, the complex may be studied experimentally under exactly the same conditions with which the molecule is calculated in a computer.

An ionic bond, like that pictured in a NaCl crystalline lattice, is, in the abstract limit, simply the electrostatic interaction between the closed-shell metal and halide ions that result from the complete charge transfer due to the disparity in the ionization potentials of the elemental atoms. The simplest molecule that contains an ionic bond would be something like the NaCl diatomic molecule. An isoelectronic analog of this molecule is $NaAr^+$, which, although '*chemically*' has the same electronic structure as NaCl, has a completely different picture *electrostatically*. The 'half-ionic' molecule M^+·RG still has nearly complete ionization of the metal center, but is bound by charge-

induced dipole forces, not charge-charge forces. This is concomitant with a drop in the binding energy from 4.23 eV for NaCl [49] to <0.2 eV for $NaAr^+$ [50,51]. We wish to study a 'half-ionic' bond in a binary complex, but where the charged metal center is not closed shell (i.e. is a transition metal). Moreover, the closed-shell ligand may be represented by a rare gas atom, or with more complex polyatomic ligands, with the proviso that the ligand ionization energy is still significantly higher than the metal.

Carbon dioxide is an excellent prototypical ligand for investigation because of its relatively rigid high symmetry structure and high ionization energy. Perhaps for this reason, isolated metal-carbon dioxide complex ions are currently the subject of active investigation, both experimentally [52-64] and theoretically [65-67]. The linear geometry [57-58, 60-63] of the $MgOCO^+$ molecule has been demonstrated by the overwhelming similarities between the measured optical photodissociation spectrum and that calculated [65,67] for a linear electrostatic structure. Similarity between observed and calculated properties suggests a linear structure [52, 59] for $FeOCO^+$ as well. More recently, Duncan has suggested the linear geometry of $CaOCO^+$ [53], at least in an excited state, from the presence of a spin-orbit splitting accounted for by Hund's case (a) coupling in a linear molecule. The structure of $VOCO^+$ is suggested to be non-linear [64] from the enhancement of insertion chemistry by excited state bending vibrations. The binding energy of $NiOCO^+$ has been spectroscopically determined [55], but not yet its geometry. The partially-resolved rotational contour of the photodissociation spectrum of $CoOCO^+$ has conclusively proven its linear structure in the ground state [56]. To date, no metal·CO_2 ion complex has suffered complete rotational analysis of its spectrum, nor any other experimental determination of its complete geometric structure.

In the current study we present the first *direct* measurement of the geometry of any transition metal cation bound to a CO_2 molecule in the gas-phase. Rotationally-resolved electronic transitions have been obtained *via* high-resolution photodissociation spectroscopy and these data are used to determine molecular constants of the $CoOCO^+$ complex in its ground and two excited electronic states.

Results

The transitions discussed here have all been previously observed in our laboratory [56]. The optical resolution with which the spectra were previously recorded was far inferior (nearly an order of magnitude) to the current study. Although several improvements to the instrument are responsible for the improvement in spectrum quality/resolution, careful control of dissociation laser power is probably the most important. The previously reported rotational constants are within 10% of the actual values, and the reported linear association of the Co^+ and CO_2 molecule is clearly correct. The original vibrational analysis [56] of the band systems of $CoOCO^+$ assumed the most general of vibrational indexing: one where $\Delta v = +1$. At that time the linear structure of $CoOCO^+$ was only speculation. Currently, the linear association of both ground and excited states has been verified and therefore the vibrational quantum numbering of the bending mode ($\Delta v_{bnd} = +2$) has been instituted in accord with selection rules. Even though the symmetry of the molecular cation in the excited **C** and **D**-states has not yet been confirmed, the vibrational quantum numbering assumes the above index (Table 5-1).

Table 5-1. Transition origins (cm^{-1}) of $CoOCO^+$

v_s	$v_r = 0$	$v_r = 2$	$v_r = 4$	$v_r = 6$
a-X ($^1\Delta_2$-$^3\Delta_3$)				
0	12301.06	12384.16		
A-X ($^3\Phi_4$-$^3\Delta_3$)				
0	12377.75	12449.18		
1	12566.14	12643.94		
2	12749.50	12832.71		
3	12928.06	13016.98	13114.05	13205.84
4	13102.40	13196.56	13297.78	
5	13271.63	13372.05	13476.59	13583.59
6	13436.40	13542.77	13650.88	13759.97
7	13597.52	13709.38	13821.02	13936.21
8	13754.52	13871.60	13987.41	
9	13907.64	14030.16		
10	14059.41	14182.56		
11	14197.47	14331.08	14462.52	14599.59
C-X ($^3\Pi_2$-$^3\Delta_3$)				
1	13930.99			
2	14123.72			
3	14310.99			
4	14493.16			
5	14669.70			
6	14841.51			

Table 5-1. Transition origins (cm^{-1}) of $CoOCO^+$ (continued)

D-X ($b\ ^3\Pi_2$-$^3\Delta_3$)				
1	15178.23	15274.69		
2	15379.39			
3	15572.35	15682.64		
4	15764.47	15880.57		
5	15954.53	16070.50	16184.62	
6	16142.59	16262.11	16379.74	16496.50
7	16326.41	16450.75	16571.60	16691.36
8	16506.46	16634.89	16759.77	
9	16682.88	16815.59	16942.50	
10	16856.18	16991.84		
11	17026.21			

This selection rule dealing with the observation of only even quantized bending vibrational levels in a linear polyatomic stems from the Franck-Condon factor or vibrational overlap integral. In the limit of slight vibronic coupling, it is realized that transitions between various vibrational levels in different electronic states can only occur

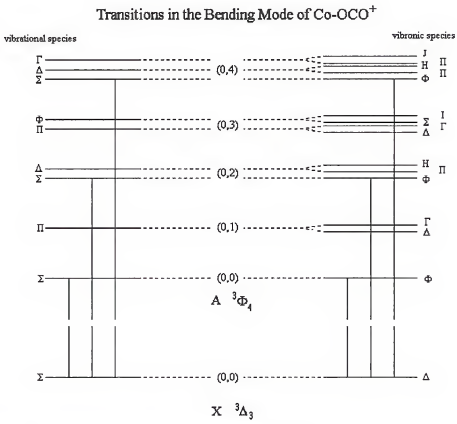

Figure 5-1. Possible electronic transitions in $CoOCO^+$.

Transitions are shown which originate in the symmetric vibrationless ground state and terminate on the various vibrational bending levels of the excited state. Only those bending excited states are shown which are built upon the lowest ($v' = 0$) level of the excited symmetric stretching mode. On the left of the figure, those transitions which are possible in the limit no vibronic coupling are shown and on the right, those for which a strong coupling is evident. Regardless of the degree of coupling, only every even quantized bending level is accessible.

when the integral $\langle \psi'_v | \psi''_v \rangle$ is non zero. This implies that a transition can only connect those levels with the same vibrational symmetry species as seen on the left of fig. 5-1. Figure 5-1 provides a qualitative representation of the transitions possible between the non-degenerate vibrationless level of the ground state ($\mathbf{X}\ ^3\Delta$) to the excited degenerate bending mode of the electronically excited ($\mathbf{A}\ ^3\Phi$) linear $CoOCO^+$ molecule. In the limit of strong vibronic coupling, this selection rule breaks down and transition intensities are governed by the more general selection rule $\langle \psi'_{ev} | \psi''_{ev} \rangle$, that is those transitions can occur when this product contains the species of the dipole moment ($\Phi - \Delta$ for the **A-X** of $CoOCO^+$) characterizing the electronic transition and is seen on the right of fig. 5-1. Of course this more general selection rule leads to the same transitions when the vibronic interaction is negligible. It is clear from fig. 5-1 that *regardless* of the degree of coupling between the vibrational and electronic wavefunctions of these states of $CoOCO^+$, the same transitions occur from the vibrationless level of the ground state and any differences resulting from degree of vibronic coupling will only manifest at vibrational excitation greater than $v_{bend} = 4$.

Figure 5-2 displays the red-visible photodissociation spectrum of $CoOCO^+$. The veticle axis provides photo-current resulting from photo-distruction via the following

$$Co^{+\bullet}OCO + h\nu \rightarrow Co^+ + OCO$$

which is the only pathway to dissociation observed. The horizontal axis gives the dissociation laser frequency. The tick marks above the spectrum label the resonant transitions and provide the excited state vibrational quantum numbers. The vibrational

constants of Table 5-2 were abstracted from a fit to the following formula detailing an anharmonic oscillator of more than one degree of freedom:

$$\nu = T_{00} + \omega_s v_s + \omega_r v_b + \omega_{ss} v_s^2 + \omega_{rr} v_b^2 + \omega_{sr} v_s v_b$$

Of the 3N - 5 = 7 normal modes possible, only 3 are observed and all originate from the Co^+-OCO complex bond: The symmetric metal-ligand stretch and the degenerate bending motion. The remaining four motions are intrinsic to the CO_2 ligand and are not observed.

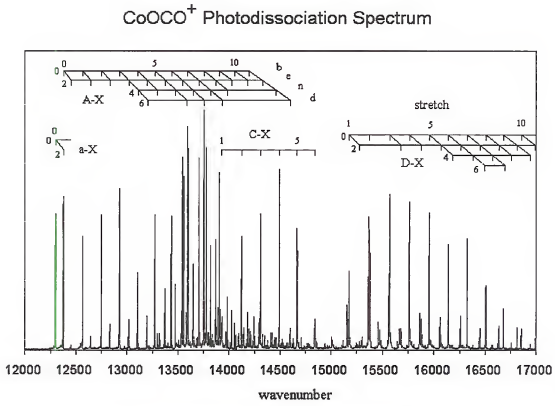

Figure 5-2. The photodissociation spectrum of $CoOCO^+$.

Vibrational progressions in the complex stretching and bending modes have been identified in 4 electronic states and are labeled by quantum number. Note that the transitions active in the complex bending mode occur only for even vibrational quantum number as in accord with selection rules.

There are only two bands observed in the $\mathbf{a}^1\Delta_2 \leftarrow \mathbf{X}^3\Delta_3$ system of $CoOCO^+$. Table 5-1 gives the frequencies of the bands of this (and other) electronic transitions. The polyatomic vibrational structure of this complex is labeled by the two active vibrational

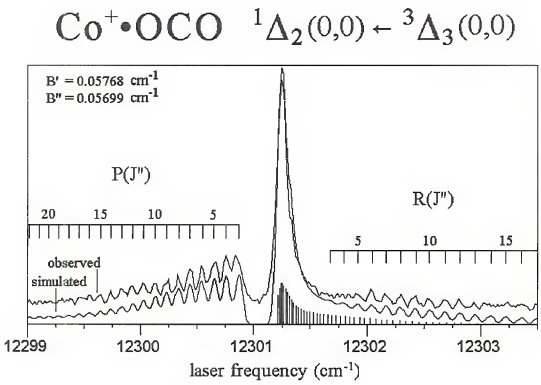

Figure 5-3. Observed (top trace) and simulated (bottom trace) contour of the **a-X** (0,0).

The simulation was generated assuming that $CoOCO^+$ acts as a rigid symmetric rotor undergoing a perpendicular transition ($\Omega' = 2 \leftarrow \Omega'' = 3$). The tick marks above the spectrum indicate the resonant transitions within the P and R-branches and are labeled by the lower state rotational quantum number (J"). The unresolved transitions in the Q-branch can be seen as the line spectrum beneath the simulated contour and trailing out to higher energy. The **a-X** (0,0) is consistent with a $^1\Delta_2 \leftarrow {}^3\Delta_3$ symmetry description.

modes of the complex , the stretch and bend of the ligand and metal ion. Thus the origin of the system is termed the **a**(0,0)-**X**(0,0), where the notation (v_{stch}, v_{bnd}) indicates the complex stretching and bending motions repectively. One other transition is observed in this system and has been assigned as the **a**(0,2)-**X**(0,0) but is too weak for full rotational analysis.

Figure 5-3 shows the **a**(0,0)-**X**(0,0) origin band in detail. The verticle axis is relative Co^+ photocurrent and the horizontal axis is the dissociation laser frequency, but for the purposes of this discussion the figure shows the absorption spectrum of the ion at laser linewidth limited resolution. Certain qualitative observations of the rotational structure of the **a**(0,0)-**X**(0,0) can be made which facilitates assignment. The most basic of observations to be gathered from fig. 5-3 is that $CoOCO^+$ is a linear ($C_{\infty v}$ symmetry) complex in both the ground and excited states because of the 'diatomic-like' band structure of the system. The spacing between members of the P and R branches are nearly equal which indicates little change in geometry (rotational constant) upon excitation. This is also consistent with the diagonal Franck-Condon factors observed in the $a^1\Delta_2 \leftarrow X^3\Delta_3$ system. Additionally, the greater intensity of the P-branch relative to the R-branch implies a decrease in orbital angular momentum upon electronic excitation. The gap (~0.4 cm^{-1}) between the intense, unresolved Q-branch and the first rotational transition in the P-branch ($J' = 2 \leftarrow J'' = 3$) indicates large unquenched orbital angular momentum in the ground state. Finally, the slight blue-degraded nature of the Q-branch clearly indicates $r_0' < r_0''$ ($B_0' > B_0''$).

A simulation was generated which quantifies the qualitative observations above and is also shown in Figure 5-3 (bottom trace). The tick marks above the spectrum indicate resonant transitions in the P and R-branches and are labeled by J". The line spectrum of the Q-branch is provided and shows its unresolved, blue-degraded nature. The simulation was generated assuming that $CoOCO^+$ acts as a symmetric rigid rotor undergoing a perpendicular transition ($\Omega' = 2 \leftarrow \Omega'' = 3$). The rotational constants extracted from the fit are B" = 0.05699 cm^{-1} and B' = 0.05768 cm^{-1}. The contour of fig.

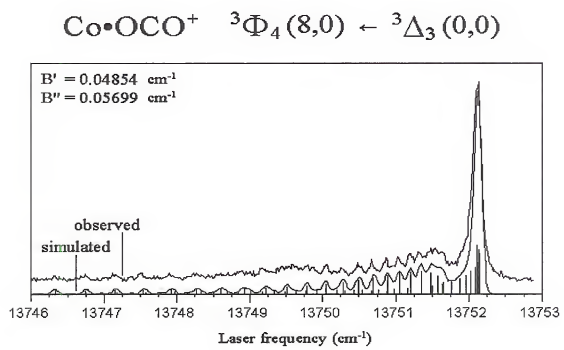

Figure 5-4. Observed (top trace) and simulated (bottom trace) contour of the A-X (8,0).

The line spectrum of the P, Q, and R-branches which give rise to the calculated contour are provided beneath the simulation. The intense feature seen ~ 13752 cm^{-1} results from transitions in the R-branch turning over and forming a head.

5-3 was generated with a rotational distribution not described by a single Boltzmann but a composite of 94% (4.6K) ions and 6% (37K) ions. The simulated contour assumes a linewidth of ~0.05 cm^{-1} and clearly reproduces the observed rotational structure of the **a**(0,0)-**X**(0,0).

Three transitions in the Co^{+}↔OCO stretching progression of the $A^3\Phi_4 \leftarrow X^3\Delta_3$ system were rotationally resolvable and simulated as symmetric rigid rotors. Figure 5-4 shows the rotational structure of one of the bands in this system, the **A**(8,0)-**X**(0,0). The **A**(0,0)-**X**(0,0) and **A**(6,0)-**X**(0,0) have also been simulated but are not shown here. All band simulations require the same lower rotational constant of B" = 0.05699 cm^{-1} and the same rotational temperatures as in fig. 6-3. The $A^3\Phi_4 \leftarrow X^3\Delta_3$ system requires a slightly larger linewidth (~0.06 cm^{-1}) than the $a^1D_2 \leftarrow X^3\Delta_3$ system for proper simulation, indicating a more rapidly predissociation upper state. The constants derived for the $A^3\Phi_4$ state are given in Table5-2. All three bands were simulated as perpendicular transitions with the total orbital angular momentum increasing upon photo-excitation ($\Omega' = 4 \leftarrow \Omega'' = 3$).

The rotational constants derived from our analysis of the photodissociation spectrum of Co^{+}·OCO are listed in Table5-2. The linear dependence of the A-state rotational constants on ($v' + \frac{1}{2}$) allow the determination of the the vibration-rotation coupling constant ($\alpha_e' = 0.00047$ cm^{-1}) and equilibrium rotational constant ($B_e' = 0.05243$ cm^{-1}) for that state.

Table 5-2. Spectroscopic constants of $CoOCO^+$ [cm^{-1}]

	$X\ ^3\Delta_3$	$a\ ^1\Delta_2$	$A\ ^3\Phi_4$	$C\ ^3\Pi_2$	$D\ ^3\Pi_2$
T_{00}	0	12301	12377	13733	14975
ω_{strch}			190.1	200.5	204.5
ω_{bnd}		41.6	37.0		48.2
x_{ss}			-2.22	-2.63	-1.64
x_{bb}			0.33		-0.26
x_{sb}			2.50		2.02
B_0	0.05699	0.05768	0.05222		
α_e			4.7×10^{-4}		

The A-state is derived from a parity forbidden transition centered on the Co^+ which involves a change from $3d^8$ in the ground state to $3d^74s$ in the excited state. The presence of the occupied 4s orbital in the excited state increases repulsions between the metal ion and the CO_2 molecule and thus leads to the longer bond length (Table 5-2) than for d^8 coniguration states. The vibrational progressions of the **A-X** system place a lower limit on the **A**-state dissociation energy of 4100 cm^{-1}. Assuming the same underestimation (~10%) quantified during the Co^+-rare gas studies, this places the **A**-state dissociation energy at 4500 cm^{-1}. This dissociaton is into fragments (Co^+ d^7s ($^3F_4$) + CO_2 $^1\Sigma_g^+$) that are 16877 cm^{-1} above the product ground states. Subtraction of the Co^+ d^7s ($^3F_4$) promotion energy above the ground state Co^+ d^8 ($^3F_4$) places the ground state bond strength of the $CoOCO^+$ complex at 7100 cm^{-1}. The **a-X** transition of $CoOCO^+$ is derived from a $3d^8$ ($^1D_2$) ← $3d^8$ ($^3F_4$) spin flip of the Co^+. Only nominal changes in geometry and short vibrational progressions are expected (and observed) for this state.

Using the ground state bond strength and the atomic promotion energy of the $3d^8$ ($^1D_2$) above the ground state $3d^8$ ($^3F_4$) of Co^+, a dissociation energy of the **a**-state of 6450 cm^{-1} is obtained. Only approximate measures have been utilized in the determination of these dissociation energies, therefore, an error of ±20% is assigned.

Discussion

The title molecular ion may be considered a 'cluster' in the sense that it is conceptually separable into two parts, and these parts are bound by forces that are normally thought of as intermolecular. The electronic structure of the ion is considered to be derived from an open d-shell atomic configuration (M^+) and a polarized 'neutral' ligand, just like many coordination compounds in inorganic chemistry. Little electron delocalization over these two conceptual parts of the molecule is expected or observed. The electronic transitions observed derive from parity forbidden transitions at the metal center which may or may not involve a formal electronic configuration change. In this, like many other ion complexes studied by us, the states derived from d^8 (d^n) metal configurations (**X**, **a**, others) are more strongly bound than those derived from $3d^74s$ ($d^{n-1}s$) configuration (**A**, **C**, others) because of the increased repulsion of the 4s orbital of the metal ion with the closed shell ligand. The ordering of the electronic states within a configuration is such that the states which have more 'd-hole' occupation at the bonding axis (greatest dσ hole population) lie lowest in energy. The ground state of the complex,

which derives from a d^8 ^3F Co^+ atomic state should then be pure ($\sigma^+\delta^+$) hole state, $^3\Delta$, as observed experimentally in this work.

Bauschlicher *et al* [66] have calculated the properties of the linear $CoOCO^+$ complex with a high level ab initio method, involving a multi reference configuration interaction algorithm. They too predict a $^3\Delta$ ground state with a dissociation energy D_e = 7450 cm^{-1} and zero point corrected bond energy D_0 of 7312 cm^{-1}. Our rotational analysis of this molecule (Figures 3,4) shows a $^3\Delta_3$ ground state in complete analogy to the ground states of the $CoAr^+$ and $CoKr^+$ complexes [28, 29] and confirms Bauschlicher's calculation. Our spectrum provides only a poor lower limit to the dissociation energy of the ground state of the ion from the vibrational structure of the **A-X** and **D-X** systems of >7000 cm^{-1}, consistent with this calculation. The experimental value should be considered inferior at this time to the calculated value as an accurate spectroscopic determination of an excited state dissociation limit (as was performed in the case of $CoAr^+$ and $CoKr^+$) has yet to be made.

Bauschlicher's calculations [66] predict a geometry for the Co^+-O'CO molecule with a rotational constant of B_e'' = 0.05693 cm^{-1}. Correcting for zero point distortion of the ground state (approximately), a predicted B_0'' is 0.05673 cm^{-1} and may be compared with experiment with an amazing 1% error. Bravo! The results further indicate that the CO_2 molecule geometrically distorts asymmetrically in the field of a Co^+. i.e., $R_{Co\text{-}C}$ = 3.176 Å, $R_{O'C}$ = 1.184 Å, and R_{CO} = 1.154 Å. Unfortunately, with one rotational constant derived from the linear-linear electronic transition analyzed in this study, we are unable to confirm the extent of the CO_2 geometric distortion.

Based on the accuracy with which Bauschlicher has calculated the bond lengths of various electrostatic species [20, 27] and the similarity seen between the calculated and observed rotational constants of this study, we must assume that theory is right and the CO_2 molecule does significantly geometrically distort in the field of a Co^+. Nonetheless, if the ligand is assumed undistorted in the complex relative to its gas-phase symmetric geometry [35], our experimental rotational constant places the Co^+-C distance at 3.167 Å. So, with uncertainty due to the unknown extent of ligand distortion in the electric field of the ion, the ground state center-to-center metal-ligand distance of this complex is in the range 3.17 ± 0.01 Å.

CHAPTER 6
THE STRUCTURE OF Co^+N_2

There are many goals of the modern spectroscopist yet none as fundamental as determining the structure of a molecule. The structure-property relationship which exists in matter is of central importance to all applications of chemistry and to this end X-ray crystalograhic and NMR techniques have been utilized to ascertain the structure of molecules in both the solid and liquid phases. While working in the gas phase, although several methods have been employed to determine the molecular structure none are as powerful as the direct observation of rotational structure via some laser induced phenomena.

The geometry of the ground state of CoN_2^+ has been determined as T-shaped through the direct measurement of the rotational band contour of a low lying electronic excited state and through comparisons of the structure of this transition with the well understood and documented $a^1\Delta_2 \leftarrow X\,^3\Delta_3$ transition present in Co^+(Ar, Kr, Xe, CO_2) [28, 29, 6]. This measurement has ushered in a host of controversy from both the experimental community [37] and theoreticians [36- 38] as no one can reproduce or calculate this result. The experimentalist (Heinemann, Schwarz, and Schwarz who shall be referred to as HSS) [37] has reported the ground state geometry of CoN_2^+ but **never** actually measured the geometry of this complex. Instead they measured the Co^+-N_2 metal-ligand

scission energy (23.0 ± 1.7 kcal/mol) through ligand exchange reactions in an FT-ICR cell. *Ab initio* quantum mechanical calculations were then performed on the various geometries expected for the CoN_2^+ molecule and HSS determined that these calculated results expressed a preference for the linear association of N_2 to Co^+, in fact, the calculated dissociation energy for a linear complex (D_e(linear) = 23.4 kcal/mol, D_e (T-shaped) = 8.9 kcal/mol) agreed with their experimentally determined value. As their calculated results reproduced Bauschlicher's [36] earlier determination and their measurement of the dissociation energy agreed with calculation (linear symmetry), HSS's assumed the linear geometry of CoN_2^+ and reported as such [37].

A few comments need to made of HSS's treatment and conclusions. The determination of the binding energy through measurement of ligand exchange rate constants in a FT-ICR cell is an inherently low resolution measurement. As the ions in HSS's study are only collisionally cooled, the experiments initial conditions are difficult to establish and are likely to contain an ensemble of electronically and vibrationally hot states. Additionally, the conversion of rate constants to the Gibb's free energy through the use of conventional thermodynamic relationships is speculated since the system may not be in equillibrium. Furthermore, as shown previously, ab inito calculations cannot accurately predict the bond energies of simple binary transition metal - rare gas complexes. In ab initio theory, there exists a 15 - 20% systematic underestimation of the dissociation energy of all transition metal - rare gas binary ions measured to a worthy precision.

All the known calculations of CoN_2^+ [36-38] are in agreement in that each predict a linear ($C_{\infty v}$) ground state with the association mainly determined by the electrostatic

(charge-quadrupole) and inductive forces (charge-induced dipole) present. Not only are these calculations in disagreement with our findings presented here, but the theory predicts the side-on coordination to be a saddle point in their potential energy determinations, thus making the theory clearly deficient.

Below we present experimental evidence for the nonlinear association of N_2 to Co^+. Unfortunately, the band contour of the observed transition is not sufficiently resolved to provide an accurate simulation. The limited resolution of this band is due to the laser linewidth and unresolved nature of an asymmetric rotor with heavy nuclei displaced from the symmetry axis.

Results

The resonant photodissociation spectrum of CoN_2^+ has been observed before [68] and is reproduced in figure 6-1 along with the similar molecule $CoXe^+$. The origin (0,0) of **a-X** system, starred in fig.6-1, has been observed in each of the binary Co^+-rare gas complexes and in the polyatomic Co^+OCO and characterized as the $a^1\Delta_2 \leftarrow X^3\Delta_3$ (0,0). This transition connects two states which are derived from d^8 Co^+ atomic states ($X\ ^3F$ and $a\ ^1D$) with the main difference due to different electronic spin coupling and spatial orientation of the occupied d-orbitals. The isolation of the starred transition in CoN_2^+ is very reminiscent of that observed in $CoXe^+$ and the diagonal Franck-Condon factors accompanying this transition is observed in all the Co^+-ligand complexes. These similarities assure that the starred transition of CoN_2^+ is due to the this same d^8-d^8

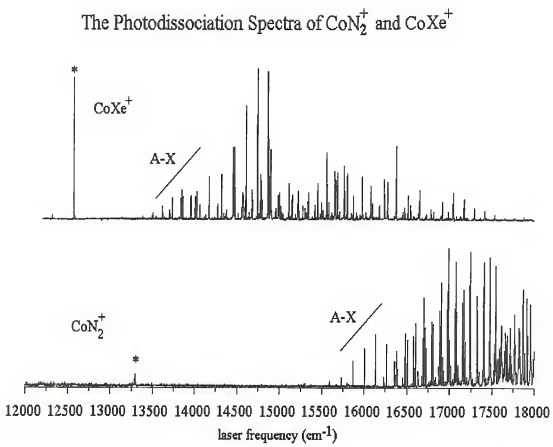

Figure 6-1. A comparison of the photodissociation spectra for $CoXe^+$ and CoN_2^+. The starred transitions indicate the origins of the **a-X** system in each.

transition centered on the Co^+ chromophore. The lack of intensity of this transition in CoN_2^+ is not reminiscent of those observed in the other Co^+-ligand complexes.

The starred transition of fig. 6-1 was scanned slowly so as to improve the resolution with which it was acquired and is shown as the top trace of fig. 6-2. The similar d^8-d^8 transitions (**a-X** origins) of the $CoOCO^+$, $CoKr^+$, and $CoAr^+$ have been reproduced in fig. 6-2 in order to show the differences in rotational structure between

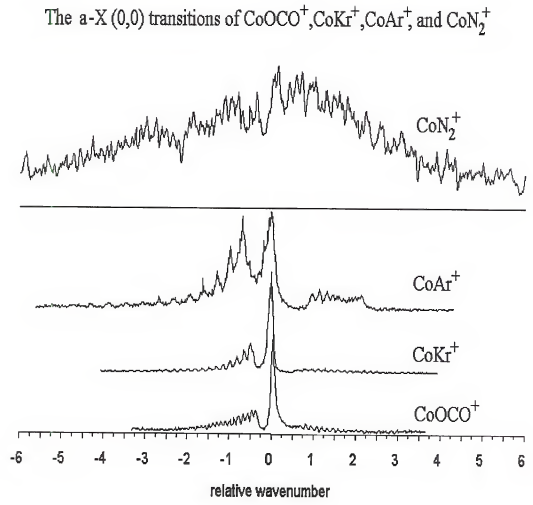

Figure 6-2. The origin of the **a-X** system in the various Co^+-homologs.

Each trace has been offset by the rotationless band origin. Clearly the **a-X** system of CoN_2^+ lacks the simple "diatomic like" rotational structure ubiquitous to the three lower traces

these bands. Each band has been plotted versus the frequency offset from the rotationless band origin (Table 6-1). All spectra were acquired in analogous fashion using the same scan rates, comparable dye laser power, comparable single to noise ratio, etc. but the resolution of the top trace is clearly inferior.

Table 6-1. The band origins of the **a-X** systems

	Rotationless band origin (cm^{-1})
$CoOCO^+$	12301
$CoXe^+$	12575
$CoKr^+$	12553
$CoAr^+$	12552
CoN_2^+	13299

Characteristic of the $a^1\Delta_2 \leftarrow X^3\Delta_3$ is the presence of discernible "gaps" between the unresolved Q-branch and the first members of the P and R-branches and indicative of a large unquenched electronic angular momentum present in the lower state. Also characteristic is the similarity in geometry (bond length) observed between the two states connected by this transition as is apparent by the near equal spacing between the members of the P and R-branches. The top trace of fig. 6-2 does not show any of these characteristics and is due to the presence of heavy nuclei displaced from the symmetry axis thus quenching the electron orbital angular momentum. Additionally, the overall width of the top band is unique and the uncharacteristic lack of intensity is (at least partially) due to the distribution over spaced-out unresolved K-structure (as opposed to unresolved J-structure). Several additional mechanisms are possible which allows this degraded resolution and will be suggested but the only one of any merit is that the top trace of fig. 6-2 results from the band contour of an asymmetric rotor.

A possible explanation for the poor resolution of this band of CoN_2^+ may be due to a shorter excited state lifetime relative to the other transitions depicted in fig. 6-2, thus resulting in a homogeneously broadened spectrum. However, as all the transitions of fig.

6-2 are centered on the same ^1D d^8 ← ^3F d^8 spin forbidden Co^+ absorption, a sudden change in the excited state dynamics is not plausible. Additionally, perhaps the resolution is limited by laser linewidth? This is obviously true, but if the rotational structure of $CoOCO^+$ (lowest trace of fig. 6-2) was resolvable then that for a linear CoN_2^+ should also be resolved as the center to center bond length should be shorter in CoN_2^+ and the ligand mass clearly lighter (both lead to a larger rotational constant). In fact, given the mass and anticipated bond length for a linear CoN_2^+, it should have a $\mathbf{a}^1\Delta_2 \leftarrow \mathbf{X}^3\Delta_3$ (0,0) band contour similar to that observed for $CoAr^+$ with minimally the "gap" structure discernible.

An explanation of the observed transition of CoN_2^+ resulting from a electronically hot band is always a consideration. However, frequency scans 1000 cm^{-1} to the red of the **a-X** (0,0) did not result in any resonant transitions. Additionally, transitions resulting from hot electronic bands have never before been identified in our photodissociation spectra and is a tribute to the supersonic expansion the ions suffer prior to photo-interrogation.

The only acceptable explanation for the lack the of simple rotational structure typical of the $\mathbf{a}^1\Delta_2 \leftarrow \mathbf{X}\ ^3\Delta_3$ systems is that CoN_2^+ possesses a T-shaped (C_{2v}) symmetry in at least one of the states involved in the transition. Given the similarities observed between the ground and this excited state in the Co^+-rare gases (and in Co^+OCO) and that both states derive from d^8 atomic states, it is probable that the symmetry of both the **a**-state and ground state of CoN_2^+ are non-linear (C_{2v}).

Additional arguments [68] supporting the non-linear geometry of the ground state are the enhanced Franck-Condon overlap with the bending mode of the proposed linear excited **A-X** electronic system of CoN_2^+. The first members of the "blue" states of CoN_2^+

(fig. 6-1) result from **A-X** transitions which terminate on the excited bending mode of the linear complex. Unlike the $A^3\Phi_4 \leftarrow X^3\Delta_3$ (linear-linear) transition of $CoOCO^+$ described previously, the most intense absorptions of CoN_2^+ evident in fig 6-1 result from transitions which connect the ground state to the bending vibrational levels of the A-state, thus indicating a gross geometry change upon photon absorption.

Discussion

Why should the ground and at least one of the excited states of CoN_2^+ be non-linear while those of $CoOCO^+$ are clearly linear? All theoretical calculations [36-38] predict a linear ground state and simple electrostatic calculations indicate the most stable configuration is linear for all bond lengths. Of all the Co^+- homologs, CoN_2^+ is not only unique rotationally but is unique in all aspects of its electronic structure. Looking back at fig. 6-1, not only is the first spin-forbidden electronic transition (the **a-X** system) blue shifted from that observed in $CoXe^+$ but also is the first spin-allowed electronic system (labeled **A-X**). Based on the simple electrostatic arguments established in chapter 4, both origins of these band systems in CoN_2^+ should be on the low energy side of those observed in $CoXe^+$, moreover, given the relatively small N_2 quadrupole moment and dipole polarizability (α_1) which is just smaller than Kr (Table 4-2), these electronic transitions should be in the same spectral region as those observed for $CoKr^+$. In stead the origins of the **a-X** and **A-X** systems of CoN_2^+ are 1000 and 3000 cm^{-1} (Table 4-10) to the blue of the electronic origins of those analogous states in the other Co^+-homologs, thus implying

that the ground state of CoN_2^+ is bound *more strongly* than any of the Co^+-homologs!

Re-posing our opening question and adding to it: Why is the ground state geometry of CoN_2^+ T-shaped and why is it more strongly bound than the other Co^+-ligand species? As electrostatics fails in describing the bonding which occurs, perhaps the T-shaped geometry indicates that the cobalt atomic ion is inserting (but not inserted) into the triple bond of N_2 and thus this interaction could be described by at least a partial degree of covalency. This covalent interaction is short ranged and thus provides a reason for the presence of non-linear states derived from Co^+ atomic states with d^8 electronic configurations and the presence of linear states which are derived from the radially larger Co^+ d^7s atomic states. If the ground state is becoming covalent, then the description of this state of the complex as derived from a d^8 ^3F Co^+ atomic state composed of a pure $\sigma^+\delta^+$ hole state may no longer be applicable and may be the reason for the uncharacteristic intensity of the origin of the **a-X** system of CoN_2^+.

CoN_2^+ Conclusions

Arguments have been proposed indicating a T-shaped ground electronic state (C_{2v} symmetry) whose bonding mechanism may be described by a partially inserted covalent interaction. This system may pose interest as a monumental step along some reaction coordinate in the activation of N_2.

CHAPTER 7
THE SOLVATION OF ZrO^+

The first part of this dissertation has focused on the elucidation of chemical forces between transition metal ions and a neutral closed shell ligand. When these interacting particles were both atoms, this became the simplest possible system which still bore resemblances to the aqueous phase and the solute-solvent bonding forces were determined with spectroscopic detail. In this current study, the chromophore for optical transitions is a diatomic metal oxide ion. The associations of the solvent ligands (CO_2, N_2, CO, and Ar) to the diatomic solute ZrO^+ are determined through photodissociation spectroscopy and the nature of the elucidated forces present have indicated different geometric configurations of the complex ions.

Results

The results of the spectral analysis of the $^{90}ZrO^+$ solute solvated by four different closed-shell ligands is presented in Table 1. The resonant vibrational structure of each molecule was fit to an anharmonic oscillator (eqn. 7-1) detailing more than one degree of freedom.

$$\nu\,(v'_{ZrO}, v'_{Sstr}, v'_{Astr}, v'_{bnd}) = T + \omega'_{ZrO}\,(v'+\tfrac{1}{2}) + \omega'_{Sstr}\,(v'+\tfrac{1}{2}) + \omega'_{Astr}\,(v'+\tfrac{1}{2}) + \omega'_{bnd}\,(v'+\tfrac{1}{2}) - x'_{ZrO}\,(v'+\tfrac{1}{2})^2 - x'_{Sstr}\,(v'+\tfrac{1}{2})^2 - x'_{Astr}\,(v'+\tfrac{1}{2})^2 - x'_{bnd}\,(v'+\tfrac{1}{2})^2 \qquad (7\text{-}1)$$

Table 7-1. Spectroscopic constants for the $^{90}ZrO^{+}\bullet$ ligand species (cm^{-1})

	$^{90}ZrO^{+}\bullet OCO$	$^{90}ZrO^{+}\bullet Ar$	$^{90}ZrO^{+}\bullet N_2$	$^{90}ZrO^{+}\bullet CO$
T	14352 ± 3	14904 ± 3	14887 ± 5	15174 ± 5
T_{00}	14892 ± 3	15459 ± 3	15598 ± 5	15919 ± 5
$\Delta G_{1/2}$	884.5 ± 0.1	892.8 ± 0.1	891.9 ± 0.2	900 ± 1
ω'_{ZrO}	890.7 ± 0.3	900.0 ± 0.5	898.4 ± 0.9	-
ω'_{Sstr}	172.9 ± 0.3	169.7 ± 0.7	243.3 ± 0.5	311 ± 1
ω'_{Astr}	-	-	224.3 ± 0.8	227 ± 1
ω'_{bnd}	19.4 ± 0.1	43.0 ± 0.3	62.5 ± 0.4	56.7 ± 0.3
x'_{ZrO}	3.4 ±0.08	3.5 ± .1	3.2 ± 0.3	-
x'_{Sstr}	0.63 ± 0.09	0.9 ± 0.3	1.9 ± .1	6.4 ± 0.3
x'_{Astr}	-	-	8.4 ± 0.2	2.2 ± 0.3
x'_{bnd}	-0.06 ± 0.02	-0.22 ± .06	-0.42 ± 0.06	0.03 ± 0.03
k'_{Sstr} (N/m)	54.8 ± 0.1	49.2 ± 0.2	77.3 ± 0.2	126 ± 0.4
Sourse (.wq1)	OCO-ISO	AR-ISO	NN-ISO	CO-ISO

To describe the structure of each molecule only 3 (4) upper state quantum numbers and their squares were used and this assignment is in terms of the Zr^{+}-O solute symmetric stretch (v_{ZrO}) with the remaining quantum numbers associated with motion along the solute-solvent bond axis. Vibrational modes intrinsic only to the solvent are not observed. The electronic term energy, T of eqn 7-1, is the difference in energy between the zero point of the ground electronic state and the bottom of the excited state potential plus the zero point energy of the solvent.

ZrO^+Ar and ZrO^+OCO

The photodissociation spectra of ZrO^+Ar and ZrO^+OCO are rather similar (fig.7-1) and therefore presented together. The x-axis represents laser frequency and for $^{90}ZrOAr^+$ this has been shifted to lower energy (-567 cm^{-1}) by the difference in term energies (T_{00}) between the two molecules. The vertical axis depicts relative dissociation into ZrO^+ fragments which is the only light induced product observed at these photon energies. The substructure evident in both spectra repeats at a nearly constant interval and is due to a progression in the ZrO^+ diatomic stretch. Even at the scale of fig. 7-1, it is evident that the diatomic stretching frequency of the ZrO^+ solute is dependent upon the solvent bond partner. Within each "unit" of substructure, vibrational progressions have been characterized in two lower frequency modes assigned as 0 to 3 quanta of $ZrO^+ \leftrightarrow$ (solvent) complex stretch combined with 0 to 6 quanta of $ZrO^+ \measuredangle$ (solvent) complex linear angle bend. Only even quantum numbers have been assigned to the degenerate complex bending vibrational levels in accord with selection rules governing transitions between states of high geometric symmetry (see below). These assigned band positions are presented in Table 7-2.

The relatively intense features of fig. 7-1 are cold band absorptions with a hint of hot bands evident in the bending vibrational progressions. Among the subtle differences between the vibronic transitions observed in these two molecules is the presence of a second electronic state in ZrO^+Ar which is not reproduced in the known absorption spectrum of ZrO^+OCO (or any of the solvated ZrO^+ complexes). The spectrum of ZrO^+Ar

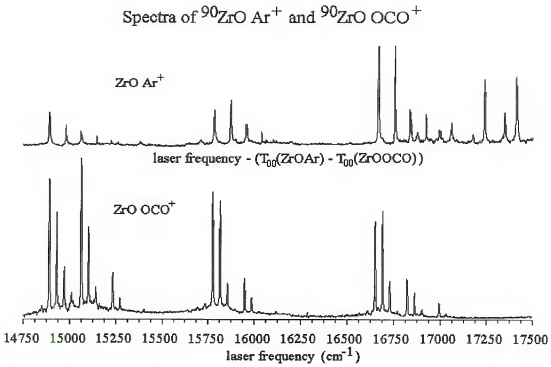
Spectra of ^{90}ZrO Ar$^+$ and ^{90}ZrO OCO$^+$
ZrO Ar$^+$
laser frequency - (T_{00}(ZrOAr) - T_{00}(ZrOOCO))
ZrO OCO$^+$
14750 15000 15250 15500 15750 16000 16250 16500 16750 17000 17250 17500
laser frequency (cm^{-1})

Figure 7-1. Portions of the photodissociation spectra of two ZrO^+ solvated complexes.

The spectrum of ZrO^+ Ar has depicted in such a way so as to display the origins (T_{00}) of both molecules at the same relative frequency. Present in both spectra is an electronic system with excited state progressions in the ZrO^+ diatomic stretch, the ZrO^+ ↔ (ligand) complex stretch, and the ZrO^+∢ (ligand) complex linear angle bend.

is presented alone in fig. 7-2 and is labeled by the three quantum numbers which describe the observed motions. Transitions in the unique state have yet to suffer full analysis, however the vibronic band positions were fit to eqn 7-1 and the constants obtained from this initial analysis indicate an electronic origin ~400 cm^{-1} to higher energy than that observed for the A-state. A summary of these constants is provided in Table 7-3 along with those determined for the A-state.

Table 7-2. Vibronic band positions (cm^{-1}) for the A-X transitions of $^{90}ZrO^{+}OCO$ and $^{90}ZrO^{+}Ar$.

v'_{ZrO}	v'_{str}	v'_{bnd}	$^{90}ZrO^{+}$ OCO	$^{90}ZrO^{+}$ Ar
0	0	0	14892.0	15459.1
0	0	2	14931.6	15546.9
0	0	4	14971.7	15635.5
0	0	6	15011.2	
0	1	0	15064.1	15627.8
0	1	2	15103.2	15714.0
0	1	4	15142.5	
0	2	0	15234.9	15793.3
0	2	2	15273.2	
0	3	0	15403.0	
1	0	0	15776.0	16351.9
1	0	2	15815.6	16440.0
1	0	4	15855.3	16528.5
1	0	6	15895.3	
1	1	0	15947.8	16520.3
1	1	2	15987.6	16607.0
1	1	4	16026.0	
1	2	0	16119.2	16686.2
1	3	0	16287.7	
2	0	0	16653.1	17237.2
2	0	2	16692.9	17325.6
2	0	4	16732.0	17414.2
2	1	0	16825.2	17406.4

Table 7-2. (continued)

2	1	2	16864.6	17492.8
2	1	4	16903.2	
2	2	0	16996.1	17572.3
3	0	0	17524.2	18116.7
3	0	2	17563.1	
3	0	4	17603.0	

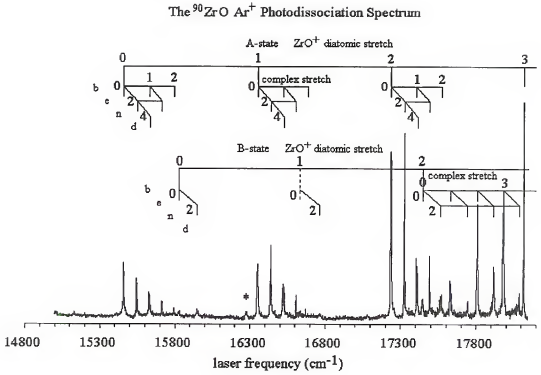

Figure 7-2. The ZrO^+ Ar photodissociation spectrum.

The presence of two electronic systems has been identified. The B-state is unique and only found in ZrO^+Ar. The asterisk indicates a vibrational hot band in the bending vibrational progression of the A-state

Table 7-3. The vibrational constants derived for two states of ZrO^+Ar (cm^{-1}).

	A-state	B-state
T	14904	15290
T_{00}	15459	15830
ω'_{ZrO}	900	840
ω'_{Sstr}	170	190
ω'_{bnd}	43	56

In figs. 7-3 and 7-4 the ZrO^+ diatomic vibrational energy has been subtracted from each member of the progression and the intensities replotted with a constant vertical offset. This "overlapped" rendition of the spectra clearly demonstrates the reproducibility of the vibronic substructure with different final state ZrO^+ vibrational quantum and thus indicates little anharmonic coupling of this mode to the other low frequency modes of the molecules. In figs. 7-2 and 7-3, an asterisk marks a weak feature which has been

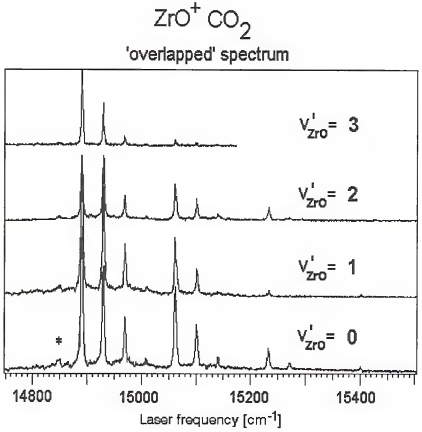

Figure 7-3. The "overlapped" rendition of ZrO^+ OCO.

The vibrational structure repeats with successive quanta of ZrO^+ diatomic stretch. From this reproducibility it is obvious that this particular mode is not significantly coupled to the lower frequencies of the molecular complex that are associated with the concerted motion of the ligand CO_2 moving with respect to the diatomic ion.

identified as hot bands in the complex bending motion. Given the high symmetry of the states connected by these transitions and the selection rules governing these transitions, the presence of these hot bands indicate a significant increase in the vibrational frequency of the ground state bending mode.

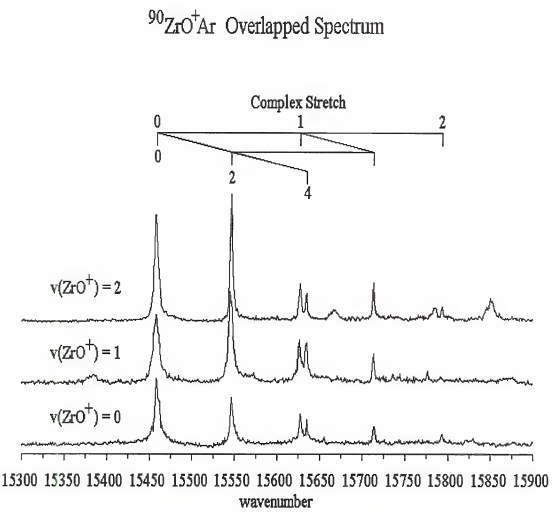

Figure 7-4. The "overlapped" rendition of $ZrO^{+}Ar$.

Although the intensity distribution of the electronic transitions alone is enough to accurately assign vibrational quantum numbers to the observed motions, the presence of naturally occurring zirconium isotopes and the simultaneous monitoring of the action of $^{92}ZrO^{+}Ar(OCO)$ and $^{94}ZrO^{+}Ar(OCO)$ as a function of laser frequency confirms these assignments. The electronic transitions of these isotopic varients yield vibrational constants which differ due to the change in mass alone. Because of the simple separable

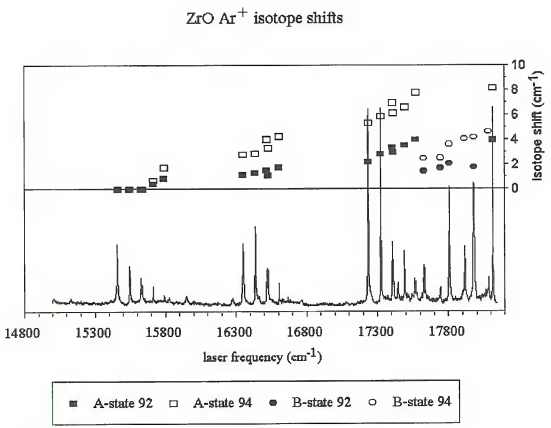

Figure 7-5. The isotopic analysis of $ZrO^{+}Ar$.

The top panel shows the observed red-shift in the spectral features of the heavier isotopic varients of $ZrO^{+}Ar$. The spectral shifts are depicted at the same horizontal position as the corresponding features in the observed spectrum which is reproduced in the bottom panel.

nature of the intramolecular forces in these complexes, we expect an isotope shift on the vibrational energy of the diatomic stretch in the ZrO^+ moiety to be related to the change in the reduced mass of that diatomic. We furthermore, expect that isotope shifts of successive quanta of the complex stretch to be influenced by the change in reduced mass of the pseudo-diatomic with ZrO^+ representing one pseudo-atom and Ar (CO_2) representing the other pseudo-atom. Figure 7-5 shows a depiction of the isotopic substitution results for ZrO^+Ar. The top panel shows the observed red-shift in the spectral features of the $^{92}ZrO^+Ar$ relative to that of the $^{90}ZrO^+Ar$ spectrum (solid symbols) and similarly the red shift of the $^{94}ZrO^+Ar$ relative to that of the $^{90}ZrO^+Ar$ spectral features in the open symbols. These spectral shifts are depicted at the same horizontal position (laser frequency) as the features they correspond to in the $^{90}ZrO^+Ar$ spectrum, which is repeated in the lower panel. These isotope shifts are quantitatively predicted by the diatomic and pseudo-diatomic approximations for the internal solute stretch and the solute-solvent stretching motions. The isotope shifts accompanying the complex bending motion has yet to be unambiguously analyzed.

Assuming electrostatics is the driving force in bond formation, it is expected that the ZrO^+Ar complex is linear and the three modes identified is the full compliment of expected motions. The primary attraction is the permanent dipole-(induced-dipole) force, however the permanent dipole of ZrO^+ is of larger magnitude than a static transition metal monopole with a full positive electron charge. This is born out by comparing the complex stretching bond force constant of Zr^+OAr (table 8-1) with the force constants of *any* M^+Ar complex measured in our lab or detailed in this dissertation. The linearity of ZrO^+OCO is

also inferred by the similarities in the dissociation spectra observed between these two molecules. Additionally, owing to the large quadrupole moment of CO_2, the electrostatic minimized geometry is linear with the negative quadrupole moment of CO_2 aligned with the positive end of the ZrO^+ dipole. Of the 3N - 5 = 10 vibrational modes possible for a linear ZrO^+OCO, only 3 are observed which are the pure solute ZrO^+ stretch, the solute-solvent symmetric stretch and one of two degenerate linear angle bends associated with the complex bond. The remaining modes are intrinsic to the solvent CO_2 and not expected to be observed in photodissociation.

$\underline{ZrO^+N_2}$

The four molecules in this study have been presented separately due to inherent differences associated with the vibrational structure, namely the presence of a fourth vibrational mode has been identified in both ZrO^+N_2 and ZrO^+CO. Figure 7-6 presents the photodissociation spectra observed for ZrO^+N_2. The same type of repeating substructure is clearly evident and is due to a progression of three quanta in the solute ZrO^+ diatomic stretching mode. Figure 7-7 displays a highlight of the spectrum close to the electronic origin and shows the assignment of the vibrational substructure as progressions in three lower frequency modes. Up to three quanta of complex $ZrO^+ \leftrightarrow N_2$ symmetric stretch combined with up to five quanta of the $ZrO^+ \measuredangle N_2$ bending mode has been identified. The progression in the third (unique) complex motion has been labeled the asymmetric stretch and renders a frequency which is just less than the $ZrO^+ \leftrightarrow N_2$ symmetric stretch (Table 7-1).

This motion contains 0 to 3 quanta of excitation which occurs congruently with 0 to 4 quanta of the low frequency $ZrO^+ \sphericalangle N_2$ bending mode. This unique progression is of much weaker relative intensity yet, albeit weak, repeats regularly with successive quanta of ZrO^+ diatomic stretch.

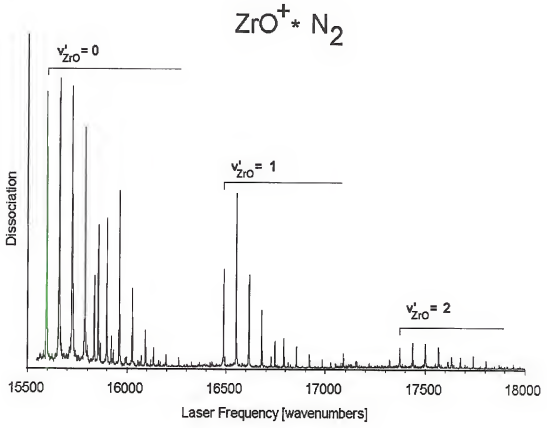

Figure 7-6. A portion of the photodissociation spectrum of $^{90}ZrO^+N_2$.

Progressions in the three lower frequency modes can be seen as repeating patterns on the labeled ZrO^+ diatomic stretch.

Table 7-4. Cold vibronic band positions (cm^{-1}) for the $^{90}ZrO^{+}N_2$ molecule.

v'_{ZrO}	$v'_{Ss\,tr}$	v'_{Asym}	v'_{bnd}	$^{90}ZrO^{+}N_2$ observed
0	0	0	0	15598.12
0	0	0	1	15661.25
0	0	0	2	15725.55
0	0	0	3	15790.72
0	0	0	4	15856.98
0	0	0	5	15923.81
0	1	0	0	15838.74
0	1	0	1	15901.36
0	1	0	2	15965.38
0	1	0	3	16030.06
0	1	0	4	16095.57
0	1	0	5	16161.56
0	2	0	0	16075.25
0	2	0	1	16137.88
0	2	0	2	16200.76
0	2	0	3	16264.83
0	2	0	4	16329.84
0	3	0	0	16307.13
0	3	0	1	16369.37
0	3	0	2	16432.06
0	3	0	3	16495.85
0	0	1	0	15804.67
0	0	1	1	15868.94

v'_{ZrO}	$v'_{Ss\,tr}$	v'_{Asym}	v'_{bnd}	$^{90}ZrO^{+}N_2$ observed
0	0	2	2	16123.84
0	0	3	0	16171.77
1	0	0	0	16489.87
1	0	0	1	16553.53
1	0	0	2	16618.24
1	0	0	3	16683.10
1	0	0	4	16749.66
1	0	0	5	16816.60
1	1	0	0	16730.64
1	1	0	1	16793.71
1	1	0	2	16857.55
1	1	0	3	16922.49
1	1	0	4	16987.91
1	2	0	0	16967.28
1	2	0	1	17029.89
1	2	0	2	17093.18
1	2	0	3	17156.77
1	2	0	4	17222.13
1	3	0	2	17324.58
1	3	0	3	17388.93
1	4	0	2	17552.13
1	0	1	0	16697.71
1	0	1	1	16761.66

Table 7-4. (Continued)

$v'_{Zr\,O}$	v'_{Sstr}	v'_{Asym}	v'_{bnd}	$^{90}ZrO^{+}N_2$ observed
0	0	1	2	15934.56
0	0	1	3	16000.62
0	0	1	4	16067.14
0	0	2	0	15994.91
0	0	2	1	16058.87
2	0	0	0	17374.40
2	0	0	1	17438.79
2	0	0	2	17503.26
2	0	0	3	17568.78
2	0	0	4	17634.99
2	0	0	5	17701.81
2	1	0	0	17615.69
2	1	0	1	17678.81

$v'_{Zr\,O}$	v'_{Sstr}	v'_{Asym}	v'_{bnd}	$^{90}ZrO^{+}N_2$ observed
1	0	1	2	16827.32
1	0	2	0	16887.17
1	0	2	1	16950.38
1	0	2	2	17015.50
1	0	3	0	17063.92
2	1	0	2	17742.79
2	1	0	3	17808.22
2	1	0	4	17873.33
2	2	0	0	17851.90
2	2	0	1	17914.75
2	2	0	2	17979.07
2	0	1	0	17581.44
2	0	1	1	17646.43

Table 7-4 lists all cold band vibronic transitions of appreciable intensity in the ZrO^+N_2 spectrum which were fit to eqn 7-1 and the constants extracted from this fit are found in Table 7-1. Isotopic analysis of the resonant spectral features of figs. 7-6 and 7-7 assure that the lowest energy, intense transition is indeed the electronic origin.

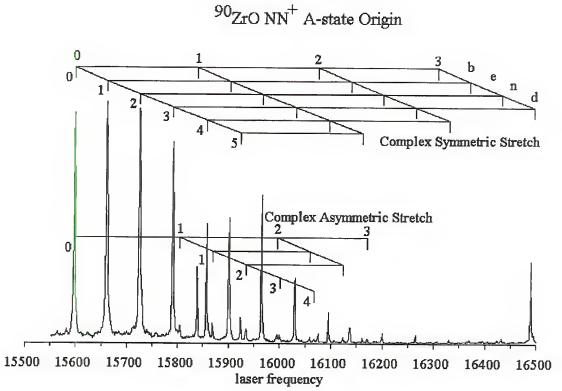

Figure 7-7. Assignment of the lower frequency modes of ZrO^+N_2.

Progressions in the complex symmetric stretch, asymmetric stretch, and bending mode have been identified and labeled by upper state vibrational quantum number. This pattern repeats with successive quanta of solute diatomic stretch.

Assuming electrostatics governs bond formation and therefore assuming the linear geometry of the ground and excited states of $ZrON_2^+$, there are 3N - 5 = 7 vibrational modes possible, two of which are doubly degenerate. A representation of these modes has been provided in fig. 7-8 along with an "in house" description of these modes. This is not in convention with historical descriptions of the vibrating nuclei but rather these terms were chosen to provide a convenient nomenclature for purposes of this manuscript. The symmetric N_2 stretch is a pure solvent mode and not observed in the photodissociation

The Possible Vibrational Modes of Linear, Symmetric ZrO^+ N_2

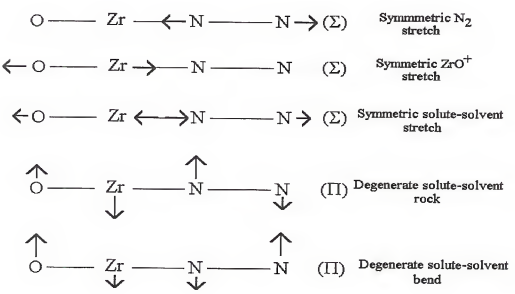
O —— Zr ←— N ——— N → (Σ)
Symmmetric N2 stretch
← O —— Zr → —— N ——— N (Σ)
Symmetric ZrO+ stretch
← O —— Zr ←→ N ——— N → (Σ)
Symmetric solute-solvent stretch
O —— Zr ——— N ——— N (Π)
Degenerate solute-solvent rock
O —— Zr ——— N ——— N (Π)
Degenerate solute-solvent bend

Figure 7-8. The normal modes of a linear 4-atom polyatomic.

A representation of the vibrational modes of linear $ZrON_2^+$ showing the nuclear displacement during normal vibrations. The symmetry species of the vibration is shown in parenthesis along with a description of the vibration taking place. The displacement vectors are not drawn to scale.

spectrum of fig. 7-6. Vibrational progressions have, however, been identified in four modes of $ZrON_2^+$ and therefore, these four modes must be represented by the remaining four diagrams of fig. 7-8 (assuming the linear geometry). The symmetric Zr^+-O stretching vibration is a pure solute mode with a frequency (898 cm^{-1}) which barely deviates (~.1%)

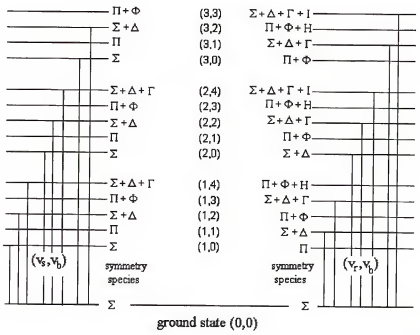

Figur 7-9. Possible transitions between linear states of a 4-atom polyatomic molecule.

On the left, low frequency degenerate bending vibrational levels are built upon higher frequency symmetric vibrational levels. Those transitions which connect with the totally symmetric ground state occur only for even quantized bending vibrational levels. To the right, multiple excitations in low and high frequency degenerate vibrational modes are indicated. Only when the quantum of both degenerate modes are of the same sense (both even or both odd) then the levels have the appropriate Σ vibrational symmetry species and are observed in cold absorption.

from those observed in it's brethren molecules (Table 7-1). The remaining three complex modes must now be labeled in accord with figure 7-8. It shall be assumed that the highest frequency (243 cm^{-1}) complex mode is the symmetric solute-solvent stretch. The two complex linear angle bends of fig. 7-8 should be nearly degenerate and of much lower frequency than the complex stretching mode. Unfortunately, however, the two remaining mode frequencies are not nearly degenerate (224 and 63 cm^{-1}) and only one is significantly less. Rather arbitrarily, the rocking motion of fig. 7-8 is assigned as the 224 cm^{-1} mode and the solute-solvent bend is assigned as the 63 cm^{-1} mode and this is realized as the first real shortcoming of the assumed excited state linear geometry.

Due to the high symmetry of this proposed linear polyatomic molecule, additional selection rules are applicable to transitions connecting the states of linear geometries. These selection rules stem from the Franck-Condon factor or vibrational overlap integral. In a symmetrical molecule, in order for this integral to be non-zero, the integrand must be symmetric or, for degenerate vibrational levels, a product of appropriate vibrational eigenfunctions must be totally symmetric. In other words, only those levels of the same vibrational symmetry species in the upper as in the lower state can combine.

In figure 7-9 a qualitative representation of the possible transitions between linear states of a (at least) 4-atom polyatomic molecule is presented. The splitting between vibrational levels has been neglected and the figure further assumes that vibronic coupling is negligible. Multiple excitations in the low frequency degenerate solute-solvent bending mode have been represented and on the left of fig. 7-9 these vibrational levels are simultaneously excited with the symmetric solute-solvent stretching vibrations and appear

"built" upon these vibrational levels. To the right, the bending vibrational levels occur with the degenerate solute-solvent rocking motion of the molecule. The symmetry allowed transitions are portrayed as solid lines connecting the bending vibrational levels with the vibrationless (symmetry species Σ) ground state. From the left of fig. 7-9, it is apparent that when symmetric and degenerate vibrations are multiply excited, only those transitions occur for even quantized bending vibrational levels. However, when two degenerate motions are multiply excited, the quantum of the observed bending vibrational level appears to cycle between even and odd integers and changes as the quantum of excitation in the degenerate rocking vibration changes.

This protocol applied to the excited vibrational structure of ZrO^+N_2 predicts the presence of "holes" in the dissociation spectra. A simple pattern of transitions separated by twice the bending frequency is expected for all bending vibrational levels, however, for those levels which are multiply excited in the degenerate modes, this cycling between only even and then only odd bending vibrational levels would leave a discernible "gap". These holes are not present in ZrO^+N_2 dissociation spectrum and thus these selection rules governing transitions between states of high symmetry fail to describe the vibrational structure of ZrO^+N_2. This failure indicates an excited state of lower geometric symmetry (probably C_{2v}). As the vibrational analysis indicates an excited state of lowered symmetry, the quantum numbers assigned to the bending vibrational modes increment by unity.

ZrO^+CO

Up to this point, the spectra of the solvated ZrO^+ complexes boasted similar Franck-Condon factors in which the intensity more or less peaked at the origin. This had the effect of allowing only relatively short vibrational progressions in the lower frequency modes which yielded the unambiguous identification of the solute ZrO^+ stretching progression. Additionally, this suggests similar geometries and binding mechanisms associated with the ground and excited states. Figure 7-10 presents the photodissociation spectrum of ZrO^+CO which displays a unique Franck-Condon overlap with the ground state. In fact, the ZrO^+ stretching progression is completely washed out and the electronic origin is not directly observed. However congested, the spectrum of fig. 7-10 was analyzed and found that only four quantum numbers, their squares, and a single constant term (the electronic origin) quantitatively described nearly every observed resonant transition. In other words, these four quantum numbers describe four different modes of motion which evolve from a single electronic transition in analogous fashion to ZrO^+N_2. The vibrational frequencies associated with these motions are given in Table 7-1 along with the remaining vibrational constants. The assignment of the resonant transitions are provided in Table 7-4.

The same reproducibility associated with successive quanta of ZrO^+ stretching vibration is evident in the overlapped spectrum of fig. 7-11. Here the approximate solute diatomic stretching frequency (~900 cm^{-1}) has been subtracted from the energy axis of the top trace and the offset intensities replotted. The agreement between traces in conjunction

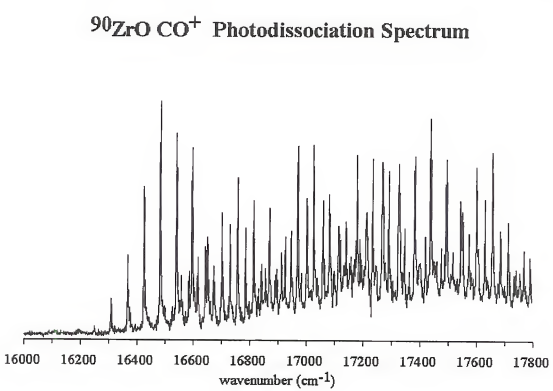

Figure 7-10. A portion of the photodissociation spectrum for ZrO^+CO.

The unique nature of this spectrum is due to unfavorable Franck-Condon overlap with the lower vibrational levels.

with the diatomic stretching frequency assures that the spectrum of ZrO^+CO is attributable to the same electronic transition evident in all the solvated ZrO^+ complexes.

Figure 7-12 shows the assignment of the resonant vibrational structure of ZrO^+CO in terms of the ZrO^+ diatomic stretch and the solute-solvent complex modes. The dashed lines in the figure indicate the calculated positions of the unobserved electronic origin transition and the first member of the progression excited in the diatomic stretching motion. The previously dubbed "unique mode" which is labeled as the asymmetric

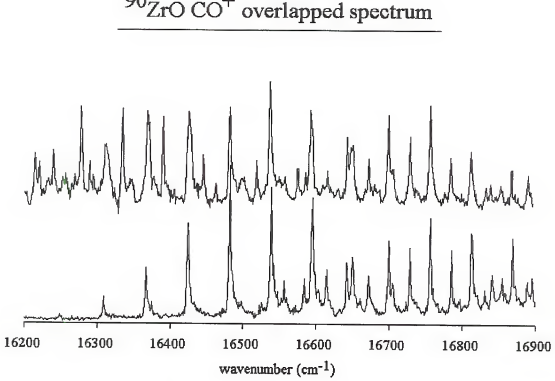

Figure 7-11. The "overlapped" rendition of the $^{90}ZrO^+CO$ spectrum.

The frequencies of the top trace have been shifted by the approximate ZrO^+ diatomic stretching frequency (900 cm-1). The reproducibility of even this complicated spectrum with successive solute stretching quantum numbers is obvious.

stretching motion in fig. 7-10 is considerably more intense in ZrO^+CO relative to ZrO^+N_2 and is due to differences in the Franck-Condon overlap. As in ZrO^+N_2, the frequency of this mode is substantially greater than the complex vibrational bending frequency and analogous arguments of the failure of the "high symmetry" selection rules to provide a suitable description of the resonant vibronic structure indicates that this excited state of ZrO^+CO is also *non-linear*.

Table 8-4. Band positions (cm^{-1}) of $^{90}ZrO^{+}CO$

v'_{ZrO}	v'_{Stir}	v'_{Asym}	v'_{bnd}	$^{90}ZrO^{+}CO$ observed
0	0	1	3	16308.47
0	0	1	4	16366.70
0	0	1	5	16424.62
0	0	1	6	16481.60
0	0	1	7	16538.20
0	0	1	8	16594.10
0	0	1	9	16649.81
0	0	1	10	16704.94
0	0	2	3	16525.70
0	0	2	4	16584.60
0	0	2	5	16641.91
0	0	2	6	16699.57
0	0	2	7	16756.09
0	0	2	8	16812.22
0	0	2	9	16868.66
0	0	2	10	16924.29
0	0	3	4	16796.50
0	0	3	5	16854.43
0	0	3	6	16911.68
0	0	3	7	16968.60
0	0	3	8	17024.99
0	0	3	9	17080.71
1	0	0	7	17212.14

v'_{ZrO}	v'_{Sstr}	v'_{Asym}	v'_{bnd}	$^{90}ZrO^{+}CO$ observed
1	0	1	6	17380.66
1	0	1	7	17436.19
1	0	1	8	17492.57
1	0	1	9	17547.01
1	0	1	10	17603.53
1	0	2	4	17485.05
1	0	2	5	17541.84
1	0	2	6	17598.46
1	0	2	7	17654.66
1	0	2	8	17710.98
1	0	2	9	17766.02
0	2	0	1	16556.14
0	2	0	2	16614.47
0	2	0	3	16671.98
0	2	0	4	16728.72
0	2	0	5	16784.85
0	2	0	6	16840.57
0	2	0	7	16895.37
0	3	0	1	16830.36
0	3	0	2	16888.36
0	3	0	3	16945.59
0	3	0	4	17001.35
0	3	0	5	17058.28

Table 8-4. Band positions (cm^{-1}) of $^{90}ZrO^{+}CO$

v'_{ZrO}	v'_{Str}	v'_{Asym}	v'_{bnd}	$^{90}ZrO^{+}CO$ observed	v'_{ZrO}	v'_{Sstr}	v'_{Asym}	v'_{bnd}	$^{90}ZrO^{+}CO$ observed
1	0	0	8	17270.59	0	3	0	6	17113.55
1	0	0	9	17326.65	1	1	0	1	17176.87
1	0	1	4	17267.70	1	1	0	2	17233.13
1	0	1	5	17325.23	1	1	0	3	17289.62
1	1	0	4	17345.02	1	2	0	5	17682.94
1	2	0	2	17514.92	1	3	0	0	17674.58
1	2	0	3	17571.41	1	3	0	1	17731.41
1	2	0	4	17627.43	1	3	0	2	17788.37

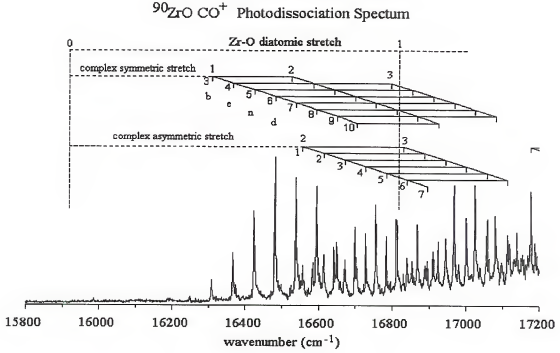

Figure 7-12. The mode assignment of ZrO^+CO.

The motions of the complex that involve the vibration of the diatomic solute with respect to the solvent have been assigned. Three different complex modes have been identified and labeled by quantum number. The dashed lines indicate the transition frequencies of unobserved band origins in the ZrO^+ diatomic stretch.

Discussion

The electronic transition responsible for the presented spectra is due to the solute ZrO^+ chromophore and thus the spectra of the four molecular ions presented have shown substantial similarities. In fact, the ZrO^+ stretching frequency changes by less than 0.1% from one complex to the other. It is, however, in the complex motion that substantial changes are evident and these changes result from the geometry of the molecule and the

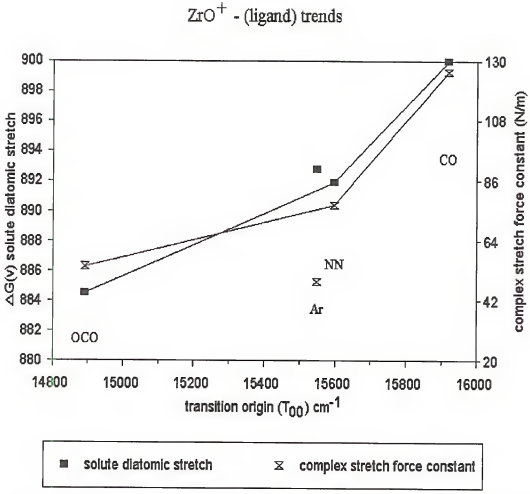

Figure 7-13. Trends and correlations between the various physical properties of solvated ZrO^+.

solute-solvent binding mechanism. Unfortunately, the actual solute-solvent binding energies were not measured but, however we may assume that the complex stretching force constant provide a relative measure of the bonding (as observed in the $CoRG^+$ systems of chapter 4). These force constants are provided in table 7-1 and were obtained assuming the complex acts as a pseudo diatomic with the solute ZrO^+ moiety acting as one pseudo atom and the rigid solvent ligand acting as the other pseudo atom. The ordering of the complex stretching force constants of Table 8-1 are $k_{(ZrO+Ar)} < k_{(ZrO+OCO)} < k_{(ZrO+N2)}$

$< k_{(ZrO+CO)}$ and we may further assume that the solute-solvent binding energies follow the same trend. The transition origins exhibit this same general trend (with the exception of ZrO^+Ar) thus indicating ground states which are more strongly bound than the excited states. The correlation of some of these properties are presented in fig. 7-13. Here the horizontal axis provides the transition origin (T_{00}) and the vertical axes display both $\Delta G(v)$ for the ZrO^+ solute and the complex bond force constant. The $ZrOAr^+$ force constant seems out of place, however ignoring this exception, it seems both properties are well correlated together and to the electronic origin. Interestingly, there is a general increase in solute diatomic frequency with complex force constant (or bond energy).

The only known optical transition in ZrO^+ is the $A\ ^2\Pi$-$X\ ^2\Sigma$ which was rotationally analyzed via plasma emission spectroscopy [69, 70]. The origin of this system is at 12 500 cm^{-1} with a spin orbit constant of 595 cm^{-1}. The data presented here indicates that this electronic transition is probably the chromophore for the absorption observed in the solvated molecules presented in this study. Measurement of the vibrational frequency of the $A\ ^2\Pi$ of ZrO^+ and plotting this frequency at 12 500 cm^{-1} in fig 7-13 would either make or break the above assignment and so the hunt for this value is on.

Assignment of a T-shaped transition-metal N_2 complex ion is not unheard of [chapter 6]. In that case, the assignment was based on unresolved and unexpected rotational structure in conjunction with an unexplainably large ground state dissociation energy. Similarities between the former (CoN_2^+) and the latter ZrO^+N_2 are seen. In both molecules electrostatics fail in the description of the bonding with the side on coordination appearing as a saddle point in the electrostatic geometric minimization.

The nature of the bonding present may best be described by the ZrO^+ inserting into the triple bond of $N_2(CO)$ and this interaction displaying much more covalent forces. The covalency of this bond then provides reason for the substantial increase in force constant (bond energy) seen in $ZrO^+N_2(CO)$ with respect to ZrO^+OCO. The frequency of the third complex mode observed in $ZrO^+N_2(CO)$ but not in $ZrO^+OCO(Ar)$ is much more reminiscent of bond compression and stretching and was thus labeled the asymmetric stretch. Figure 7-14 displays the modes and assigned frequencies in the ZrO^+N_2 complex. The vibrational symmetry designations of the various modes are also indicated. We are

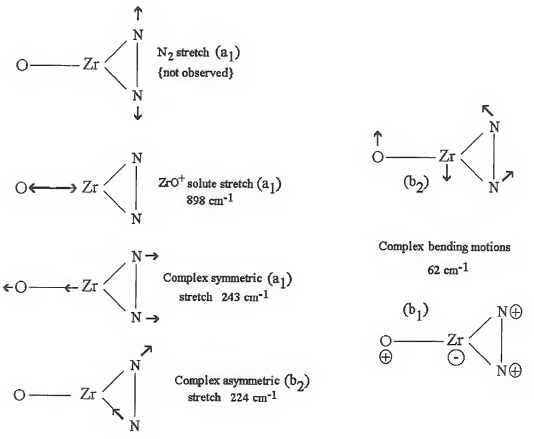

Figure 7-14. The assigned modes of motion of ZrO^+N_2

unable to differentiate between the two low frequency complex bending motions, but these frequencies are expected to be nearly degenerate.

As these assignments may meet with sufficient speculation, a final aliquot of supporting evidence is supplied via the vibrational isotope effect between ^{94}Zr and ^{90}Zr. The relative amplitude of vibration of a certain nucleus is dependent upon the geometrical arrangements of the nuclei. Isotopic substitution of nuclei result in significant vibrational shifts only when that nucleus is displaced from its equilibrium position during the vibration. We therefore expect that the isotopic shift associated with substituting ^{94}Zr for ^{90}Zr to be significant for all vibrational modes of motion except the asymmetric stretch of fig. 7-14. Figure 7-15 shows the isotopic substitution results for the various motions observed in ZrO^+N_2. The measured $^{90}ZrO^+N_2$ - $^{94}ZrO^+N_2$ isotope shifts have been superimposed onto the observed dissociation spectrum of $^{90}ZrO^+N_2$. The transitions marked with an asterisk are "pure" in that they do not contain excitation in the low frequency mode, however progressions in this mode are connected by solid lines. Each different symbol represents a different high frequency motion with 0-5 quanta of excitation in the low frequency mode. The transition at ~ 15 800 cm^{-1} is the first member in a progression of the asymmetric mode and contains a single quantum of excitation in this motion. Compare this observed isotope shift with that for the transition excited by a single quantum of stretching motion (~15 840 cm^{-1}). Comparing the isotope shifts for the doubly excited "pure" members of these progressions only provides credence for the assignments made.

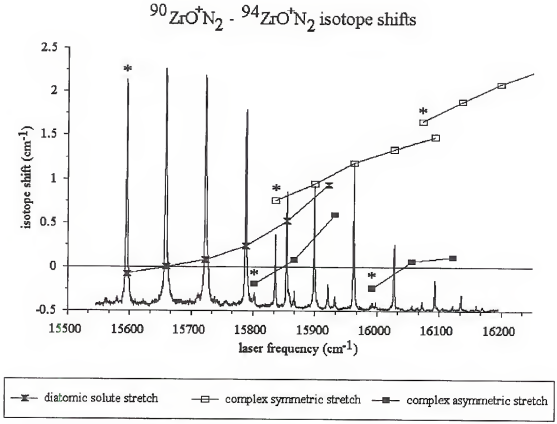

Figure 7-15. The measured (^{94}Zr-^{90}Zr)isotope shifts superimposed upon the $^{90}ZrO+N_2$ spectrum.

The transitions marked by an asterisk contain no excitation in the low frequency modes. The negligible isotope shifts observed for successive quanta of excitement in the complex asymmetric stretch indicate that the amplitude of motion of the Zr^+ within this mode is also negligible.

CHAPTER 8
CONCLUDING REMARKS

The big picture. The acquisition and analysis of a single molecule's spectrum is praise worthy, however, it is only when many spectra are simultaneously analyzed that the true power of comparisons unfold. It is from these "big pictures" that we develop expectations and our chemical intuition sharpens. We are typically unaware of this intuition until the occurrence of the unexpected.

Various molecular spectra have been presented. Normally, what one would expect to find is what one does finds and the development of the all important "trend" occurs. These trends, however, bear their greatest utility when they are violated. These violations force us to rethink our initial positions and render physical reasons for the interpretation of the unexpected phenomena. Twice within the pages of this dissertation has the analysis of a "trend breaker" been presented. Both involved the analysis of transition metal containing ions bound to N_2 (which incidently starts a new trend).

Both ionic complexes broke trend by their uncharacteristic binding energy. This enhanced bonding was interpreted as covalency which stemmed from the transition metal ion inserting into the triple bond of the N_2. Evidence (independent of the bond energy) in both spectra was the indication of the non-linear association of N_2 to the transition metal containing complex ions. In CoN_2^+, this evidence was unresolved rotational structure and in ZrO^+N_2, the vibrational structure of the various modes in conjunction with selections

rules and isotopic shifts indicated the non-linearity of the complex ion. Unfortunately, the smoking gun (resolved rotational structure) was never found. Despite this, a wealth of circumstantial evidence has been accrued and all point to a partially inserted, partially covalent geometry.

REFERENCES

[1] STAR TREK, THE NEXT GENERATION, episode 117, Home Soil. 20th Century Fox.

[2] M. S. Kim, R. E Smalley, L. Wharton, and D. H. Levy, J. Chem. Phys., 65, 1216 (1976).

[3] W. C. Wiley and I. H. McLaren, *The Review of Scientific Instruments*, 26, 1150, (1955).

[4] D. Bellert, T. Buthelezi, V. Lewis, K. Dezfulian, D. Reed, T. Hayes and P. J. Brucat, Chem. Phys. Lett.,256, 555 (1996).

[5] D. Bellert, T.Buthelezi, T. Hayes and P. J. Brucat, Chem. Phys. Lett., 276, 242 (1997)

[6] D. Bellert, T. Hayes, T. Buthelezi and P. J. Brucat, Chem. Phys. Lett. 287 22 (1998).

[7] C. T. Scurlock, J. S. Pilgrim, and M. A. Duncan, J. Chem Phys., 103, 3293 (1995)

[8] S. H. Pullins, C. T. Scurlock, J. E. Reddic, and M. A. Duncan, J. Chem. Phys. 104, 7518, (1996).

[9] Sergey I. Panov, James M. Williamson and Terry A. Miller, J. Chem. Phys. 102, 7359, (1995).

[10] Ch. Luder and M. Velegrakis, J. Chem. Phys. 105 2167, (1996).

[11] D. Lessen and P. J. Brucat, J. Chem. Phys. 90 6296 (1989).

[12] D. E. Leswsen, R. L. Asher, and P. J. Brucat, Chem. Phys. Lett. 177 380 (1991).

[13] R. L. Asher, D. Bellert, T. Buthelezi, and P.J. Brucat, Chem Phys. Lett. 228 599 (1994).

[14] R. L. Asher, D. Bellert, T. Buthelezi, Dan Lessen, and P. J. Brucat, Chem. Phys. Lett. 234 119 (1995).

[15] D. Lessen and P. J. Brucat, J. Chem. Phys. 91 4522 (1989).

[16] D. Bellert, T. Buthelezi, K. Dezfulian, T. Hayes and P. J. Brucat, Chem. Phys. Lett. 256 555 (1996).

[17] T. Buthelezi, D. Bellert, T. Hayes and P. J. Brucat, Chem. Phys. Lett. 262 303 (1996).

[18] D. Bellert, T. Buthelezi, T. Hayes and P. J. Brucat, Chem. Phys. Lett. 277 27 (1997).

[19] T. Hayes, D. Bellert, T. Buthelezi, and P. J. Brucat, Chem. Phys. Lett. 287 22 (1998).

[20] H. Partridge and C. W. Bauschlicher Jr., J. Phys. Chem. 98 2301 (1994).

[21] R. J. LeRoy and R. B. Bernstein, J. Chem. Phys. 52, 3869 (1970); R. J. LeRoy and R. B. Bernstein, J. Mol. Spectrosc. 37 109 (1971).

[22] H. J. Fischbeck and K. H. Fischbeck, *Formulas Facts and Constants, 2ed.*, (Springer-Verlag, New York, 1987).

[23] C. J. F. Botcher and P. Bordewijk, *Theory of Electric Polarization Vol II* (Elsevier, Amsterdam, 1978).

[24] R. T. Birge and H. Sponer, Physic. Rev. 28 259 (1926).

[25] C. E. Moore, *Atomic Energy Levels*, Natl. Bur. Stand. Circ. 467 (U.S.GPO, Washington D.C., 1952).

[26] N. Aristov and P. B. Armentrout, J. Phys. Chem. 90 5135 (1986).

[27] H. Partridge and C. W. Bauschlicher Jr., and S. R. Langhoff, J. Phys. Chem. 96 5350 (1992).

[28] R. L. Asher, D. Bellert, T. Buthelezi, and P. J. Brucat, Chem. Phys Letters 227 (1994) 277.

[29] T. Buthelezi, D. Bellert, V. Lewis and P. J. Brucat, Chem. Phys. Lett. 242 627 (1995).

[30] J. Winn, *Physical Chemistry* (Harper Collins, New York, 1995).

[31] A. A. Radzig and B. M. Smirnov, *Reference Data on Atoms, Molecules and Ions*, Springer-Verlag, Berlin Heidelberg (1985).

[32] R. L. Asher, D. Bellert, T. Buthelezi, V. Lewis, and P. J. Brucat, Chem. Phys. Lett. 234 113 (1995).

[33] D.R. Lide (editor) *CRC Handbook of Chemistry and Physics*, 71st ed. 1990-91, CRC Press, Boston (1990).

[34] D. Stogryn and A. P. Storgyn, Mol. Phys. 11 319 (1966).

[35] G. Herzberg, *Spectra of Diatomic Molecules* (van Nostrand Reinhold, New York, (1950).

[36] C. W. Bauscnlicher, H. Partridge, and S. R. Langhoff, J. Phys. Chem. 96 2475 (1992).

[37] C. Heinemann, J. Schwarz, and H. Schwarz, J. Phys. Chem. 100 6088 (1996).

[38] C. Adamo, R. Telesca, F. Lelj, Chem. Phys. Lett. 254 314 (1996).

[39] M. Rsoi and C. W. Bauschlicher, J. Chem. Phys. 92 1876 (1990).

[40] S. R. Langhoff, C. W. Bauschlicher, H. Partridge, and M. Sodupe, J. Phys. Chem. 95 10677 (1991).

[41] E. U. Condon and G. H. Shortley, *The Theory of Atomic Spectra*, Cambridge University Press, 1959.

[42] J. S. Griffith, *The Theory of Transition-Metal Ions*, Cambridge University Press, 1961.

[43] Griffith and Orgel, *An Introduction to Transition Metal Chemistry*, Meuthen, London, (1960).

[44] S. F. Rice, H. Martin, and R. W. Field, J. Chem. Phys. 82 5023 (1985).

[45] E. M. Spain and M. D. Morse, J. Chem. Phys. 97 4641 (1992).

[46] R. S. Ram, P. F. Bernath, and S. P. Davis, J. Mol. Spectrosc. 175 1 (1996).

[47] R. S. Ram, P. F. Bernath, and S. P. Davis, J. Chem. Phys. 104 6949 (1996).

[48] R. M. Badger, J. Chem. Phys. 2 128 (1934).

[49] JANAF Thermochemical Tables, 2nd Edition, NSRDS-NBS 37 (1971).

[50] M. J. Takebe, Chem. Phys. 78 7223 (1983).

[51] T. R. Powers and R. J. Cross, J. Chem. Phys. 58 626 (1973).

[52] M. Dieterle, J. N. Harvey, C. Heinemann, J. Schwartz, D. Schroder, and H. Schwarz, Chem. Phys. Lett. 277 399 (1997).

[53] C. T. Scurlock, S. H. Pullins, and M. A. Duncan, J. Chem. Phys. 105 3579 (1996).

[54] L. N. Ding, P. D. Leiber, Y. C. Cheng, M. A. Young, S. V. Oneil, and W. C. Stwalley, J. Chem. Phys. 102 5235 (1995).

[55] R. L. Asher, D. Bellert, T. Buthelezi, G. Weerasekera, and P. J. Brucat, Chem. Phys. Lett. 228 390 (1994).

[56] R. L. Asher, D. Bellert, T. Buthelezi, and P. J. Brucat, Chem. Phys. Lett. 227 623 (1994).

[57] C. S. Yeh, J. S. Pilgrim, K. F. Willey, D. L. Robbins, and M. A. Duncan, Int. Rev. Phys. Chem. 13 231 (1994).

[58] C. S. Yeh, K. F. Willey, D. L. Robbins, and M. A. Duncan, Int. J. Mass Spectrom. Ion. Proc. 131 307 (1994).

[59] J. Schwarz and H. Schrwarz, Organometallics, 13 1518 (1994).

[60] C. S. Yeh, K. F. Willey, D. L. Robbins, J. S. Pilgrim, and M. A. Duncan, J. Chem. Phys. 98 1867 (1993).

[61] C. S. Yeh, K. F. Willey, D. L. Robbins, and M. A. Duncan, J. Phys. Chem. 96 7833 (1992).

[62] K. F. Willey, C. S. Yeh, D. L. Robbins, and M. A.Duncan, Chem. Phys. Lett. 192 179 (1992).

[63] K. F. Willey, D. L. Robbins, C. S. Yeh, and M. A. Duncan, Faraday Discuss. 92 269 (1991).

[64] D. E. Lessen, R. L. Asher, and P. J. Brucat , J. Chem. Phys. 95 1414 (1991).

[65] M. Sodupe, V. Branchadell, A. Oliva, and J. Bertran, Int. J. Quantum. Chem. 63 523 (1997).

[66] M. Sodupe, V. Branchadell, M. Rosi, and C. W. Bauschlicher, Jr., J. Phys. Chem. 42 7854 (1997).

[67] M. Sodupe, C. W. Bauschlicher, Jr., H. Partridge, Chem. Phys. Lett. 192 185 (1992).

[68] R. L. Asher, D. Bellert, T. Buthelezi, and P. J. Brucat, J. Phys. Chem. 99 1068 (1995).

[69] J. G. Phillips, S. P. Davis, Astro. J. 234 393 (1979).

[70] W. J. Bslfour, B. Lindgren, Phys. Sce. 22 36 (1980).

BIOGRAPHICAL SKETCH

Darrin was born April 9, 1968 to Big Al and Mary Bellert. He attended Carroll High School in Dayton, Ohio where his first clip on tie was flushed down the toilet. After graduating in 1986, he attended Wright State University and graduated in 1992 with a B.S. in chemistry. As he is on the 6 year plan (and 6 years are up) he is graduating from the University of Florida with a Ph. D. in physical chemistry.

I certify that I have read this study and that in my opinion it conforms to acceptable standards of scholarly presentation and is fully adequate, in scope and quality, as a dissertation for the degree of Doctor of Philosophy.

Phillip J. Brucat, Chair
Associate Professor of Chemistry

I certify that I have read this study and that in my opinion it conforms to acceptable standards of scholarly presentation and is fully adequate, in scope and quality, as a dissertation for the degree of Doctor of Philosophy.

William Weltner, Jr.
Professor of Chemistry

I certify that I have read this study and that in my opinion it conforms to acceptable standards of scholarly presentation and is fully adequate, in scope and quality, as a dissertation for the degree of Doctor of Philosophy.

Martin Vala
Professor of Chemistry

I certify that I have read this study and that in my opinion it conforms to acceptable standards of scholarly presentation and is fully adequate, in scope and quality, as a dissertation for the degree of Doctor of Philosophy.

Jeffrey Krause
Assistant Professor of Chemistry

I certify that I have read this study and that in my opinion it conforms to acceptable standards of scholarly presentation and is fully adequate, in scope and quality, as a dissertation for the degree of Doctor of Philosophy.

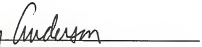

Timothy Anderson
Professor of Chemical Engineering

This dissertation was submitted to the Graduate Faculty of the Department of Chemistry in the College of Liberal Arts and Sciences and to the Graduate School and was accepted as partial fulfillment of the requirements for the degree of Doctor of Philosophy.

August, 1998

Dean, Graduate School